UNIVERSITAT POLITÈCNICA DE CATALUNYA BARCELONATECH

Fractal approach to wheel-rail roughness contact theory

Laura Mariana Babici

Fractal approach to wheel-rail roughness contact theory

Laura Maria BABICI

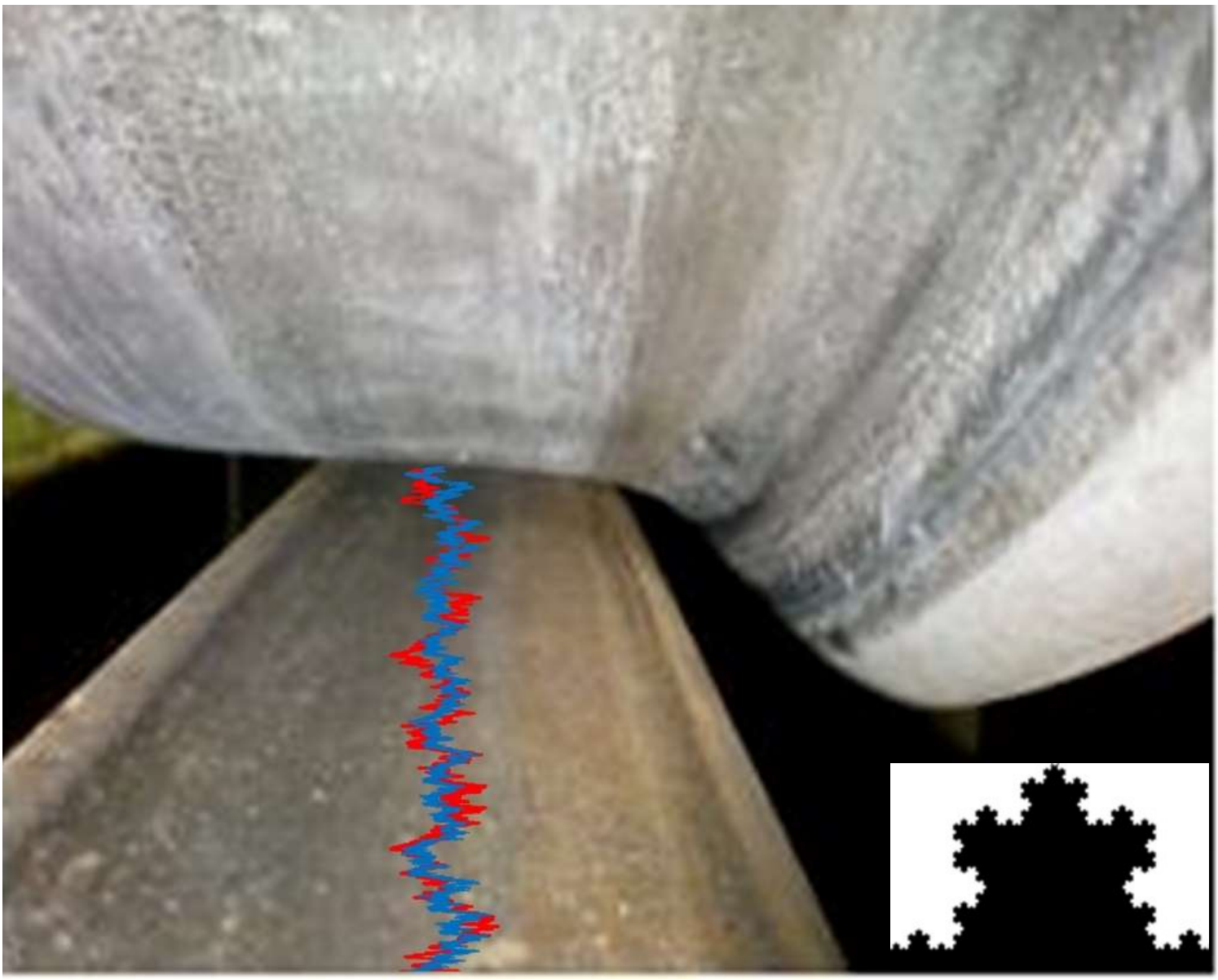

Doctoral Thesis
Supervisors: Jordi ROMEU and Andrei TUDOR
December 2023

Departament d'Enginyeria Mecànica
UNIVERSITAT POLITÈCNICA DE CATALUNYA

DEPARTMENT OF MACHINE ELEMENTS AND TRIBOLOGY
NATIONAL UNIVERSITY OF SCIENCE AND TECHNOLOGY
POLITEHNICA BUCHAREST, ROMANIA

Departament d'Enginyeria Mecànica
UNIVERSITAT POLITÈCNICA DE CATALUNYA

DEPARTMENT OF MACHINE ELEMENTS AND TRIBOLOGY
NATIONAL UNIVERSITY OF SCIENCE AND TECHNOLOGY
POLITEHNICA BUCHAREST, ROMANIA

Fractal approach to wheel-rail roughness contact theory

by

Laura Maria BABICI

Thesis submitted to obtain the title of
Doctor in Mechanical Engineering
by the
Universitat Politècnica de Catalunya (UPC)
and
National University of Science and Technology
Politehnica Bucharest, Romania (UPB)

December 2023

Abstract

In this study, the Weierstrass fractal function was used to model the surface roughness of railway tracks and, subsequently, the static coefficient of friction (COF) for Hertzian rail-wheel contact and cylinder-plane interactions. This methodology is based on the assumption that the fractal nature of surface roughness can be effectively captured using fractal parameters, which significantly influence the contact mechanics and frictional behaviour observed in railway systems.

Initially, the study focused on a detailed modelling of the railway track surface roughness. To validate the efficacy of this model, a rigorous and meticulous comparison between the theoretical results obtained and the experimental data was conducted. These data were collected through extensive roughness measurements carried out at the Faurei Railway Testing Centre in Romania. For robust validation, 41 roughness parameters derived from the fractal model were compared with those measured experimentally. This comprehensive approach allowed not only for the validation of the fractal model but also for its refinement by identifying which parameters are most critical in representing the real roughness of the tracks, as well as the minimum measuring length for determining acoustic roughness.

The experimental determination of the static COF was conducted through laboratory tests involving two cylinder-plane specimens, made from the same material as the railway wheel and track. This configuration was chosen to closely replicate the contact conditions found in actual wheel-rail interactions, thus ensuring that the experimental data collected were representative and reliable.

To precisely determine the static COF, the stick-slip (SS) process was meticulously characterized by monitoring acoustic emissions (AE), allowing for convenient identification of each phase. The acoustic emissions provided a non-invasive means not only to detect transitions between stick and slip phases but also to understand the underlying mechanisms driving these transitions.

This dual approach of theoretical modelling and experimental validation forms the core of this methodology and offers a comprehensive understanding of the frictional phenomena occurring within railway systems, which essential for designing and maintaining safer and more efficient railway operations. The insights gained from this study are expected to significantly contribute to the development of new standards and practices in railway engineering, particularly in areas of wear reduction, noise control, and overall system reliability.

The results of this research pave the way for a more nuanced understanding of the fractal nature of contact surfaces and their implications on tribological performance.

Acknowledgements

The completion of this research work would not have been possible without the help and support of several individuals to whom I wish to express my deepest gratitude.

I would like to extend my deepest gratitude to my supervisors, Prof. Jordi Romeu and Prof. Andrei Tudor, for their guidance, continuous support throughout my Ph.D. studies, and for their patience, motivation, and vast knowledge. Their counselling has been instrumental throughout the period of research and writing of this thesis. Their tireless efforts in shaping my scientific thought and in enhancing the clarity and depth of my analysis deserve special recognition.

My sincere gratitude also goes to Dr. Cristian Ulianov, who provided me the opportunity to join their Railway Technology Team Lead as a visiting researcher at the Newcastle University, UK, offering me fresh perspectives in my research and helping me to broaden my horizons in this field of study.

I sincerely thank the leadership of the Romanian Railway Authority, the Faurei Railway Testing Center in Romania, and the leadership of Softronic Craiova, which significantly contributed by providing the essential experimental facilities for this study. I would like to thank the leadership and colleagues of the Romanian Railway Authority, specifically the Railway Notified Body Directorate - Laboratories Department, for all their support and understanding, making the completion of my thesis possible.

Furthermore, I would like to express my appreciation specially prof. Robert Arcos, to all members of the LEAM research group at UPC, and the Department of Machine Elements and Tribology at UPB. Without their valuable opinions and ideas, this research would not have been accomplished.

I would like to extend my heartfelt thanks to the review and guidance committee from the Department of Machine Elements and Tribology at UPB, comprised of prof. prof. Filip Ilie, Alexandru Radulescu, and prof. Adrian Predescu, for their unwavering support and valuable suggestions that have significantly contributed to the refinement and success of this research. I am also very grateful to all my colleagues at LEAM and the Department of Tribology for their friendship and assistance.

Finally, and most importantly, I wish to thank my husband, my son, and my entire family. Their support has gone beyond mere encouragement, being a constant source of comfort and emotional stability. Their role in this academic journey has been as vital as any academic contribution, providing me with the balance and well-being necessary to continue this pursuit of knowledge.

Dedication

Dedicated to my family

.

Contents

List of Tables

List of Figures

List of Figures

List of Symbols

Notation	*Description*
a	roughness amplitude
a_1, b_1, a_2, b_2	constant (Kogut, L. and Etsion, I. 2002)
a_{1p}, b_{1p}, a_{2p}, b_{2p}	constant (Kogut, L. and Etsion, I. 2002)
A_a	nominal or apparent area
A_{AEsl}	amplitude of the acoustic emission in the slip phase
A_{AEst}	amplitude of the acoustic emission in the stick phase
a_c	critical area
a_{cs}	dimensionless critical area
a_{cs1}	area that separates the second stage of elastoplastic from the-plastic stage
a_{cs2}	area that separates the first elastoplastic stage from the second elastoplastic stage
A_{eps1}	dimensionless contact area for first elastic regime
A_{eps2}	dimensionless contact area for second elastic regime
A_{es}	dimensionless contact area for elastic regime
a_{ls}	dimensionless maximum contact spot area
a_{ls}	maximum area of actual contact between wheel and rail
a_m	contact spot area of fractal surface
A_{ps}	dimensionless contact area for plastic regime
A_r	real contact area
A_{rs}	dimensionless real contact area
a_s	dimensionless contact spot area of fractal surface
B	cylinder width
C_t	fractal parameter
d	wheel diameter
D	fractal parameter
E	equivalent Hertzian elastic modulus
E_1, E_2	elastic modulus of Wheel and rail
F_{ep1s}	dimensionless contact load for first elastic regime

F_{ep2s}	dimensionless contact load for second elastic regime
F_{es}	dimensionless contact load for elastic regime
F_f	friction force
F_n	Normal force
$F_{ns}(a_{ls})$	dimensionless total contact load
F_{ps}	dimensionless contact load for plastic regime
G_f	characteristic scaling length/ scale coefficient
G_{fs}	dimensionless characteristic scaling length
H_d	hardness of the softer material,
k	coefficient related to the Poisson ratio of the wheel
k_{HE}	hardness factor
k_{yE}	yield ratio
l	length scale of fractal asperity (base diameter)
L_f	length of the friction path
L_{rr}	acoustic rail roughness level, denoted as L_{rr}
L_s	the sample length used for roughness measurement
n	is the integer number
$n(a)$	distribution function of the contact spot area
nh	high cut-off frequency of the profile
nl	low cut-off frequency of the profile
n_s	cumulative count of contact spots
P	Pearson correlation
P_p	contact load in the plastic regime
$P_{se}(a_s)$	dimensionless contact load in the elastic state
$P_{sep1}(a_s)$	dimensionless contact loads in the first elastoplastic regime
$P_{sep2}(a_s)$	dimensionless contact loads in the second elastoplastic regime
$P_{sp}(a_s)$	dimensionless contact load in the plastic regime
$P_{st}(a_s)$	dimensionless total contact load
R_a	curvature radius at the peak of the asperity
R_d	cylinder radius
$SF(k)$	represents the SF in discrete form
$\mathrm{SF}(\tau)$	structure-function in continuous form
$T_{tf}(a_{ls})$	maximum tangential load for fractal surfaces
v	driving speed [mm/s]

v_{slip}	sliding speed [mm/s]
W_{AEsl}	energy generated by the acoustic emission in the stick phase
W_{AEst}	energy generated by the acoustic emission in the stick phase
W_{COFsl}	energy consumed by friction in the slip phase
W_{COFst}	energy consumed by friction in the stick phase
$y(x)$	height of the roughness profile
$y_r(x)$	roughness signal
$yrW(x)$	represents the height of the generated fractal profile
δ	asperity deformation
δ_c	critical deformation
δ_{cs}	dimensionless critical asperity deformation
$\delta_s(a_s)$	dimensionless asperity deformation
Γ ()	represents the Gamma function.
γ	parameter which determines the frequency density in the roughness analysis
μ_k	kinetic friction coefficients
μ_s	static friction coefficient
$\mu_s(a_{ls})$	static friction coefficient for dimensionless fractal surfaces
μ_v	amplitude of the stick-slip phenomenon
Φe(D)	domain extension factor
Ψ	constant
ν	Poisson's ratio
ν_1	Poisson's ratio
ν_2	Poisson's ratio
σ_1	normal stress of the x coordinate axis
σ_2	normal stress of the y-coordinate axis
σ_y	yield stress
τ	displacement along the x-axis

List of Abbreviations

ACF	Autocorrelation Function
ADF	Amplitude Density Function
AE	Acoustic Emission
AE_{rms}	Acoustic Emission Root mean square Amplitude
COF	Friction Coefficient
B	Wheel width
Bh	Hertzian contact semi-axis
PSD	Power Spectral Density
Rd	Wheel radius
r_{rms}	Root Mean Square
SF	Structure-Function
SS	Stick-Slip
TCF	Făurei Railway Testing Centre
W_{AEst}	energy generated by the acoustic emission in the stick phase
WM	Weierstrass Mandelbrot

Chapter 1

Introduction

This chapter introduces the current thesis, beginning with a concise overview of harmonised legislation concerning wheel-rail roughness and its implications for rolling noise. Following that, an explanation is provided for adopting a simulated fractal approach, which targets the prediction of rail roughness and static friction coefficients. Within the Hertzian contact experiments, the acoustic emissions arising from the relative movement of the cylinder-plane specimens served as indicators for the onset of the slip phase, thereby establishing themselves as essential non-destructive tools in detecting and monitoring the slip phenomenon while concurrently accompanying the friction process. The experimental findings assertively corroborated that friction coefficient variations and bursts of acoustic emission are congruent across all contact pressure conditions and sliding velocities. After presenting the justification, the primary goals of the thesis are outlined. The chapter then culminates with a brief overview of the topics covered in each subsequent thesis section.

1.1. Overview

In the context of the ongoing modernisation of the European railway infrastructure, the compliance of rolling stock with current technical regulations is essential to ensure interoperability and reduce noise pollution. European standards, notably the "Technical Specifications for Interoperability" (TSI), as well as Directive 2008/57/EC and Regulation (EU) No. 1304/2014 of 26 November 2014, underscore the necessity for this compliance, aiming to guarantee the compatibility of vehicles within the EU territory and mitigate railway noise. A particular emphasis is placed on the identification and control of the main sources of noise. In the railway sector, it is unequivocally recognised that the intricate wheel-rail interaction primarily causes rolling noise. This interaction and the resulting noise are significantly influenced by the roughness of both components and their mutual engagement.

Thus, the roughness of the rail in the contact between the rail and the wheel significantly impacts the microstructural interaction, directly impacting the running noise (Thompson, 2003, R.J. Diehl, P. Holm, 2006, Wu, 2006). When a wheel moves over a rail with variable roughness, the interaction can generate noise fluctuations due to the variation in contact intensity and intermittent contact. This phenomenon can lead to increased noise, with considerable potential for noise pollution in the areas adjacent to the railway. Moreover, roughness directly influences the transmission of forces through the wheel-rail system, generating oscillations or vertical vibrations that affect both the passenger's comfort and the lifespan of components and infrastructure (R. Arcos, 2011, E. Verheijen, 2006). In addition to these immediate effects, roughness plays a key role in determining wear and maintenance needs. A rough rail can cause uneven wear, both in the wheel and in the rail, resulting in increased costs and the need for more frequent repairs. The adhesion between the wheel and the rail can also be compromised due to roughness, affecting the acceleration and braking efficiency of the train and, implicitly, the safety and overall performance (Zhang, 2002). In addition, roughness-induced vibrations can be transferred to neighbouring structures and soil, creating the potential for discomfort in nearby communities and affecting adjacent structures. For all these reasons, it is clear that monitoring and managing rail roughness is crucial for efficient and safe rail transport.

In the study of surface roughness and Hertzian contact mechanics, the fractal method presents an alternative approach. Fractals, structures or patterns that replicate across multiple scales highlight the auto-similar nature observed in many natural phenomena, including surface roughness.

Through these fractal structures, it becomes possible to represent the complexity of roughness from macroscopic features down to microscopic asperities more effectively than with traditional methods. Furthermore, due to their inherent auto-similar and auto-affine properties, fractals ensure a consistent roughness representation, maintaining the overall contour regardless of the scale at which it is analysed.

Utilising the Weierstrass-Mandelbrot function, the fractal method employs geometric progressions to model and simulate the subtle variations in roughness. This approach provides specific parameters for roughness characterisation that are independent of the resolution of the instrument, thereby facilitating a consistent roughness simulation across various scales.

In contrast to the traditional method, where the analysis of roughness is limited by the resolution of the instruments used, the fractal method proves to be versatile, accommodating changes observed at every scale. This attribute grants fractals a distinct advantage in terms of adaptability and comprehensive analysis of surfaces when compared to conventional methods.

The coefficient of friction in rail transport is important due to its influence on the interactions between the surfaces in contact, such as establishing the capacity to accelerate, brake or navigate safely. It also characterises the degree of adhesion or slip between two surfaces in relative motion and can determine the behaviour of a system in situations of braking, traction or slipping. The adequate value of the COF ensures the efficient transmission of forces from wheel to rail, allowing adequate traction and avoiding unwanted phenomena, such as wheel skating or accelerated wear. COF also influences rail and wheel wear rates, directly impacting the maintenance costs and life of the railway infrastructure. Unforeseen variability or changes in COF may result in loss of adhesion, causing possible skidding or slipping, with associated risks of accidents or material damage. In addition, the properly managing of the coefficient of friction helps prevent premature wear of components, reducing maintenance costs and extending the life of the infrastructure.

The "stick-slip" phenomenon in the railway system dynamics manifests rapid and distinct transitions between the adhesion and sliding phases of the wheel-rail Hertzian contact, stemming from variations in the friction coefficient, changes in humidity conditions, and the presence of contaminants at the contact interface. This behaviour, influenced by mechanical and environmental factors, can induce vibrations in the rolling stock and railway infrastructure, leading to acoustic emissions, often referred to as rolling noise, with the potential to disrupt the comfort of passengers and adjacent communities to railway lines. In this context, acoustic emissions (AE) are high-precision, non-destructive tools, allowing the observation and analysis of the stick-slip phenomenon, especially by clearly delineating the onset of the slip phase.

Furthermore, the alternation between adhesion and sliding, precisely the stick-slip phenomenon, can accelerate wear processes at the wheel and rail level, significantly reducing the lifespan of components, increasing operational and maintenance costs and, under certain circumstances, compromising travel safety, generating speed fluctuations and potential skidding. Such fluctuations can also alter the train's rolling performance, thereby affecting the overall efficiency of railway transport. Within the framework of maintaining the integrity and optimal functioning of the railway system, modern approaches, such as monitoring and adjusting the static friction coefficient through fractal modelling, are promoted as innovative solutions for managing and mitigating the impact of the stick-slip phenomenon, simultaneously ensuring efficient predictive maintenance.

1.2. Motivations

Monitoring and quality control of the railway track by evaluating the measured roughness is imperative in assessing the operation state. Although roughness is often perceived only as a physical characteristic, it plays a significant role as a source of rolling noise, having major implications on efficiency, safety, and environmental compliance. Given the multifaceted nature of roughness and its non-uniform manifestation across different scales, the fractal approach offers a more comprehensive analysis. Utilising fractal methods enables a deeper understanding of the intricate patterns and self-similarities inherent in roughness, which traditional methods might overlook. This enhanced insight gained through fractal analysis allows for more precise diagnostics, prediction, and mitigation strategies, ultimately leading to better management of the associated challenges posed by rolling noise and the ensuing impacts on railway operations.

The traditional modelling of Hertzian contact, based on the interaction between wheel and rail considering roughness, does not always accurately illustrate the complex interface interactions. With the introduction of fractal theory, a new perspective is opened on the true nature of the contact area between the wheel and rail. Opting for fractal theory in contact mechanics provides a much more detailed view, taking into account the inherent complexities and variations at different scales present in the contact surfaces of the real world. By approaching this perspective, one can arrive at a more accurate representation and prediction of Hertzian contact behaviour, thus creating more efficient solutions for reducing wear, decreasing noise, and optimising performance in railway systems. This justifies the need for detailed research in this field, as a deep understanding of these interactions can lead to significant innovations in railway engineering and overall infrastructure improvement.

The "stick-slip" phenomenon, characterised by a swift transition between adhesion and sliding, has profound implications in the railway domain, impacting performance and operational safety. A deep understanding of this phenomenon within contact mechanics allows us to identify and analyse the root causes of its manifestation and how it can influence the overall system behaviour. With this foundation of knowledge, effective solutions can be developed to minimise or eliminate the adverse impact of stick-slip, offering the opportunity to enhance the quality and efficiency of system operation. By delving deeper into the study of this phenomenon in the realm of contact mechanics, we can reveal the subtle details and complexities of the interaction, thus facilitating the development of more advanced monitoring, control, and optimisation strategies.

1.3. Thesis objectives

The primary objective of this research is to develop and implement specific algorithms based on fractal techniques for studying roughness within contact mechanics. Particular attention is given to investigating the roughness of railway wheels and tracks to provide essential information for the efficient maintenance of railway components and for mitigating vibrations and rolling noise.

The following task have been undertaken:

- Modelling roughness using the fractal formulation, based on the detailed analysis of 41 roughness parameters obtained from experimental measurements; to achieve this goal, the Weierstrass-Mandelbrot (W-M) function was applied to the mentioned parameters, and the results thus obtained were then compared with the original data to verify the validity of the fractal method, placing particular emphasis on acoustic roughness modelling, under the standards set by EN ISO 15610:2019.
- Modelling roughness through the fractal formulation, encompassing contact mechanics parameters and specifically addressing the static coefficient of friction (COF), provides a nuanced understanding of surface interactions at varying scales. This method makes capturing the multifaceted nature of wheel-rail contact interactions feasible, which often eludes traditional modelling techniques. Such an approach not only refines our grasp of the underlying mechanisms but also paves the way for enhanced predictive capabilities, aiding in designing and maintaining more efficient systems in railway engineering contexts.
- Analysing the stick-slip behaviour in a Hertzian contact involves investigating the correlations between Acoustic Emission (AE) minimal parameters and the COF

(coefficient of friction), particularly at low and very low driving speeds. The initiation of relative motion between two bodies in friction is foundational in understanding the principle of friction in tribology. Through this approach, the minimal AE parameters prove to be both adequate and sufficient to detect and monitor the stick-slip phenomenon, pinpointing the onset of the slip phase. This establishes AE as an effective, non-destructive tool for detecting and monitoring the stick-slip behaviour.

- Validation of the friction static coefficient using the fractals method and its comparison with the experimental static friction coefficient results.

1.4. Thesis Outline

The content of the present thesis is divided into five chapters. All chapters except Chapter 1 and Chapter 5, Introduction and Conclusion, and Further Work, respectively, include their state-of-the-art within the introduction. The chapters of the thesis are organised as follows:

Chapter 1 presents a general introduction to the research, the justifications, the objective and the thesis outline.

Chapter 2 introduces a methodology that employs fractal modelling techniques to capture rail roughness characteristics intricately. The complex nature of rail roughness is depicted in detail by using both the structure and Weierstrass Mandelbrot functions. Data from the Făurei Railway Testing Centre in Romania validate that the roughness height exhibits distinct mathematical fractal traits. A total of 41 classical statistical parameters derived from roughness measurements were juxtaposed against their simulated fractal counterparts. Parameters such as the Autocorrelation function, Amplitude Density Function, Bearing Area Curves, and rail acoustic roughness were generated using the Weierstrass function. Comparisons between these parameters and the actual measured data indicate significant congruence. Most parameters demonstrated a relative error within a 10% range, emphasising the effectiveness of the fractal approach in assessing rail roughness dynamics. Consequently, the simulated parameters could be vital tools for rail roughness evaluation, promoting enhanced track maintenance, grinding, and noise reduction.

Chapter 3 focuses on the analysis of the static coefficient of friction (COF) and Hertzian contact parameters from a fractal perspective. This approach enables the fractal model to encompass the real contact area, reflecting the surface asperities not as ideal geometric shapes but as complex and irregular structures, which more accurately represent reality. This significantly enhances understanding of phenomena within the contact zone and contributes to more accurate modelling of contact parameters.

The work highlights that the COF value is affected by the material characteristics of rough surfaces, the fractal parameters describing the topography, and the applied normal force. The fractal model, with its ability to simulate complex interactions at a micrometric scale, provides a valuable contribution to predicting and analysing contact behaviour. Thus, it paves the way for advanced design and optimisation of mechanical systems, with direct applications in areas where friction and wear determine performance and reliability, such as in the railway industry.

Based on the WM model, four deformation regimes have been assessed: elastic, the first and second elastoplastic, and fully plastic. The static friction coefficient, theoretically derived from fractals and contact mechanics, can be viewed as the "intrinsic property" of the softer of the two entities in contact, marked by its surface microgeometry in terms of fractal dimensions. This approach to contact mechanics within the fractal context paves the way for advancing more robust methods for managing and controlling adherence under diverse operating conditions.

Chapter 4 highlights that the fundamental AE parameters effectively detect the stick-slip phenomenon. Using a custom configuration of the tribometer tailored for these experiments, a thorough analysis of AE signals was conducted, bypassing the need for traditional AE equipment. The central aim of the tests was to delve into the interrelations between AE and COF parameters, with emphasis on extremely low driving speeds, considering the onset of relative movement between two frictional bodies is key to grasping the friction principle in tribology.

In this context, connections were established between foundational AE characteristics and stick-slip attributes, like static and kinetic friction coefficients, as well as their temporal evolution. Tribological tests were carried out on the cylinder-plane specimen under dry friction conditions at varied Hertzian contact pressures and driving speeds. The rig was set to record AE, normal, and frictional forces concurrently, noting that AE peaks followed immediate variations in the friction coefficient. Findings revealed the sensitivity of AE amplitude and energy to the stick-slip manifestation, with energy profiles for both AE and COF indicating consistent patterns based on driving speed. Ultimately, the fractal-derived static friction coefficient was compared to the experimentally obtained coefficient at a driving speed of zero.

Chapter 2

Fractal - based modelling of rail roughness

2.1. Introduction

Railway maintenance and track grinding are crucial aspects for railway operators to ensure a comfortable and safe journey for passengers. One significant factor in this process is the surface roughness of the rail system, which holds a vital aspect in the overall research of track quality. Characterizing this roughness is essential in understanding and improving the railway infrastructure. By understanding and quantifying track roughness, railway operators can take proactive measures to reduce noise below (*Kourroussis G., 2014*), improve safety, and extend the lifespan of railway components. Moreover, these characterizations can help develop better maintenance strategies and optimize the overall performance of railway systems. Researchers have extensively studied the impact of track roughness on generating rolling noise, which can be a significant environmental noise source (*Thompson D. J., 2001, Thompson D. J., 1996*). Track roughness effects result in vertical vibrations within the wheel-rail system, serving as the primary sources of rail noise, wear, friction, and elastoplastic deformations in the material (*Kiyak M., 2007, Xiao L. et al., 2003, Benardos P. G. and Vosniakos G. C., 2003*). As a result, the characterization of track roughness has become a technical requirement in both the railway (EN 15610:2018 and ISO 3095:2013) and tribological (EN ISO 21920-2:2023) fields.

Quantitative estimation of rail roughness involves using a series of statistical parameters. These parameters include amplitude, spatial, and hybrid parameters, each corresponding to specific roughness properties (*Gadelmawla E. S. et al., 2002, Thomas T. R., 1982, G. W. Stachowiak, 2004*). By analysing these parameters, valuable information about the quality of the track roughness profile can be obtained. One quantitative method to assess the roughness is determining the rail acoustic roughness associated with rolling noise. This approach allows for a practical assessment of the impact of track roughness on noise generation.

In conducting this roughness analyses, it is advantageous to consider a wide range of roughness parameters. The more parameters that are analysed and correlated with each other, the more comprehensive the understanding of the track surface quality becomes. This comprehensive analysis can aid in identifying specific issues, potential wear patterns, and opportunities for improvements in track maintenance. It is worth noting that the roughness of the rail is commonly assumed to follow a Gaussian and isotropic distribution (*Kamash K. M. A. and Robson J. D., 1978, Cooper A. J. et al., 2015, Crandall S. H. and Zhu W. Q., 1983,*

Villamarin R. A., 2011). This assumption simplifies the statistical modelling and analysis of roughness data and provides a helpful basis for characterizing the rail surface.

Overall, the quantitative assessment of track surface roughness through statistical parameters and rail acoustic roughness analysis plays a essential role in maintaining track quality and ensuring a comfortable and safe railway journey. The gathered information aids in making informed decisions regarding track maintenance, optimizing maintenance schedules, and enhancing the overall performance of railway systems.

However, it is traditionally accepted that the variation of a rough surface from its average plane is typically considered random (*Nayak P. R., 1966, Greenwood J. A. and Williamson J. B. P., 1966*), multi-scale (*He L. and Zhu J., 1997, Zhou G., 1993*) and non-stationary (*Nayak P. R., 1973, Thomas T. R., Thomas A. P., 1988*) processes for which statistical parameters like height, slope and curvature variances utilized for characterizing roughness are highly dependent on the sampling length and resolution of the roughness measuring device and therefore not unique for the same surface (*Zhu H. et al., 2003, Jordan D. L., Hollins R. C. and Jakeman E., 2003, Majumdar A., Tien C. L., 1990, Majumdar A., Bhushan B., 1991, Dong W. P., Sullivan P.J. and Stout K.J., 1994*). When the surface is repeatedly magnified, statistically similar surface images continue to appear, and details down to the nanoscale can be observed (*Majumdar A., Tien C. L., 1990*).

It is, therefore, necessary to characterize the roughness of the track by an instrument-independent method at any scale of magnification. A roughness characterization method that is independent of the instrument ensures that the results obtained are not influenced by factors such as the measuring resolution of the instrument, sampling length, or other instrument-related considerations. This aspect is critical in railway track roughness analysis, as different measurement instruments may yield slightly different results, making comparing and interpreting data from various sources challenging.

In recent years, fractal geometry has drawn considerable interest in characterizing surface topography because the fractal model does not depend on the scale (*Gagnepain J. J., and Roques-Carmes C., 1986, Majumdar A. and Bhushan B., 1990*). One of the fundamental characteristics of fractals is their scale invariance, meaning they have similar patterns and structures on different scales. This property is crucial in the context of surface roughness analysis. Due to the scale independence of fractals, roughness properties are not limited to a specific range of scales. Using the Weierstrass-Mandelbrot (WM) function presented in (*Majumdar A. and Bhushan B., 1990*), which satisfies the self-affinity property (*Majumdar A.,*

Tien C. L., 1990, *Peitgen H. O. and Saupe D., 1988, Mandelbrot B. B., 2021*) the fractal analysis also enables roughness modelling with scale-independent parameters, which allows forecasting surface attributes across various scanning lengths based on measurements at a single scanning distance.

Determining essential parameters for characterizing fractal surfaces with roughness fractal dimension D and scale coefficient G_f involves different approaches such as the compass method (*Mandelbrot B. B., 1967, Mandelbrot B. B., 1985, Carr J. R., Benzer W. B., 1991*), variogram or structure function method (*Zhang X., Xu Y. and Jackson R. L., 2017, Ganti S., Bhushan B., 1995, Berry M. V. and Lewis Z. V., 1980*), length-roughness method (*Malinverno A., 1990*), and Power Spectral Density (PSD) method (*Wen R. J., Sinding-Larsen R., 1997, Mandelbrot B. B. and Vanness J. W., 1968, Li H. et al., 2023*). These techniques aid in accurately describing and understanding the complex nature of rough surfaces across various scales, providing valuable insights for railway track roughness analysis and other applications.

The primary aim of this chapter is to examine the fractal nature of rail surface roughness, which is based on roughness measurements taken at the Făurei Railway Testing Centre (TCF) in Romania, by deriving the fractal parameters and defining two essential parameters, D and G_f, to characterize the rail roughness accurately. To achieve this goal, an evaluation and a comparison of the classical statistical parameters obtained from roughness measurements with simulated fractal parameters was performed using the WM function for the same measurements.

In addition, acoustic roughness modelling was performed using the WM function and the results were compared with the acoustic roughness data obtained from the experimental measurements. By comparing the classical statistical parameters with the fractal parameters obtained from the WM function and analysing the acoustic roughness data, the paper seeks to offer an in-depth insight into the fractal characteristics of the roughness of the rail surface.

2.2. Theory

For a signal $y_r(x)$, whose increment $y_r(x_i+ \tau) - y_r(x_i)$ is assumed to have a Gaussian distribution with zero mean, a function called a structure-function (SF) in continuous forms (*P. R. Nayak, 1973*) is defined:

$$SF(\tau) = \langle (yr(x) - yr(x+\tau))^2 \rangle = C_t(|\tau|)^{(4-2D)}, \quad (2.1)$$

where τ is a displacement along the x-axis $C_t = \psi G_f^{2(D-1)}$, D and G_f are the fractal parameters, and Ψ *(A G.Y. Zhou et al., 1993)* is given by the equation:

$$\psi = \frac{\Gamma(2D-3)\, sin(2D-3)\pi/2}{2-D}, \tag{2.2}$$

in which Γ ( ) represents the Gamma function.

The graph of S(τ) concerning τ in Eq. (1) appears as a straight line when plotted using double logarithmic coordinates of the form:

$$log(S(\tau)) = (4-2D)\, log\, \tau + log\, C_t, \tag{2.3}$$

If the original signal *yr* (*x*) is divided into *Nr* equal intervals, $\Delta x = x_q/Nr$, where x_q is the length of the measured section, the SF in discrete form, *SF(k),* of a signal $yr(x_i)$ is:

$$SF(k) = \frac{1}{Nr-k}\sum_{i=1}^{Nr-k}(yr_{i+k} - yr_i)^2, \tag{2.4}$$

where, *SF(k)* represents the SF in discrete form and *k* varies in the range 1 to *Nr*.

To assess the surface roughness of the rail, *SF(k)* was calculated using measurements along the rail, and then the shape and behaviour of the graph were analysed. The graph analysis delineates the linear and nonlinear regions of the Structure Function. If the *SF(*k*)* forms a straight line on a double logarithmic coordinate with a unique slope that is a non-integer number between 0 and 2, indicating a power law with a relationship between the roughness and the length scale, the rough surface of the rail (*yr* (*x*)) has a fractal character. *D*, C_t and G_f can be obtained by directly comparing results from Eq. (3) and the logarithmic version of Eq. (4). D and Gf are independent of the spatial correlation distance τ, signifying that they are inherent surface roughness parameters not tied to any specific scale.

Once *D* and G_f are known, the roughness can be estimated using fractal parameters by the WM continuous function *yrW(x*) of the following form (*Majumdar A. and Bhushan B., 1990, Mandelbrot B. B., 2021, Zhang X., Xu Y. and Jackson R. L., 2017, Majumdar A., Tien C. L., 1991, Singh A. N., 1953, Green I., 2020*):

$$yrW(x) = G_f^{D-1}\sum_{n=nl}^{nh}\frac{cos(2\pi\gamma^n x)}{\gamma^{(2-D)n}}, \qquad 1< \gamma<2 \tag{2.5}$$

where, *yrW(x)* represents the height of the generated fractal profile, and G_f is the characteristic length scaling constant *(Zhou A. G. Y. et al., 1993)*; it establishes the position of the spectrum on the power axis and remains unchanged concerning all roughness frequencies; *D* represents the fractal dimension of the profile, and it can be a non-integer value between 1 and 2 for 2D and between 2 and 3 for 3D; γ is a parameter which determines the frequency density in the roughness analysis; *n* is the integer number of items gathered by the series during the roughness measurement process, and it indicates the total number of data points considered in the analysis; *nh* corresponds to the high cut-off frequency of the profile, depending on the resolution of the instrument used to capture the roughness data, and nl corresponds to the low cut-off frequency

of the profile. By setting appropriate values for γ, n, nh, and nl, we can control the frequency range of the roughness data used in the analysis. This allows values to focus on specific roughness scales and obtain meaningful results that capture the relevant features of the rail surface profile. As surfaces are non-stationary random processes (*Majumdar A., Tien C. L., 1990, Sayles R. S., Thomas T. R., 1977*), the lowest cut-off frequency is contingent on the sample length used for roughness measurement, denoted as L_s, and it is defined as $\gamma^{nl} = l/L_s$.

2.3. Methodology

This study aimed to establish a correlation and comparative analysis between rail roughness parameters obtained through experimental measurements conducted at Făurei Railway Testing Centre, Romania, and those derived from simulated roughness profiles generated using the fractal method involving the WM function.

This comparison helps validate the effectiveness of the fractal method in capturing the essential characteristics of roughness and provides valuable information related to noise generation and track maintenance. Also, the prediction of the rail roughness by using the fractal model with the Weierstrass function was performed.

The method of measuring direct rail acoustic roughness involves placing the transducer on the surface of the rail, which allows an isolated measurement of the roughness of the rail without being influenced by wheel surface roughness or other potential interactions of wheel-rail contact. The rail acoustic roughness was compared with the rail acoustic roughness calculated using the fractal method involving the WM function.

2.3.1. Experimental measurements

The experimental tests were carried out within the Făurei Railway Testing Centre, belonging to the Romanian Railway Authority, whose total length of the lines is 20.2 km, of which the Small Ring is 2.2 km long and the Big Ring, with an electrified network and 1435 mm gauge, is 13.7 km long, two curves with radii of 1800 m and lengths of 1000 m and 950 m respectively. At present, it is feasible to conduct dynamic assessments of rail vehicles, allowing for testing at a maximum speed of 200 km/h.

To determine the roughness of the track on the Big Ring, a segment of straight-line type UIC 60 was chosen, on ballast bed and concrete sleepers, without visible joints or defects, located at kilometre marker 6 + 900 km (Figs. 2.1-2.2). The test area was chosen in such a way that the rail did not show any visible defects that could cause high vibrations, which subsequently lead to an amplification of the rolling noise.

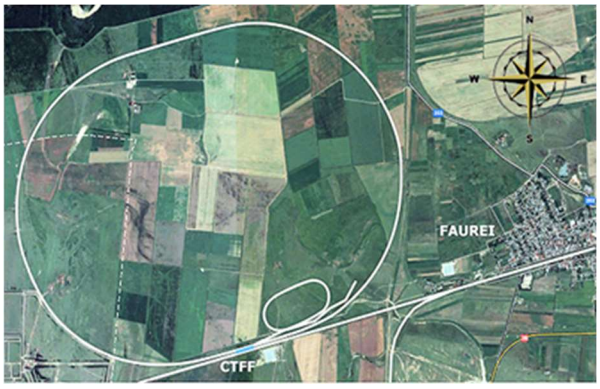

Fig. 2.1. RailwayTesting Centre graphic presentation.

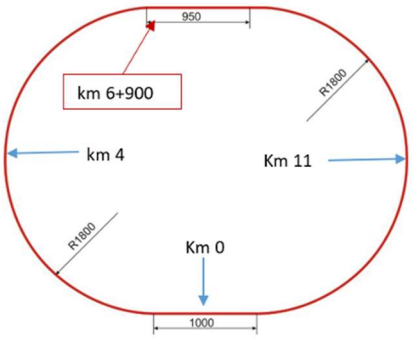

Fig. 2.2. Testing area.

The tests were conducted following the guidelines outlined in EN 15610:2019 (Chapter 5), employing the direct approach for measuring rail surface roughness. A total test surface length of 30 m was considered, comprising four test sections of 7.5 m each. Regarding the lateral position of the valid reference surface of the rail, as it is larger than 30 mm, the roughness was measured on the centre line of the reference surface as well as on two additional parallel lines located to the left and right of the centre line at a distance of 10 mm from it, for both rails. These four test sections with the roughness measured on the centreline of the surface were analysed. The rail roughness measurements were performed using a high-precision measuring system m|rail trolley equipment, that uses an interdependent acceleration sensor that is manually moved along the rail (trolley) and continuously records the rail roughness with a vertical resolution of 1 mm (Fig. 2.3).

Fig. 2.3. Equipment m|rail trolley

2.3.2. Data processing of roughness

In order to analyse the rail roughness condition, the experimental sequence of the roughness profile of centre line vector *yr(xi)* for the centre-hand thread of the outer ring of length 7.5 with a profile discretization of 1 mm was selected and analysed. The peak removal techniques and curvature processing were performed for roughness data, according to EN 15610:2019, chapter 5.

In order to eliminate the effects of dust or dirt granules on the rail head, an algorithm has been included that removes "spikes and pits", i. e. very short spikes and pits (much reduced than the wheel-rail contact area). A second algorithm, known as "curvature processing," is developed to manage similar features that the small radius tip of the probe would detect but would not affect a much larger radius wheel.

2.3.3. Calculations

Different surface roughness parameters are compared to check if the fractal approach is suitable to model roughness. Thus, 41 parameters defined as amplitude, spatial and hybrid parameters calculated in 2D (*Majumdar A., Bhushan B., 1991*) and the rail acoustic roughness were analysed. In order to compare the experimentally determined roughness with the simulated roughness obtained by the WM method, the roughness parameters for the four measured test sections of 7.5 m each were compared.

The parameter γ in Eq. 5 is a parameter that can be adjusted in fractal analysis when using the WM function. Frequency density controls are essential in defining the range of frequencies taken into account for characterizing the roughness profile. As γ is dimensionless, it can serve as a consistent ratio within the geometric progression of frequencies (*Majumdar A., Tien C. L., 1990*). For this study, a γ value of 1.5 was selected for all generated fractal profiles, as it is deemed appropriate for achieving both high spectral density and phase randomization across the interval $[0,2\pi]$ (*Majumdar A. and Bhushan B., 1990, Green I., 2020*).

Each section of 7.5 m was considered and systematically divided into segments ranging from 1 metre (the minimum length prescribed according to EN 15610:2019) to 7.5 metres. This segmentation was carried out using increments of 500 millimetres. In this framework, the roughness parameters obtained from the measured roughness for the 7.5 m length were compared with the roughness parameters obtained by simulation using the WM function. Determining these parameters involved a comprehensive analysis of zero-mean roughness profiles for both, measured and simulated roughness data.

2.4. *Results and discussions*

The SF analysis method was employed to examine the fractal nature of the rail roughness from CTF Făurei Romania and to determine the fractal parameters for each segment of roughness-subjected analysis following Eqs. 1-4. This analysis confirmed the fractal nature of the rail's roughness as each segment adhered to the exponential law criterion, indicated by its linear behaviour on a double logarithmic scale in the structure-function plot (Fig. 2.4.a). Following the fractal method, which used the WM function and involved the fractal dimension, D, the characteristic length scaling constant G_f, and other relevant parameters, synthetic roughness profiles were created to mimic the fractal nature of the real roughness of the rail. The fractal roughness simulated by WM modelling and the measured roughness for the first section of the length of 7.5 m is shown in Fig. 2.4.b, and it can be seen that simulated roughness follows the same trend as measured roughness.

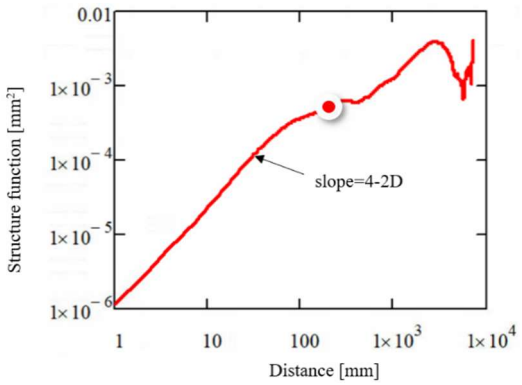

Fig. 2.4.a. Structure-function log-log of the rail roughness measurement data (7.5 m).

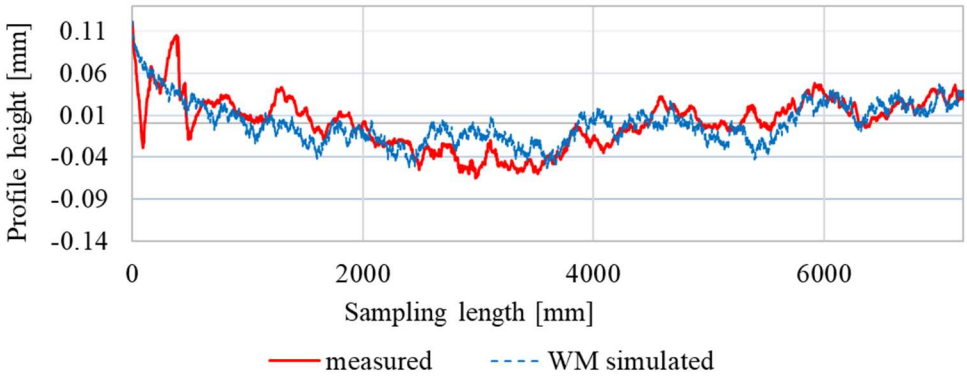

Fig. 2.4.b. Comparison between experimental (solid line)
and simulated (dotted line) rail roughness (7.5m).

Surface roughness is commonly characterized using scalar parameters, such as the root mean square (rms) for height, slope and curvature. These parameters characterize the amplitude

of spatial variations in height, slope and curvature for the measured roughness. However, a significant issue with these roughness parameters is that they depend explicitly on the measurement scale. For example, the height of the rms value increases with the measurement lateral dimension (the largest scale) and the slope rms value changes with the resolution of the measurement (the smallest scale) (*Bhushan B., Majumdar A., 1992, Russ J. C., Fractal Surfaces, 1994, Sanner A. et al., 2022)*.

To demonstrate the scale independence of the roughness parameters obtained by the fractal method, simulated roughness parameters obtained using the WM function for different measuring scales were then compared with the roughness parameters calculated for the first measured test section of 7.5 meters, which is equal to each of these parameters providing the specific information about the roughness profile of the track.

Comparing the roughness parameters measured with the simulated values at different length scales, we can assess whether the fractal method provides consistent results, regardless of the measurement scale used. This analysis allows us to validate the scale independence of the fractal approach and its ability to accurately capture the essential roughness characteristics. For starters, amplitude parameters, the most important surface characterization parameters with roughness, which provide information on surface quality, roughness variations and other essential rail features, were analysed. For example, Table 1 compared the roughness parameters calculated for the measured roughness of 7.5 m and the simulated roughnesses for lengths of 7.5, 5 and 2.5 m, respectively. For each set of parameters calculated, the relative error was determined.

However, as expected, it can be seen that the smaller the experimental data collected, the lower the accuracy, but the results are a pretty good event for a short experiential extent. The results for the length of 7.5 are consistently below the relative error of 10% and always have the same order of magnitude of value result referring to each parameter analysed.

Table 2.1. Amplitude parameters.

No param.	Parameters	Experimental data for 7.5m [mm]	Simulated data for 7.5m [mm]	Relative error [%]	Simulated data for 5m [mm]	Relative error [%]	Simulated data for 2.5m [mm]	Relative error [%]
	Amplitude parameters							
1	Arithmetic average height (Ra) [mm]	0.026	0.024	7.692	0.023	10.000	0.023	10.000
2	Root means square roughness (Rq) [mm]	0.032	0.029	9.375	0.028	12.500	0.028	12.500
3	Ten-point height (Rz)(ISO) [mm]	0.046	0.045	2.174	0.047	-2.174	0.043	6.522
4	Ten-point height (Rz) (DIN) [mm]	0.04	0.04	0.00	0.041	-2.500	0.039	2.500
5	Maximum height of peaks (Rp) [mm]	0.121	0.122	-0.826	0.131	-8.264	0.110	9.091
6	Maximum depth of valleys (Rv) [mm]	-0.069	-0.063	8.696	-0.055	20.290	-0.067	2.899
7	Mean height of peaks (Rpm) [mm]	0.044	0.044	0.000	0.042	4.545	0.048	-9.091
8	Mean depth of valley (Rvm) [mm]	0.036	0.039	-8.333	0.038	-5.556	0.033	9.722
9	Maximum height of the profile (Rt) [mm]	0.190	0.178	6.316	0.186	2.105	0.150	21.053
10	Mean of maximum peak to valley height (Rtm) [mm]	0.080	0.082	-2.500	0.08	0.000	0.067	16.250
11	Largest peak to valley height (Ry) [mm]	0.150	0.148	1.333	0.141	6.000	0.150	0.000
12	Third point height (R3y) [mm]	0.057	0.060	-5.263	0.067	-17.544	0.081	-42.105
13	Mean of the third point height (R3z) [mm]	0.037	0.037	0.000	0.034	8.108	0.037	0.000
14	Profile solidity factor k	0.190	0.209	-10.000	0.203	-6.842	0.172	9.474
15	Skewness (Sk)	-0.038	0.747	-3<Sk<3	1.220	-3<Sk<3	0.896	-3<Sk<3
16	Kurtosis (Ku)	0.171	1.164	-3<Ku<3	2.450	-3<Ku<3	0.540	-3<Ku<3

Some discrepancies can be observed from Table 2.1. between the skewness and kurtosis of the measured and the calculated profile. Further data distribution analysis (Figs. 2.5.a and 2.5.b) shows that the measured roughness obeys a symmetric Gaussian distribution. In contrast, the simulated roughness shows a slight positive skewness (range 0.5-1) with high peaks or domed valleys. Both sets of data show few outliers, sharpness peaks and deep valleys. In a

perfectly Gaussian distribution, the skewness value is zero, and the kurtosis value is three. Nevertheless, within an acceptable range, skewness values typically vary between -3 and +3, while kurtosis values are considered good within a range of ± 3 (Jacobs T. D. B., Junge T. and Pastewka L., 2017, A. Gujrati et al., 2018) or even within a broader range of ± 10 (Sovey S., Osman K. and Mohd-Matore M. E., 2022), and therefore, the results of skewness and kurtosis tend to show similarities.

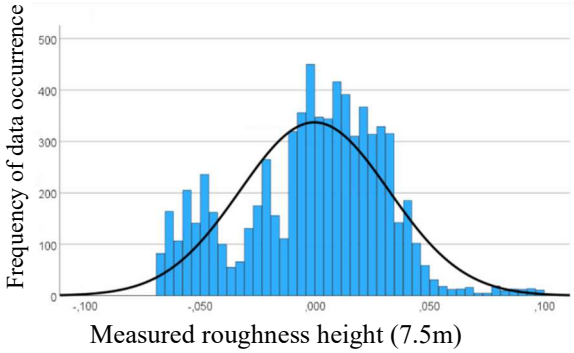

Fig. 2.5.a. Histogram for measured roughness (7.5 m).

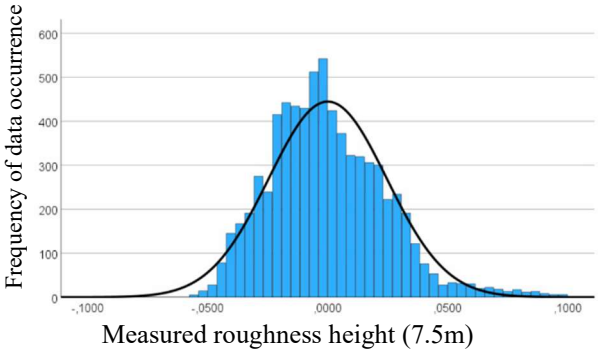

Fig. 2.5.b. Histogram for simulated roughness (7.5 m).

The differences between simulated fractal values and measured roughness values in a Gaussian distribution are influenced by various factors, including inherent variability, measurement errors, surface complexity, scale effects, and the assumptions and constraints of the fractal model used. Hence, it is essential to interpret and validate the results carefully, taking into account the specific characteristics and limitations of both the fractal simulation and the roughness measurement technique. However, since some discrepancies arise between the height distribution from the experimental and calculated data, some additional parameters are calculated to determine how the calculated roughness resembles the experimental data.

The Amplitude Density Function (ADF) is a statistical tool used to describe the distribution of amplitude values within a surface profile. In the context of roughness analysis, ADF provides valuable insights into the distribution of height variations or amplitudes along the length of a surface. It helps characterize the occurrence and intensity of different amplitude levels, revealing information about the texture and irregularities of the surface. ADF depicts the distribution histogram of the profile, which can be seen in Fig. 6, and is defined by the next equation:

$$ADF = \sqrt{2\pi R_q^2 \exp\left[\frac{-yr^2}{2R_q^2}\right]}. \tag{2.6}$$

The distribution of amplitude values captured by ADF can be correlated with functional properties such as friction, wear, contact behaviour and material performance. In addition, ADF allows the comparison of surface profiles from different sources or treatments, helping to control quality, optimize processes and evaluate surface changes with roughness (*Q. Zeng et al., 2018*). Fig. 2.6 clearly illustrates a striking similarity between the measured and simulated ADF for 7.5 m length. The resemblance is particularly evident in their overall shape and the peak amplitudes. Notably, even though a minimal disparity exists in the R_q values, this discrepancy has a negligible impact on the overarching trend of the ADF curve.

Another important amplitude parameter is the autocorrelation function (ACF), which measures the relationship between the current value of a variable and its past values and can help measure how much influence the real roughness has on a future one. The ACF can help detect anisotropic behaviour in certain rough surfaces, meaning the surface characteristics vary depending on the measurement direction. Anisotropy may arise due to machining processes or material properties, and the ACF aids in quantifying these directional dependencies. In the rail roughness analysis, ACF is considered helpful for signal processing and helps in identifying dominant wavelengths and characteristic surface features. ACF is shown in Fig. 8, and the mathematical representation of this function is as follows:

$$ACF = \frac{\frac{1}{Nr+1}\sum yr * yr_{i+1}}{R_q^2}. \tag{2.7}$$

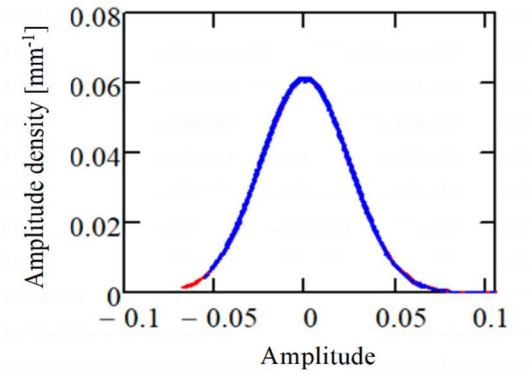

Fig. 2.6. Comparison between experimental (solid line)
and simulated (dotted line) amplitude density function (7.5m).

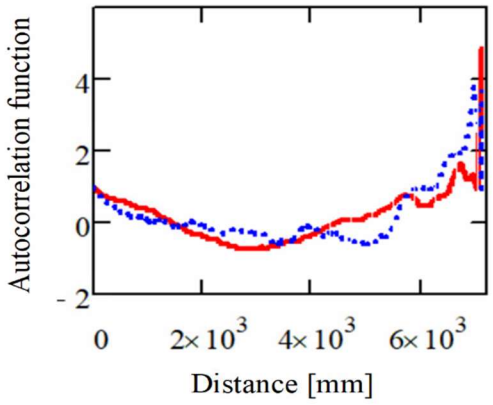

Fig. 2.7. Comparison between experimental (solid line)
and simulated (dotted line) autocorrelation function (7.5m).

Fig. 2.7 shows that autocorrelation for measured and simulated roughness for 7.5 m maintain a consistent pattern between them and remains positive and constant between 0 and 2, which predicts there will be no change in roughness variance very soon in both situations. For example, the rail grinding would be required only if the autocorrelation is a constant greater than 2. Similarly, graphs resembling those of the Autocorrelation Function (ACF) and the Amplitude Density Function (ADF) outlined above were generated for lengths of 5 and 2.5 meters, respectively, mirroring the pattern observed with a length of 7.5 meters. This aspect suggests a consistent trend across varying distances, highlighting the relationship between the respective functions and the analysed roughness measured and simulated profiles.

PSD is another essential parameter for identifying dominant spatial wavelengths present in a surface profile, understanding roughness behaviour at different length scales, and also plays a vital role in assessing noise sources related to the roughness of surfaces. In rail roughness analysis, PSD measures how different wavelength components contribute to the overall roughness. Short wavelengths may be associated with rolling noise, variations in the wear of rail surfaces or traces of material processing. In contrast, in precision machining or tribology applications, longer wavelengths are associated with airborne noise or vibration.

Fig. 2.8a compares the measured PSD and the PSD generated with the Weierstrass Mandelbrot function and provides information on how well the Weierstrass Mandelbrot model fits the actual roughness data for a length of 7.5 m, and in this context, the simulated PSD is comparable in trend to the measured PSD Furthermore, with the reduction of the roughness length up to 2.5 m, the results missed a wide range of wavelengths, but the coherence between the two PSD functions remains consistent across the 7.5 meters length, alignment that persists also as the distance decreases as can be seen in Fig. 2.8b.

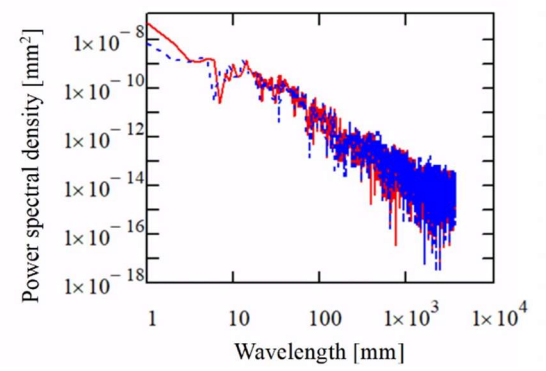

Fig. 2.8.a. Comparison between experimental (solid line) and simulated (dotted line) PSD function for roughness length 7.5 m.

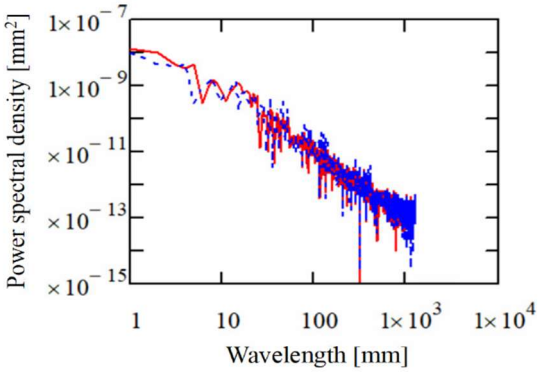

Fig. 2.8.b. Comparison between experimental (solid line) and simulated (dotted line) PSD function for roughness length 2.5 m.

An essential parameter in the railway system under examination is acoustic roughness, which records the height fluctuations of the running surface, correlating with the generation of rolling noise, and these variations are expressed as a function of the distance "x" along the running surface. Aligned with the guidelines of EN 15610:2019, in order to compare both measured and simulated roughness, the direct measurement approach was employed to characterize the roughness of the rail surface, precisely its correlation with the running noise referred to as "acoustic roughness." This characterization is represented in the form of a one-third-octave band spectrum.

The equation below provides the acoustic rail roughness level, denoted as L_{rr} and expressed in dB:

$$L_{rr} = 10\,log\left(\frac{r_{rms}^2}{r_0^2}\right), \tag{2.8}$$

where, r_{rms} represent the root mean square roughness in millimetres (mm), and r_0 is the reference roughness (r_0 = 1 mm). This definition pertains to values measured in a spectrum format using one-third octave band wavelengths.

Fig. 2.9 compares the relationship between rolling noise and rail roughness wavelength between measured and simulated rail acoustic roughness for a length of 7.5 meters. Notably, the simulated acoustic roughness aligns closely with the measured data at this length. The computed relative error calculated for these two scenarios of acoustic roughness stands at 7.31%. Likewise, as the measured length decreases to 2.5 m, the alignment of the roughness plots remains significant, and the calculated relative error for these cases is 5.76% for a 5 meters length and 3.64% for a 2.5 meters length. Another way to check the results is by calculating the overall deviation of the acoustic roughness spectrum from the TSI (technical

specifications for interoperability). For the length of 7.5 m, the deviation is 2.97 dB for measured acoustic roughness and 3.04 dB for simulated acoustic roughness. Therefore, the reduction of measurement length does not affect the accuracy of the acoustic roughness from the calculated roughness and also the wavelength range required by the standard EN 15610: 2019 (2.8-250 mm).

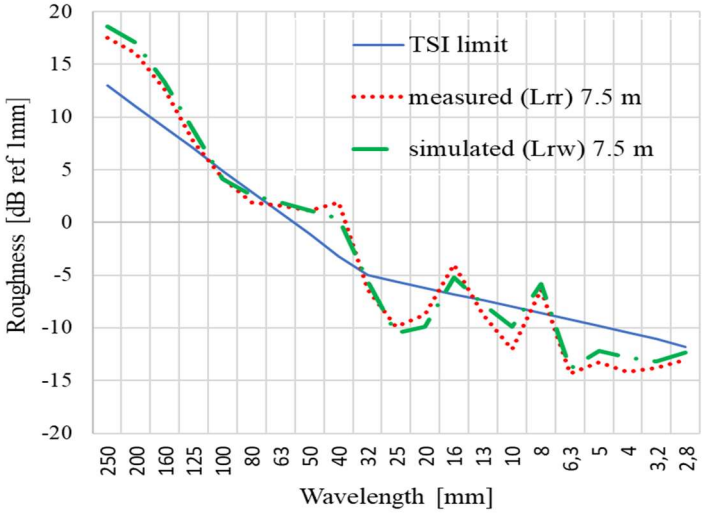

Fig. 2.9. Comparison between experimental (solid line) and simulated (dotted line) rail acoustic roughness determined for 7.5 rail roughness length.

Hence, Figs. 2.6-2.9 illustrate a notable alignment between graphs that show simulated and measured roughness, confirming that the deviations observed for skewness and kurtosis are within the range of admissibility and emphasize the robustness of the WM model in capturing the nuanced characteristics of the surface roughness.

Hereafter, the spacing parameters which quantify the horizontal features of the surface irregularities are presented in Table 2.2.

Spacing parameters play a crucial role in roughness analysis, surface texture or a range of manufacturing processes, such as metal forming, where they are essential for maintaining uniform lubrication and performance during material shaping. While these parameters are significant in specific industrial applications, their importance is less pronounced in the railway field. Nonetheless, they assume an important role in the field of tribology, where their evaluation is paramount for optimizing lubrication efficiency and surface interactions.

Table 2.2. Spacing parameter.

No param.	Parameters	Experimental data for 7.5m [mm]	Simulated data for 7.5m [mm]	Relative error [%]	Simulated data for 5m [mm]	Relative error [%]	Simulated data for 2.5m [mm]	Relative error [%]
				Spacing parameters				
1	High spot count (HSC) threshold 0.005 mm [counts]	3237	2965	8.403	1605	50.417	1042	67.810
2	Peak count (Pc) [counts]	244	230.000	5.738	194	20.492	150	38.525
3	Mean spacing of adjacent local peaks (S) [mm]	20.188	19.729	2.274	19.755	2.145	19.677	2.531
4	Mean spacing at mean line Sm [mm]	20.188	19.729	2.274	19.755	2.145	19.677	2.531
5	Number of intersections of the profile at the mean line (n(0))	62.000	68.000	-9.677	54.000	12.903	30.000	51.613
6	Number the peaks in the profile (m) [m/cm]	0.000	0.000	0.000	0.000	0.000	0.000	0.000
7	Number of inflection points (g) [g/ cm]	4.250	4.250	0.000	4.237	0.306	4.250	0.000
8	Mean radius of asperity rp [mm]	-0.000002	-0.0000018	10.000	-0.0000018	10.000	-0.0000018	10.250

The high number of points (HSC) is calculating by counting the number of high regions in a profile that exceeds either the midline or the level above the midline. The High Spot Count (HSC) shares similarities with the Peak Count (Pc), but the main difference between these two parameters is in the definition of the peak. For a peak to be counted in the Peak Count analysis, it must be succeeded by a valley that spans the entire bandwidth (upper and lower threshold). For the Peak Count, a threshold above and below the mean line is set at the same distance from the mean line, and only peaks above this threshold are considered. The thresholds were set to

± 0.05 mm. The thresholds are intended to limit the number of peaks to "substantial peaks" to produce more stable parameters. Parameters like Peak Count and High Spot Count find their primary application in tribology, where they play a crucial role in manufacturing processes and quality control for coatings.

Based on the findings discussed earlier, it becomes evident that when considering a length of 7.5 meters, the spacing parameters extracted from the simulated roughness profiles demonstrate a remarkable closeness with the experimental roughness profiles. This proximity is exemplified by a relative error that remains notably below the threshold of 10%.

As expected, as the measurement distance is progressively reduced, a discernible reduction in the count of these spacing parameters is observed.

It is noteworthy, however, that certain parameters, specifically the High Point Count (HSC) and Peak Count, exhibit relatively higher errors when evaluated at shorter lengths.

These parameters are particularly suited for scrutinizing the small metal material finishes and imperfections. Nonetheless, in the context of railway operations and the broader field of tribology, the emphasis often lies on broader-scale roughness attributes, and hence, these specific parameters might hold less relevance.

The hybrid parameters combine amplitude and spacing parameters and represent the last set of analysed parameters, as shown in Table 2.3.

Table 2.3. Hybrid parameters

No param.	Parameters	Experimental data for 7.5m [mm]	Simulated data for 7.5m [mm]	Relative error [%]	Simulated data for 5m [mm]	Relative error [%]	Simulated data for 2.5m [mm]	Relative error [%]
			Hybrid parameters					
1	Profile slope at mean line ɣ [degree]	-85.080	-88.170	-3.632	-87.867	-3.276	-81.03000	4.760
2	Mean slope of the profile Δa [degree]	0.092	0.094	-2.174	0.0870	5.435	0.086	6.522
3	RMS slope of the profile Δq [degree]	4.424	4.444	-0.452	4.426	-0.045	4.515	-2.057
4	Average wavelength (λa) [mm]	1.742	1.709	1.894	1.696	2.641	1.775	-1.894
5	RMS wave length (λq) [mm]	0.046	0.045	2.174	0.045	2.174	0.042	8.696
6	Relative length of the profile (Lo)	1.004	1.02	-1.594	1.020	-1.594	1.007	-0.299
7	Steepness factor of the profile (Sf)	0.0001068	0.000112	-4.869	0.00013	-21.723	0.00016	-49.813
8	Waviness factor pf the profile (Wf)	39.218	41.100	-4.799	41.659	-6.224	41.650	-6.201
9	Roughness height uniformity [mm]	0.009041	0.009170	-1.427	0.0093	-3.075	0.0053	41.378
10	Roughness height skewness hs	-0.143	-0.150	-4.895	-0.172	-20.280	-0.1090	23.776
11	Roughness pitch uniformity Pu [mm]	4.435	4.099	7.576	3.98	10.259	2.680	39.572
12	Roughness pitch skewness Ps	3.356	3.171	5.513	3.033	9.625	2.700	19.547

When considering a length of 7.5 meters, it becomes evident that the hybrid parameters extracted from the simulated roughness profiles, when compared to the experimental roughness profiles, consistently exhibit a convergence below a 10% relative error range. However, as the measurement distance is progressively reduced, a slight decrease in these hybrid parameters' count becomes evident.

The anticipated trend of decreasing the number of parameters with the reduced measurement distance is a natural result, as fewer data points are collected for the Comparison with experimental results. Notwithstanding this minor reduction, the simulated results consistently uphold a level of accuracy and alignment, particularly given the relatively limited

extent of its length. The robustness of the outcomes within the 7.5 meters distance preserves a comparable magnitude of values across the spectrum of analysed parameters and underscores the reliability of the method and its ability to provide valuable insights into the roughness characteristics under investigation.

The bearing area curve (BAC) is one of the most important analysis parameters in tribology, functioning as a statistical curve derived from the cumulative probability density of surface profile heights that can be calculated by integrating the probability density function. The BAC serves as a powerful tool to comprehend the connection between surface performance parameters and roughness (*Hamdi A., Merghache S. M. and Aliouane T., 2020, Babici L. M., Tudor A., 2019, He P. et al., 2021*), enabling insights into wear, friction (*N. F. M. Yusof, & Z. M. Ripin,2016*), pressure distribution, and material adhesion (*Pavelescu D., Tudor A., 2004*). Its significance extends to tribological studies, manufacturing process enhancement, and evaluation of functional surface coatings. Both measured and simulated roughness (Fig. 2.10) follow the same BAC allure and capture the roughness peaks in the contact area well. The fractal parameter *D* influences the bearing area curve of the shape and characteristics, reflecting the self-affine nature of the surface roughness.

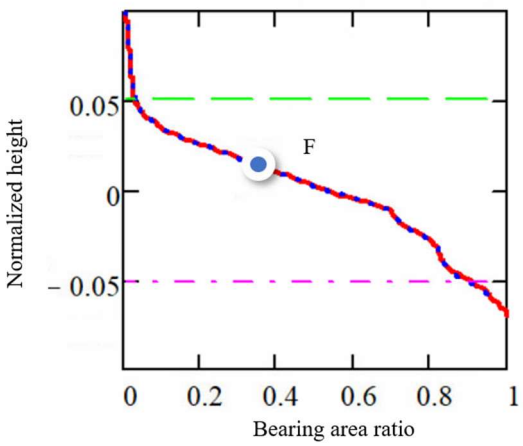

Fig. 2.10. Comparison between experimental (solid line) and simulated (dotted line) BAC.

For all parameters analysed, as the measurement length decreases, the resolution of the measuring instrument could become more critical. The measurement lengths of the experimental data can lead to challenges in capturing fine details and variations in the roughness profile, which can lead to fewer parameters obtained from simulated roughness in the relative error range of 10%.

The scale independence of the fractal method can be maintained in a certain range, but extreme length reductions can affect the accuracy of the measurements. While the fractal method provides a valuable way to model certain statistical properties of roughness, it may not fully capture all the intricate details and variations present on the surface at extremely small scales when reporting results to a scale of superior length. This thing could lead to the identification of a fewer number of accepted roughness parameters.

Next, an in-depth analysis was conducted by juxtaposing all the roughness parameters extracted from the initial 7.5 meters experimental section with simulated roughness profiles spanning a range of 2.5 to 7.5 meters. The simulation intervals were systematically established at increments of 500 mm, thereby encompassing various length scales. Moreover, this comprehensive investigation extended to a comparison involving the simulated roughness at a minimum measured length of 1 meter, a requirement specified by the EN 15610 standard. In each instance of simulated roughnesses, the fractal parameters D and G_f were determined.

All parameters calculated for the measured roughness profiles as well as those obtained from the simulated roughness that falls within a margin of error of 10%, are presented in detail in Table 4. This thorough examination emphasizes the effectiveness of the method in capturing and reproducing the characteristics of roughness while maintaining a high degree of fidelity to experimental data.

Table 2.4. Centralizer on the statistical parameters of experimental and simulated roughness that fall within the relative error of 10% (7.5m).

Distance measured	7.5 m	7 m	6.5 m	6 m	5.5 m	5 m	4.5	4	3.5	3	2.5	1
No. Amplitude param.	16/16	16/16	15/16	14/16	13/16	13/16	13/16	13/16	12/16	12/16	12/16	11/16
No. Spacing param.	8/8	7/8	6/8	6/8	6/8	6/8	5/8	5/8	5/8	5/8	5/8	2/8
No. Hybrid param.	12/12	11/12	10/12	10/12	10/12	10/12	8/12	7/12	7/12	7/12	7/12	5/12
Total no. parameter	**36/36**	**34/36**	**31/36**	**30/36**	**29/36**	**29/36**	**26/36**	**25/36**	**24/36**	**24/36**	**24/36**	**18/36**

After careful examination of the data presented in Table 2.4, it can be seen that all simulated roughness parameters fall within an error of 10% for the measured roughness length of 7.5 m. This harmonious approximation extends convincingly up to a distance of 5 m, where many parameters still show notable agreement.

It is important to acknowledge that certain parameters, notably those pertaining to spatial characteristics, exhibit deviations beyond the established 10% relative error threshold. Nevertheless, it is imperative to contextualize this deviation within the specific domain of railway analysis. In this particular context, the aforementioned spatial parameters hold negligible relevance. As the measurement distance is progressively truncated to 2.5 meters, a progressive reduction in the number of simulated roughness parameters maintaining this close alignment is observed. This trend culminates in a substantial decrease in the number of parameters when examining the simulated roughness at the 1 m length.

This correlation between distance and the number of parameters underlines the essential role of distance measurement in optimizing the fidelity of the simulated results, so one could conclude that, to acquire the most conclusive information in the roughness analysis, the minimum distance measured should be 2.5 m. To validate the scale independence of the roughness parameters obtained by the fractal method, roughness parameters from the simulated roughness calculated from four distinct test sections (30, 22.5, 15, and 7.5 meters) are compared to those from the measured roughness for the total test section of 30 meters. Notably, these lengths correspond to specific subsections of the first two and last two test sections, denoted as 1-2 and 3-4, respectively. Within the framework of assessing roughness characteristics over a length of 30 meters, Fig. 2.11 captures the roughness measured and simulated with the WM function, as well as it can be observed that simulated roughness closely mirrors the trajectory of the measured roughness, and this alignment substantiates a notable similarity between the two datasets, indicative of a compelling concordance. The WM function showcases a good ability to accurately predict and replicate the inherent roughness behaviour of rail surfaces.

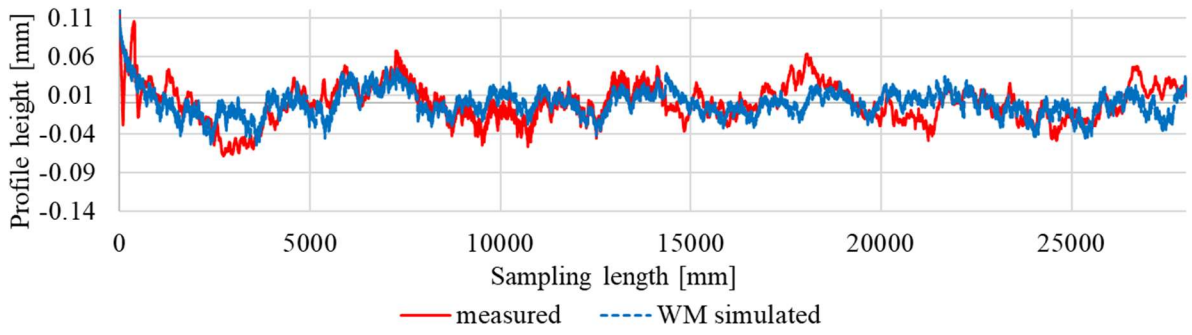

Fig. 2.11. Comparison between experimental (solid line)
and simulated (dotted line) rail roughness (30 m).

As anticipated, with the augmentation of the measurement length, both the measured and simulated roughness profiles exhibit an almost symmetrical Gaussian distribution (Fig. 2.12 a and b). A comparative analysis against the 7.5 meters benchmark highlights a noticeable enhancement in both Gaussian distributions. Furthermore, the simulated roughness profile manifests a subtle positive inclination, confined within the narrow range of 0 to 0.5.

In terms of kurtosis values, both the measured and simulated roughness profiles generated via the Weierstrass function maintain consistently low values, residing within the bracket of 0.5 to 1.5.

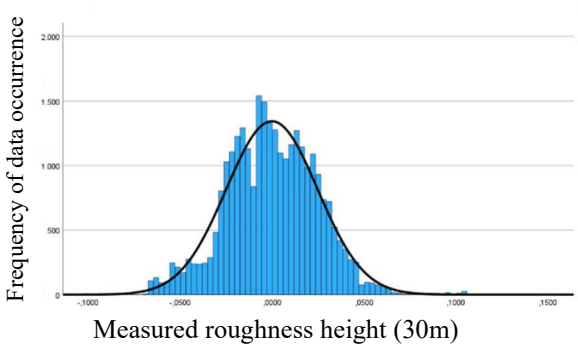

Fig. 2.12.a. Histogram with Gaussian distribution for measured roughness (30 m).

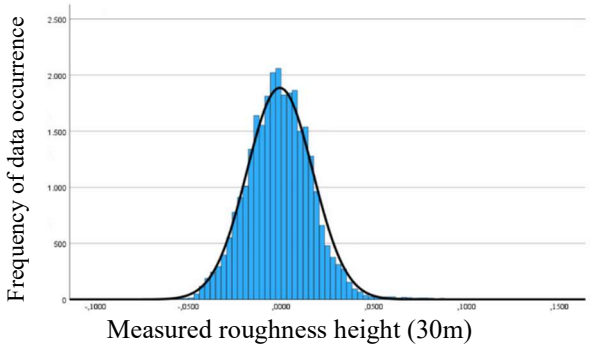

Fig. 2.12.b. Histogram with Gaussian distribution for simulated roughness (30 m).

Similarly, to Table 2.4, Table 2.5 shows the roughness parameters measured over the four distinct test sections, extending over a distance of 30 meters that involve a comparison with their simulated parameters, examined for lengths of 30, 22.5, and 15 meters, in the same 10% relative error.

Table 2.5. Centralizer on the statistical parameters of experimental and simulated roughness that fall within the relative error of 10% (30m).

Distance measured	30 m	22.5 m	15 m (sections 1-2)	15 m (sections 3-4)	7.5 m (first sections)
No. Amplitude parameter	16/16	15/16	14/16	14/16	14/16
No. Spacing parameter	4/8	4/8	4/8	4/8	3/8
No. Hybrid parameter	10/12	8/12	8/12	8/12	7/12
Total no. parameter	**30/36**	**26/36**	**26/36**	**26/36**	**24/36**

Thus, good matches of all simulated roughness parameters are observed at all lengths analysed, without significant variation in the number of parameters considered.

In Comparison to the 7.5 meters length, a marginal reduction is evident in the count of matching parameters. This limitation could have introduced a subtle decrease in measurement precision and subsequent result accuracy. Hence, strong correlations were observed between the actual and simulated roughness parameters, suggesting that the fractal method can be a valuable tool for predicting and analysing the roughness of the rail. This would have implications for track maintenance, noise prediction, wear analysis and overall route performance evaluation.

Considering these findings in conjunction with the guidelines outlined in the EN 15610 standard, it becomes evident that a measurement length of 7.5 meters suffices to provide the relevant roughness characteristics.

Regarding the analysis of the fractal parameters D and G_f, they are essential for the characterization of the rail roughness and have unique values for a certain surface state.

Figs. 2.13 and 2.14 showcase the variation of fractal parameters D and G_f within each test subsection spanning 2.5 - 7.5 m of test section no. 1 Fig. 13 illustrates the relatively constant nature of the D fractal parameter, while Fig. 14 displays the diminishing trend of parameter G_f (R^2 = 0.9986) with increasing measured length. This suggests that fractal parameter D remains unaffected by sampling length and instrument resolution, whereas the parameter G_f shows dependence on sampling length, as existing literature suggests (*Zhang X., Xu Y. and Jackson R. L., 2017, Berry M. V. and Lewis Z. V., 1980*).

The agreement between the simulated roughness generated from rail measurements within TCF Romania further validates these dependencies.

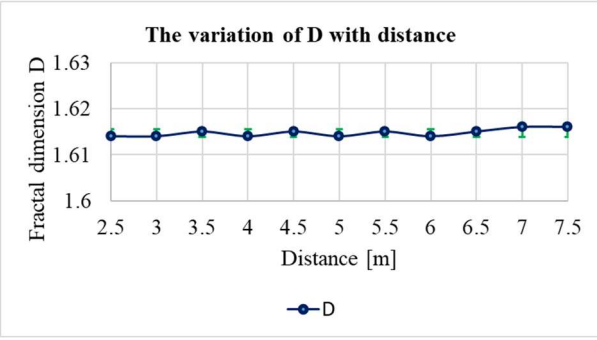

Fig. 2.13. Analysis of fractal dimension parameter D variation.

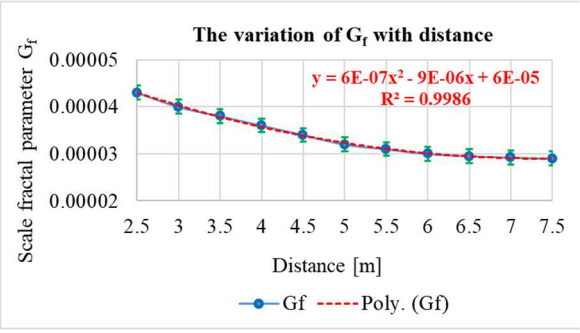

Fig. 2.14. Analysis of scaling parameter Gf variation

In summary, the entire length of 950 m within the Făurei Testing Centre, Romania, from km area 6 + 900 to km area 7 + 850, showcases an average fractal parameter *D* value of 1.615 ± 0.00045 (95% confidence interval) with a coefficient of variation (CV) of 0.044% and parameter G holds a value of $3.379 \times 10^{-5} \pm 2.367 \times 10^{-6}$ (95% confidence interval) with a coefficient of variation CV = 8.754%.

2.5. Conclusions

This study uses fractal modelling techniques to depict the roughness characteristics of the rails at the Făurei Test Centre in Romania examined in this study by means both the structure function and the Weierstrass Mandelbrot function to capture the intricate nature of the rail roughness effectively.

The analysis involved assessing and comparing 41 conventional statistical parameters of amplitude, spaces and hybrids and the rail acoustic roughness obtained from roughness measurements with the simulated fractal parameters.

Four sections of rail roughness testing, each comprising 7.5 meters, were systematically evaluated and divided into segments from 1 m to 7.5 meters long, with increases of 500 millimetres, in order to compare the roughness parameters obtained simulated with the experimental ones.

A comparison of the statistical parameters of the experimental measurements with the parameters simulated using the WM function showed that a representative number of these parameters fell within the relative error of 10%.

However, the fit of the number of simulated parameters relative to the measured parameters decreases as the measurement length decreases.

Specifically, when amplitude, spatial and hybrid parameters are considered for a measured roughness of 7.5 m, their correspondence to the simulated roughness at the same length is 100%, but with decreasing measured length, the matching of the number of parameters gradually decreases to 66.6% for a distance of 2.5 m, reaching 50% for a length of 1 m. This trend highlights the variability of the agreement between measured and simulated parameters based on the distance considered, taking into account that the simulated roughness for a length of 2.5 m is three times lower than the measured roughness against which the reported results were compared.

For a measured roughness of 30 m, the roughness parameters from the experimental measurements match the simulated parameters by 83.33% for the same length, which decreases to 66.66% for a simulated roughness of 7.5 m.

As the length of the measurement increases, both the measured and the simulated roughness profiles have almost symmetrical Gaussian distributions. Compared to the 7.5 meters reference, both Gaussian distributions are significantly improved.

Parameters such as ADF, ACF, PSD, and BAC exhibit close roughness equivalence through simulation with the WM function and the measured and simulated acoustic roughness exhibit close correspondence.

Although the roughness assessment of rails EN 15610: 2019 standard requires an optimal reference length of 7.5 m and a minimum length of 1 m, according to the simulated roughness results, the minimum roughness measurement length could be considered to be at least 2.5 m.

The results illustrate the relatively constant nature of the fractal parameter D, which remains unaffected by the length of the sampling and the resolution of the instrument, as well as the dependence of the Gf parameter on the measured length.

The WM function demonstrates a remarkable capacity to predict and emulate the roughness behaviour inherent in rail surfaces. This observation underscores its potential as a good tool for predicting and analysing rail roughness. In essence, the Weierstrass function emerges as a promising avenue for unravelling the intricacies of rail roughness, presenting a valuable asset in the roughness characterization.

The convergence of experimental measurements and simulated profiles underscores the power of the fractal approach in decrypting the complex behaviour of rail roughness.

Chapter 3

Fractal model of static friction behaviour in Hertzian roughness contact

3.1. Introduction

Contact mechanics, foundational in tribology, explores the analysis of stresses and deformations within the contact zone between bodies. Beginning with Hertz's pioneering work in 1882, which highlighted stress interactions between elastic solids, advanced methodologies have been developed to determine the real contact area in rough surfaces and to explore specific tribological phenomena such as wear, friction and dynamic contact.

Within the context of railway transportation, the Hertzian contact between wheel and rail not only governs vehicle efficiency but also impacts the longevity of the infrastructure. The pressure distribution within this contact area significantly influences wear patterns, noise generation, and vibrations, each affecting the overall lifespan of the components. Phenomena like elastic, elastoplastic, and plastic deformations, energy dissipation and the emergence of specific tribological challenges like the stick-slip phenomenon are crucial in such analyses.
The contact between wheel and rail implies a series of interactions between surface asperities, resulting in a real contact area that is smaller than the nominal contact area, both of which depend on the force applied due to elastic deformation and material properties. Consequently, it becomes necessary to characterise the relationship between this real contact area and the total contact load precisely.

For the determination of tribological contact characteristics, rough surfaces represented by a set of roughness of regular shape and variable height are modelled for assessing contact parameters such as actual pressure (or actual contact area), deformation, number of spots, static coefficient of friction and so on (N. B. Demkin and V. V. Izmailov, 1991).

The static friction coefficient (μs), a dimensionless parameter, is used in various fields and applications where understanding and controlling frictional forces between solid surfaces are essential, and it plays a crucial role in determining the onset of stick-slip motion.
The static coefficient of friction at the rail-wheel contact interface is a fundamental parameter in controlling and mitigating stick-slip behaviour in railway networks. Maintaining adequate adhesion and understanding the relationship between applied forces and the maximum static friction force is critical for safe and efficient rail operations. (Popov, V.L, 2009, Persson B.N.J., Tossati, E.,1995)

The actual contact area and surface roughness notably affect μ_s and slip behaviour. The interplay between these factors is important in diverse fields, including railway engineering and tribology. Furthermore, the static coefficient of friction, a critical factor in understanding slip resistance, has a rich history shaped by the contributions of philosophers, scientists, and

engineers across time. Visionaries such as da Vinci (1500), Amontons (1699), and Coulomb (1785) aimed to establish a universal friction law that could provide a logical framework for explaining how solid bodies resist sliding against each other. In broad terms, the Coulomb friction law postulates that the static friction coefficient remains constant. However, it is well-acknowledged that this coefficient is not an absolute constant; rather, it is influenced by both material properties and the specific system under consideration (J.M., You, P.N**.,** Chen, 2010; P.J., Blau, 2001), and variations can occur in response to changes in contact pressure. Greenwood and Williamson, known for their G.W. model, formulated a technique to ascertain the static friction coefficient (μs) as initially described in their 1966 publication. Drawing inspiration from Hertz's renowned elasticity theory, their method introduces a deterministic framework for analysing contact between surfaces. Notably, when considering the deformation of the surface roughness during contact, their model emphasises the importance of elastic deformation while excluding the potential for plastic deformation of asperities, especially under low loads. Based on the traditional G-W model, Chang (W. R. Chang et al., 1988) developed a coefficient model for metal joints, taking into account the tangential deformation resistance of the elastic node.

Subsequently, the Zhao, Maietta and Chang model (ZMC) (Zhao Y., 2000) incorporated all three deformation stages of the classical model. However, it showed some variation from the conclusions drawn by Kogut and Etision (FEM) (L., Kogut, and I., Etsion, 2002). The Kogut and Etzion model, designed to predict static friction in elastoplastic contacts with rough surfaces, prioritises parameters such as interaction and elastoplastic adhesion, distinguishing itself from traditional friction laws. Given the random structure of surface roughness, modelling such contacts is difficult, leading to exploring various statistical methods in the literature, where Greenwood and Williamson used semi-spherical asperities with Gaussian height distributions (J.A., Greenwood, 1971). This approach was later extended by researchers such as Whitehouse, Archard, Nayak, Onions, Bush and others (D.J., Whitehouse, 1970; J.F., Archard, 1970; P.R., Nayak, 1971; R.A., Onion, J.F., Archard, 1973; A.W., Bush, 1975; A.W., Bush, 1979; D.J., Whitehouse-1, 1978; D.J., Whitehouse-2, 1978, D.J., Whitehouse, 1982). However, these models largely depend on surface measurements, particularly the roughness curvature, which may vary due to the measurement resolution (B., Bhushan, C.Y., Poon., 1995; A., Almqvist, 2006).

Researchers have employed two primary approaches in studying surfaces with roughness and contact analysis: statistical analysis and fractal theory.

Statistical analysis involves using scale-dependent statistical parameters to describe the contact behaviour of hard surfaces. However, it is important to note that these statistical parameters can yield non-unique results for the same surface, as documented in references (Dowson D.,1991).

The fractal theory is proposed as an alternative approach in which fractal parameters, scale-independent, are utilised to characterise and simulate rough surfaces in contact, thereby providing an atomic-level detailed depiction of roughness. According to various studies (A. Majumdar, B. Bhushan, 1990; A. Majumdar, B. Bhushan, 1991; Y F Peng, 2009, Y. Yuan, 2016), this perspective is deemed invaluable in modelling contact behaviour. By integrating the Weierstrass-Mandelbrot (W-M) function to describe surface roughness across various scales, its popularity has been observed in various sectors, especially in the studies of friction and wear (Zhou, G. Y., Leu, M. C., and Blackmore, D. 1993; Yang, J. and Komvopoulos, K., 2005). However, the omission of the elastoplastic regime in the Majumdar-Bhushan (M.B.) model is noted as a significant limitation. Research on the static friction coefficient of surfaces with fractal roughness, which is known to influence stiffness and damping, has been documented (Zhang C., 2022), necessitating a thorough examination of their frictional characteristics.

While seeking to understand static friction, the development of an elastoplastic fractal model, which intricately delineates the interactions between contacting surfaces and roughness, has been highlighted. The Chang, Etsion, and Bogy (CEB) model, introduced in 1987 (W. R.Chang, I. Etsion, and D.B. Bogy, 1988), is acknowledged for not being confined merely to elastic behaviours but also encompassing the elastoplastic and plastic behaviours exhibited by asperities during contact. Despite CEB's comprehensive representation of interactions, limitations have been identified, including its potential inability to predict the static friction coefficient (μs). Further research by Chang and his colleagues in 1988 (W.R. Chang et al., 1988) indicated that as the normal load increases, μs decrease, thereby challenging the traditional Coulomb friction law (J.M. You, 2010). A critique often associated with the CEB model pertains to its possible oversight of the resistance provided by elastoplastic asperities against tangential loads, as pointed out by studies conducted by Kogut and Etsion (L. Kogut and Etsion, I., 2003, L. Kogut and I. Etsion, 2004). It is imperative to underline that both the G.W. and CEB models have been found to neglect the elastoplastic phase in their analyses.

Building on this, Sheng (X. Sheng et al.,1998) predicted the static friction coefficient using the M-B fractal model, but they overlooked the variations of fractal parameters D and G_f

with changing contact forces. Addressing this oversight, (J. Zhou et al., 2011) introduced a model that considers changes in fractal parameters relative to alterations in the contact area. In a parallel development, Kogut (L. Kogut and I. Etsion, 2002) formulated a static elastoplastic friction model that delved deep into the finite elements of elastoplastic contact and the adhesive nature of individual asperities. Furthering this exploration, Kogut and colleagues (Miao X. M., Huang X. D.,2014) employed the finite element method to study the interaction between a single roughness element and a rigid plane. This research birthed the K.E. model, which outlines a three-phase progression from elasticity through elastoplasticity to full plastic deformation. MORAG (Morag Y, Etsion I., 2007) presented a modified elastoplastic contact model for a single fractal roughness element. This model revealed that deformation, contact area, and the critical load of a single fractal roughness all vary with scale, transitioning from elastic to plastic contact mode with increasing loading and contact area. You (J.M. You, 2010) devised a statistical, computational model for the static friction between two surfaces in contact. This model takes into consideration various conditions of asperity deformation, including complete elasticity and elasticity combined with plasticity. Tian et al. (H. Tian, et al., 2011; H. Tian, et al., 2013-1; H. Tian, et al., 2013-2; H. Tian et al., 2014) enhanced fractal theory by building upon Luo's work (Sheng Xuanyu, Luo Jianbin, Wen Shizhu, 1997). They established a fractal pattern for normal load, friction force, and static coefficient, which offers a more comprehensive understanding of contact mechanics and friction dynamics. Zhang and colleagues (Lan G et al., 2012; Zhang Y et al., 2014; Lan G et al., 2021) formulated a fractal model for the friction behaviour of contacting surfaces, considering three deformation mechanisms: complete elasticity of asperities, complete elasticity with plasticity, and they also explored the impact of various factors on the contact status of the connecting surfaces. Building upon the traditional M-B model, Li and collaborators (Li X et al., 2019; Pan W, Li X, Wang X., 2020) and Hanaor (Hanaor D., Gan Y., and Einav I., 2016) introduced the elastic stage of asperities to establish a static friction coefficient. Subsequently, they refined this model by incorporating the domain expansion factor. They used numerical simulation to derive a nonlinear relationship between relevant factors, leading to an accurate prediction of the static friction coefficient. More recently, Zhang and colleagues (Zhang X, Zhang W, Wen S, et al. 2021) proposed a three-dimensional fractal pattern associated with the static friction scale of the contacting surfaces. This model successfully reconciled disparities between existing fractal or statistical models for static friction coefficients and experimental test results.

This research aims to explore the static coefficient of friction within the context of Hertzian contact between rail and wheel, employing a methodology based on fractal

approaches. The analysis is grounded in the Weierstrass-Mandelbrot model, which outlines the transition through four deformation states: elastic, the first two elastoplastic, and the fully plastic state. In this light, the static friction coefficient is considered to reflect an intrinsic property of the softer material in contact, with the surface microgeometry influenced by the fractal parameters D and Gf. Connecting these concepts, it should be noted that although the Hertzian contact surface is traditionally assumed to be homogeneous, this work enriches the perspective by considering fractal properties for the calculation of the actual contact area. This detail not only refines the understanding of the interactions between surfaces but also strengthens the existing model by including variations in roughness, allowing a more truthful representation of the contact performance of the system; thus, this static coefficient of friction is not only an essential measure of adhesion but also a barometer of performance in rail transport.

3.2. Static friction theoretical fractal model

Fractal characterisation of the equivalent roughness of the wheel and rail, is based on the Weierstrass Mandelbrot function (W.M.) (eq.5 chap. 2) and provides a more accurate description of how the surface roughness interacts at different scales during contact. Fractal analysis helps capture complex roughness details, including how asperities on different scales contribute to frictional forces. Using fractal analysis such as the W.M. function to characterise surface roughness, researchers gain a more comprehensive understanding of the complex interaction between surface roughness during Hertzian wheel/rail contact, which can help predict and mitigate stick-slip behaviour, which is crucial for the safe and efficient operation of trains and railway systems.

3.2.1. Analysis of contact with one asperity

The mechanical model of a single asperity is depicted through cosine waves, offering an understanding of surface roughness and contact mechanics at the microscopic level. Such models are often used in tribology and Hertzian contact mechanics, describing the intricate interaction between rough wheel-rail surfaces. Visualising a single asperity or surface irregularity can elucidate its shape and behaviour through cosine waves with varying amplitudes and wavelengths, thereby enhancing our comprehension of Hertzian contact phenomena.

Based on the W.M. function, with a wavelength of $l=1/\gamma^n$,

(l denotes a general wavelength or a characteristic scale applicable in a broad context, γ is a parameter that defines the frequency density in roughness analysis, and n is the integer number

of items gathered by the series during the roughness measurement process), and it indicates the total number of data points considered in the analysis); the shape of individual asperity deformation is described as: (Y. Yuan, 2016):

$$y(x) = G_f^{(D-1)} l^{2-D} \cos\frac{\pi x}{l},\ -\frac{l}{2} \le x \le \frac{l}{2} \tag{3.1}$$

where *y(x)* represents the height of the roughness profile, *D* represents the fractal parameter, *(*$1 < D < 2$*)*, and G_f is the characteristic scaling length.

This interaction can be simplified when the asperities contact, as Figure 3.1 depicts. In this representation, the contact of the wheel-rail interacting surfaces is condensed to a rigid rail featuring a rough texture. Fractal parameters characterise this textured profile of the surface, as the W-M function outlines.

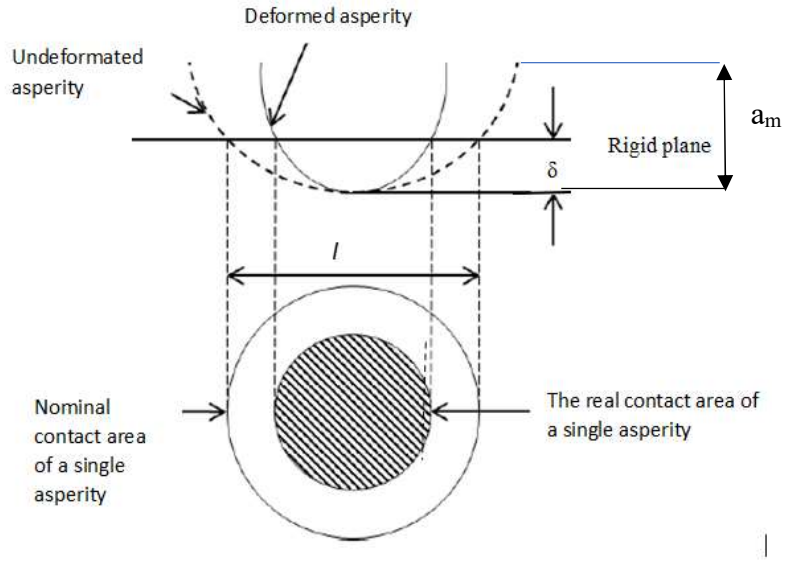

Fig. 3.1. Schematic model for asperity interaction.

The curvature radius R_a (Yuan, Y.,2016) at the peak of the asperity (one cosine) is:

$$R_a = \frac{l^D}{\pi^2 G_f^{(D-1)}}, \tag{3.2}$$

where the figure 3.1. illustrates the deformation of an individual asperity.

In this new perspective, *l* represents the specific base diameter of a fractal asperity at level *n* within the fractal hierarchy, reflecting the structural characteristic of the asperities at a certain level of fractal detail. This parameter is independent of the deformation δ and spans a range starting from zero up to the maximum amplitude, with $0 \le \delta \le a_m$.

The deformation (δ) and amplitude (a_m) can be expressed in the following manner (Y. Yuan, 2016):

$$\delta = G_f^{(D-1)} l^{2-D} \left(1 - \cos\frac{\pi r^2}{2l}\right),\ a_m = G_f^{(D-1)} l^{2-D}. \tag{3.3}$$

Individual asperity deformation in contact with the rail surface can be elastic, elastoplastic, and plastic.

3.2.1.1. Elastic deformation regime

For the elastic regime in the context of Hertzian contact between wheel and rail, the focus is on the reversible deformation of asperities under load. In this regime, the materials return to their original shape once the load is removed. The elasticity of the materials is fundamental for absorbing and distributing the stresses without causing permanent changes. It is critical to maintain the integrity of the wheel and rail surfaces under normal operating conditions and ensure the smooth transmission of forces during wheel-rail interactions.

In the elastic state for Hertzian contact involving a single spot, the contact load is distributed in a manner where deformations are entirely recoverable once the load is removed.

Based on the Hertz theory (Johnson K L., 1987), the critical deformation (δ_c) caused by an individual asperity, when in contact with a flat, rigid, smooth surface rail is:

$$\delta_c = G_f \left(\frac{2E}{k \cdot H_d}\right)^{\frac{2-D}{D-1}}, \tag{3.4}$$

where, H_d is the hardness of the softer material, k represents the coefficient related to the Poisson ratio of the wheel (Chang, W. R., Etsion, I., and Bogy, D. B, 1988) with k=0.454+0.41ν, and E is the equivalent Hertzian elastic modulus defined as:

$$\frac{1}{E} = \frac{1-\nu_1^2}{E_1} - \frac{1-\nu_2^2}{E_2}, \tag{3.5}$$

where E_1, E_2 and ν, ν_1, ν_2 are Young's modulus and Poisson's ratios of the wheel and rail materials, respectively, in the case of the rigid flat $E_2 \to \infty$.

When the deformation δ equals the critical value δ_c, the individual asperity undergoes elastic deformation. This is the point where the material responds to stress without undergoing permanent changes, returning to its original shape once the stress is removed. If the deformation δ is less than δ_c , the asperity remains within the purely elastic regime, meaning that the material's elastic limits are not exceeded, and no plastic deformation occurs.

Conversely, if δ exceeds δ_c, the asperity enters the elastoplastic or plastic regime. In this case, the asperity does not return to its initial size after the load is removed, indicating that the material has undergone plastic deformations. These deformations may continue to evolve towards a fully plastic regime, where the material completely loses its ability to return to its initial shape, undergoing permanent changes in its structure. Each of these regimes has significant implications for the behaviour of contacting surfaces and, therefore, for the static coefficient of friction and wear behaviour in mechanical systems.

3.2.1.1.1. Critical area

Based on the Majumdar Bhushan model (M.B. model) (Majumdar, A. and Bhushan, B., 1991), the critical contact area (a_c) concept associated with surface roughness deformation serves as a fundamental boundary that distinguishes between the regimes of elasticity and plasticity in contact mechanics. In other words, it provides a crucial demarcation point where the mechanical response of the materials transitions from elastic deformation to plastic deformation when surfaces come into contact, without taking into account the elastoplastic regime of a deformed roughness.

Given that the asperity's curvature radius is significantly larger than its amplitude, specifically R>>a_m (Li L, 2021; Caixia Z, 2022).

This critical contact area (a_c) and its dimensionless form a_{cs} are expressed as:

$$a_c = G_f{}^2 \left(\frac{2E}{kH_d} \right)^{2/(D-1)}, \; a_{cs} = \frac{G_{fs}{}^2}{\left(k \frac{k_{HE}}{2} \right)^{2/(D-1)}}, \; k_{HE} = \frac{H_d}{E}, \tag{3.6}$$

where, the dimensionless form are the expressions:

$$a_{cs} = \frac{a_c}{A_a}, G_{fs} = \frac{G_f}{\sqrt{A_a}}, \tag{3.7}$$

where A_a represents the nominal or apparent area of wheel-rail surfaces with fractal roughness, which refers to the apparent or macroscopic contact area and is the area one would observe without any magnification, essentially the projected area of one object onto the other, G_{fs} *represent Gf* dimensionless form, and k_{HE} is the hardness factor. The nominal area depends on the load applied due to elastic deformation and material properties and directly influences G_f.

3.2.1.1.2. Contact spot area

In this model, the asperity's deformation enters the plastic regime when the contact spot area of surfaces with fractal roughness a (with as its dimensionless form) is less than a_{cs}. In

contrast, if a_s exceeds a_{cs}, the regime shifts to an elastic state. The dimensionless contact spot area a_s and asperity deformation $\delta_s(a_s)$ have the following equations expressed by fractals:

$$a_s = \frac{a}{A_a},\ a_s = G_{fs}^{\frac{2D-2}{D-2}} \delta_s^{\frac{2}{2-D}}, \tag{3.8}$$

$$\delta_s = \frac{\delta}{\sqrt{A_a}}, \delta_s(a_s) = G_{fs}^{D-1} a_s^{2-D}. \tag{3.9}$$

Subsequently, the dimensionless contact load in the elastic state (P_{se}) may be expressed by fractals depending on the roughness corresponding to the contact dimensionless area a_s as follows:

$$P_{se}(a_s) = \frac{4\sqrt{\pi} G_{fs}^{D-1}}{3} a_s^{(3-D)/2},\ P_{se} = \frac{P_e}{A_a E}, \tag{3.10}$$

where, dimensionless P_{se} denote the contact loads of a distorted asperity in the elastic regime.

3.2.1.2. Elastoplastic deformation regime

In the context of Hertzian contact between wheel and rail, the elastoplastic regime is particularly significant as it determines how forces are transmitted and distributed across the contact asperities. This regime indicates the onset of plastic flow and can affect the static and dynamic coefficient of friction, as well as the wear of both the wheel and the rail. The critical factor here is the threshold at which the elastic deformation of the asperities transitions into plastic deformation. This is determined by the material properties of the asperities, such as hardness and yield strength. In railway engineering, understanding and managing this deformation regime is vital for optimizing wheel-rail contact to minimize wear and maintain traction, which directly contributes to the safety and efficiency of rail transport.

Next, the critical deformations for elastoplastic deformation's first and second stages are evaluated. As per the findings of Kogut (Kogut, L. and Etsion, I.,2004), when expressed dimensionless, the complete elastoplastic regime of a deformed one asperity falls within the range of $1 \leq \frac{\delta_s}{\delta_{cs}} \leq 110$. Here, δ_s represents the dimensionless asperity deformation, and δ_{cs} represents the dimensionless critical asperity deformation, completely dependent on the material property in which the following equations give δ_s and δ_{cs}:

$$\delta_s(a_s) = G_{fs}^{D-1} a_s^{\frac{2-D}{2}},\ \delta_{cs} = G_{fs}^{D-1} a_{cs}^{\frac{(2-D)}{2}}. \tag{3.11}$$

Furthermore, this entire elastoplastic regime is divided into two distinct phases: the first regime, where deformation values range from $1 \leq \frac{\delta_s}{\delta_{cs}} \leq 6$, the hemisphere undergoes mainly elastic deformation, indicating the onset of elastoplastic behavior. In the second regime, represented by $6 \leq \frac{\delta_s}{\delta_{cs}} \leq 110$, deformation is largely plastic, signifying a progression into a more advanced stage of elastoplastic deformation.

Also, the full elastic and plastic regime of a deformed asperity falls within the range of $0 \leq \delta_s \leq \delta_{cs}$, respectively $\delta_s \geq \delta_{cs}$.

These equations help us determine the dimensionless deformations and critical deformations of asperities in these specific regimes, aiding our understanding of the material behaviour during elastoplastic deformation.

Therefore, the full range of contact surfaces with fractal roughness behaviours for surfaces with fractal roughness with in the M.B. model (A. Majumdar, B. Bhushan,1991, J.M. You, 2010) can be reconfigured to include distinct regions: the completely elastic state, with $1 \leq \frac{a_s}{a_{cs}} \leq a_{ls}$, where a_{cs} represents dimensionless critical area, a_{ls} signifies the maximum area of actual contact between wheel and rail when an asperity undergoes deformation ($0 \leq a_{ls} \leq 1$), and this area is typically influenced by the shape and size of the asperities, as well as the applied forces and material properties. Following, appear initial elastoplastic stage $6^{1/(1-D)} \leq \frac{a_s}{a_{cs}} \leq 1$, subsequent elastoplastic phase, $110^{\frac{1}{1-D}} \leq \frac{a_s}{a_{cs}} \leq 6^{\frac{1}{1-D}}$ and final plastic stage, $0 \leq a_s \leq 110^{\frac{1}{1-D}} a_{cs}$.

Therefore, the area that separates the first elastoplastic stage from the second elastoplastic stage a_{cs2} and the area that separates the second stage of elastoplastic from the plastic stage (a_{cs1}) have the following equations:

$$a_{cs1} = 110^{\frac{1}{1-D}} a_{cs},\ a_{cs2} = 6^{\frac{1}{1-D}} a_{cs} \tag{3.12}$$

The dimensionless contact loads in the first and second elastoplastic regimes (P_{sep1}, P_{sep2}) may be expressed by fractals depending on the roughness corresponding to the contact dimensionless area a_s follows:

$$P_{sep1}(a_s) = \frac{2a_2}{3a_1} kk_{HE} G_{fs}^{2(D-1)(b_2-b_1)} \left(\frac{2}{kk_{HE}}\right)^{2(b_2-b_1)} a_s^{(1-D)(b_2-b_1)+1},\ P_{sep1} = \frac{P_{ep1}}{A_a E},$$

(3.13)

$$P_{sep2}(a_s)=\frac{2a_{2p}}{3a_{1p}}kk_{HE}G_{fs}^{2(D-1)(b_2p-b_1p)}\left(\frac{2}{kk_{HE}}\right)^{2(b_2p-b_1p)}a_s^{(1-D)(b_2p-b_1p)+1},P_{sep2}=\frac{P_{ep2}}{A_aE},$$

where $P_{s\text{ep1}}$ and $P_{s\text{ep2}}$, denote the contact loads of a distorted asperity in the first and second elastoplastic regimes, and a_1, b_1, a_2, b_2, $a_{1\text{p}}$, $b_{1\text{p}}$, $a_{2\text{p}}$ and $b_{2\text{p}}$ are the constant (Kogut, L. and Etsion, I. 2002), constants that are found in table no. 3.1.

Table 3.1. Value of constants for the various deformations of states

First elastoplastic state	a_1	a_2	b_1	b_2
	0.93	1.03	1.136	1.425
Second elastoplastic state	a_{1p}	a_{2p}	b_{1p}	b_{2p}
	0.94	1.4	1.146	1.263

3.2.1.3. Plastic deformation regime

Regarding the plastic regime, the focus is on the asperities' irreversible deformation when the applied load surpasses the yield point of the material. In this state, the asperities are permanently altered and do not return to their original shape post-load, affecting the topology of the contact surfaces. Such permanent changes are significant for the longevity of railway components, influencing wear patterns and maintenance schedules. Grasping the implications of the plastic regime is indispensable for engineering materials and components robust enough to endure the substantial loads encountered in rail transport without incurring damage that could precipitate operational failures.

The full plastic regime of a deformed asperity falls within the range $\delta_s \geq \delta_{cs}$.

The dimensionless contact load in the plastic regime ($P_{sp(a_s)}$) could be written as follows:

$$P_{sp}(a_s)=k_{HE}a_s,P_{sp}=\frac{P_p}{A_aE}, \tag{3.14}$$

where P_p, with dimensionless form, $P_{s\text{p}}$, denote the contact loads of a distorted asperity in the plastic regime.

Finally, the dimensionless total contact load (P_{st}) is given by:

$$P_{st}(D,G_{fs},a_s)=P_{se}(D,G_{fs},a_s)+P_{sep1}(D,G_{fs},a_s)+P_{sep2}(D,G_{fs},a_s)+P_{sp}(D,G_{fs},a_s) \tag{3.15}$$

when $\delta_s \geq \delta_{cs,}$ it follows that $a_s > a_{cs}$. This implies that if the contact area of a singular asperity exceeds the second critical elastoplastic contact zone, the asperity undergoes complete plastic deformation, with the relationship between load and area. These formulations capture the interplay between the contact area, the load on an asperity, and its interference across various conditions.

3.2.2. Real contact area

The real contact area is smaller than the contact spot because the contact pressure is not uniform across the contact spot. The real contact area depends on many factors, such as the wheel profile, rail profile, and the vertical load on the wheel.

The distribution function of the contact spot *n(a)* represents the distribution function of the contact spot area, which gives the probability that the contact spot size will be between *a* and *a+da* and is provided by the formula in the dimensionless form:

$$n_s = nA_a, \quad n_s(D, a_{ls}, a_s) = \frac{D}{2}\left(\frac{a_{1s}^{D/2}}{a_s^{D/2+1}}\right)\Phi_e(D)^{\frac{2-D}{2}}, \tag{3.16}$$

where n, and dimensionless form n_s represents the cumulative count of contact spots with areas greater than a specific size threshold denoted as area a_s and depends on the normal load. $\Phi_e(D)$ is the domain extension factor (Wang, S. and Komvopoulos, K., 2014; C. Zhang, 2022) associated with micro-contact size distribution, and it is linked to the fractal dimension (D) through the following formula:

$$\frac{\Phi_e^{\frac{2-D}{2}} - \left(1+\Phi_e^{\frac{-D}{2}}\right)^{\frac{D-2}{D}}}{\frac{(2-D)}{2}} = 1 \tag{3.17}$$

Using the insights the preceding analysis provides, the real contact area A_r is derived from the cumulative contributions of the contact areas corresponding to the four distinct regimes. Therefore, it can be computed using the following equation for A_r with its dimensionless form A_{rs}:

$$A_r = A_e + A_{ep1} + A_{ep2} + A_p \tag{3.18}$$

The following real area dimensionless are made:

$$A_{es} = \frac{A_e}{A_a}, A_{ep1s} = \frac{A_{ep1}}{A_a}, A_{ep2s} = \frac{A_{ep2}}{A_a}, A_{ps} = \frac{A_{ps}}{A_a},$$

$$A_{rs} = A_{es} + A_{ep1s} + A_{ep2s} + A_{ps} \tag{3.19}$$

Thus, the contact area for each deformation state is given by:

$$A_{es}(D, G_{fs}, a_{ls}) = \int_{a_{cs}}^{a_{1s}} a_s n_s(D, G_{fs}, a_{ls}) da_s, \; A_{ep1s}(D, G_{fs}, a_{ls}) = \int_{a_{cs2}}^{a_{cs}} a_s n_s(D, G_{fs}, a_{ls}) da_s \tag{3.20}$$

$$A_{ep2s}(D,G_{fs},a_{ls})=\int_{a_{cs1}}^{a_{cs2}} a_s n_s(D,G_{fs},a_{ls})da_s\,,\ A_{ps}(D,G_{fs},a_{ls})=\int_{0}^{a_{cs1}} a_s n_s(D,G_{fs},a_{ls})da_s$$

In this context, A_e, A_{ep1}, A_{ep2} and A_p, respectively A_{es}, A_{ep1s}, A_{ep2s}, and A_{ps} represent the contact area and dimensionless contact areas associated with the four distinct regimes and a_l and its dimensionless form a_{ls} represent the maximum contact spot area, determined by normal load.

By the principles laid out in the M.B. model (Majumdar, A. and Bhushan, B.,1991), the total normal load is constituted by the plastic and elastic load accumulation. Correspondingly, within the context of the present model, the total normal load denoted as F_n also emerges as the accumulation of the contact loads linked to the four regimes. Normal total load and its dimensionless forms could be elaborated upon as follows:

$$F_n = F_e + F_{ep1} + F_{ep2} + F_p \tag{3.21}$$

Normal contact force for the four deformation states in the dimensionless form is given by:

$$F_{es}(a_{ls})=\frac{F_e}{A_a E}\,,F_{ep1s}(a_{ls})=\frac{F_{ep1}}{A_a E}\,,F_{ep2s}(a_{ls})=\frac{F_{ep2}}{A_a E}\,,F_{ps}(a_{ls})=\frac{F_{ps}}{A_a E}\,,F_{ns}(a_{ls})=\frac{F_n}{A_a E}\,, \tag{3.22}$$

where F_{es}, F_{ep1s}, F_{ep2s}, *and* F_{ps} represent the contact loads corresponding to the four states, and F_{ns} is the dimensionless total contact load.

Finally, the contact normal for each deformation state is given by:

$$\begin{gathered}F_{es}(a_{ls})=\int_{a_{cs}}^{a_{1s}} P_{se}(a_s)n_s(a_{ls})da_s\,,F_{ep1s}(a_{ls})=\int_{a_{cs2}}^{a_{cs}} P_{ep1s}(a_s)n_s(a_{ls})da_s \\ F_{ep2s}(a_{ls})=\int_{a_{cs1}}^{a_{cs2}} P_{ep2s}(a_s)n_s(a_{ls})da_s\,,F_{ps}(a_{ls})=\int_{0}^{a_{cs1}} P_{ps}(a_s)n_s(a_{ls})da_s\end{gathered} \tag{3.23}$$

The equation gives the dimensionless total normal contact load for real contact area:

$$F_{nst}(a_{ls}) = F_{es}(a_{ls}) + F_{ep1s}(a_{ls}) + F_{ep2s}(a_{ls}) + F_{ps}(a_{ls}) \tag{3.24}$$

This formulation captures the comprehensive impact of various contact regimes on the cumulative normal load, offering a refined understanding of the contact behaviour between simulated surfaces with fractal roughness.

3.2.3. Tangential contact load and static friction coefficient

In the case of the friction analysis described above, the tangential load is the force that tries to initiate sliding or relative motion between wheel-rail contacting surfaces. Only the contacting asperities (microscopic surface irregularities) that undergo the fully elastic and the

first elastoplastic regimes are able to support the tangential load (Kogut, L. and Etsion, I., 2003; Kogut, L. and Etsion, I.,2004; You Y, 2010, (Caixia Zhang et al.,2022, You J M, 2010; Zhao, B., Xu, H., & Lu, X., 2019)). This means that only certain portions of the contacting surfaces, where the deformation remains within specific limits, can resist the force attempting to cause sliding. Furthermore, at the stage of sliding inception, the final yielding or plastic deformation occurs at the edge of the contact spot. This assumption is based on the distribution of the principal stresses within a deformed asperity at the interface (Caixia Zhang et al., 2022, You J M, 2010; Zhao, B., Xu, H., & Lu, X., 2019). This indicates that under the influence of the tangential load, the material experiences plastic flow, losing its ability to withstand further tangential loads without undergoing significant deformation.

The Tresca criterion determines the onset of plastic deformation by asserting that yielding starts when the material's maximum shear stress reaches a specific threshold (K. L. Johnson). Utilising this criterion, the maximum dimensionless tangential load, $T_{ts}\ (a_{ls})$, can be deduced for surfaces with fractal roughness.

$$T_{ts}(a_{ls}) = \frac{8k_{yE}}{\pi(6-3\upsilon)}\left(A_{es}(a_{ls}) + A_{ep1s}(a_{ls})\right) + \frac{8(2\nu-1)}{\pi(6-3\nu)}\left(F_{es}(a_{ls}) + F_{ep1s}(a_{ls})\right),$$

$$k_{yE} = \frac{\sigma_y}{E} \tag{3.25}$$

where k_{yE} represents the yield ratio and $\sigma_{y,}$ yield stress.

Then, the static friction coefficient $\mu_s(a_{ls})$ in the can be expressed as:

$$\mu_s(a_{ls}) = \frac{T_{tf}(a_{ls})}{F_{ns}(a_{ls})} \tag{3.26}$$

3.3. Experimental measurement

The flat specimen was made of unhardened and unalloyed steel, type R260 (EN 13674-1:2018) with a Brinell hardness of 285 HBW, and the cylinder specimen was made of surface-treated steel, type ER7 (EN 13262:2021), with a Brinell hardness of 265 HBW. These wear-resistant materials are used for the rails and wheels in railway systems. The surface quality of the specimens was initially evaluated by measuring the roughness with a Gaussian filter of 0.8 mm in the longitudinal (*L*) and transverse (*T*) directions with Surtronic 25 equipment**.** Thus, the average roughness values of the cylinder specimen were 0.734 µm (*L*) and 2.15 µm (*T*), and for the flat specimen, 1.13 µm (*L*) and 1.17 µm (T).

Similarly, the hardness values for the rail and wheel are comparable to those of the specimens made from the same type of material.

Rail roughness, measured at the Faurei Test Centre (see Chapter 2), was assessed using the m|rail trolley equipment, which integrates a coordinated acceleration sensor guided along the rail, consistently recording the roughness details with a vertical accuracy of 1 mm. In the same way, wheel roughness from the Lema locomotive class 048 was evaluated using the sophisticated m|wheel system. This device is manually moved across the wheel, capturing the intricacies of its roughness with a consistent vertical resolution of 1 mm (Fig.3.2).

(a) (b)

(c)

Fig. 3.2. Equipment m|wheel (a,b), Lema locomotive (c).

3.4. Methodology

In the framework of this study, we aimed to determine the static friction coefficient by employing a fractal approach, which combines the fundamental principles of fractal geometry with the mechanics of contact in both Hertzian wheel-rail systems and cylinder-plane specimen interactions involving rough surfaces.

Within the scope of this study, the μ_s were determined by employing a fractal approach, which combines the fundamental principles of fractal geometry with the mechanics of contact in Hertzian wheel-rail systems and cylinder-plane specimen interactions involving rough surfaces.

From this perspective, the static friction coefficient is perceived as an "intrinsic property" of the softer material of the two in contact within the context of a specific surface micro geometry, defined by the unique fractal parameters D and G_{fs}.

Fractal geometry provides an efficient method for characterizing contact surfaces. This approach is relevant for both the cylinder-plane contact samples in the laboratory and the wheel-rail contact. In the analysis of wheel-rail contact, attention has been focused on rail segment number 1, which was the one analyzed out of the four segments with varying roughness measured at CTF Faurei, as detailed in Chapter 2. Furthermore, wheel number 1, pertaining to axle one on the left side, sourced from the Lema locomotive class 048, has been selected for the wheel component involved in the study. A crucial step in the analysis is identifying the specific fractal parameters for the surfaces of the wheels and rails.

The structure-function (SF) method, following the methodology presented in Chapter 2, was applied to estimate these parameters, as detailed in equations 2.1 to 2.4. Subsequently, the equivalent fractal parameters were calculated to simplify the contact analysis between the two rough surfaces, whether the reference is to the cylinder-plane samples or the wheel-rail. The SF of the surface with equivalent roughness was determined using the following relation:

$$SF(\tau) = SF_r(\tau) + SF_w(\tau) \tag{3.27}$$

Then, the W.M. function outlined in eq. (2.5) from Chapter 2 was used, and their simulated equivalent roughness was derived, yielding fractal parameters. From these analyses, distinct sets of fractal parameters have resulted.

For the analysis of Hertzian contact parameters, three scenarios were investigated for cylinder-plane specimens with roughness, each associated with a specific normal force of 20 N, 40 N, and 60 N. Within the study of Hertzian wheel-rail contact, focus was directed to a specific case where a normal force of 103.00 kN was applied to wheel number one. This wheel,

belonging to axle one on the left side, originates from a Lema electric locomotive equipped with a Co-Co wheel arrangement featuring two bogies, six axles, and a total of twelve wheels.

The nominal areas (A_{a1}- A_{a4}) for the cylinder-plane material pairs, as well as the wheel-rail pairs, were determined based on the Hertzian contact semi-axes of the wheel and the cylinder, the applied external forces, and the material properties of the specimens (Esveld, C, Thompson, D. J., 2009; Otero Yugat, J., 2009).

Similarly, the dimensionless fractal parameters, G_{fs1}- G_{fs4}, were determined for each case, directly dependent on the nominal area (eq.3.7). The analysis encompassed four deformation regimes: elastic, first elastoplastic, second elastoplastic, and fully plastic, culminating in the

determination of the static friction coefficient for these four scenarios.

3.5. Results and discussions

The results of the equivalent fractal parameters and the contact parameters used for the specimens cylinder-plane and wheel-rail contacts can be found in Table 3.2.

Table 3.2. Overview of Fractal Parameters and Contact Mechanics Characteristics

Parameter	Value
Equivalent fractal parameter D for cylinder-plane	1.636
Equivalent fractal parameter D for wheel/rail	1.661
Equivalent scale parameter G_f for cylinder-plane	$1.652*10^{-7}$
Equivalent scale parameter G_f for wheel-rail	$1.389*10^{-7}$
Normal load (F_{n1}) cylinder plane contact [N]	20
Normal load (F_{n2}) cylinder plane contact [N]	40
Normal load (F_{n3}) cylinder plane contact [N]	60
Normal load (F_{n4}) for wheel-rail contact [N]	103.000
Nominal area A_{a1} for cilynder-plane under F_{n1} mm^2	0.528
Nominal area A_{a2} for cilynder-plane under F_{n2} mm^2	0.746
Nominal area A_{a3} for cylinder-plane contact under F_{n3} mm^2	0.914
Nominal area A_{a4} for wheel-rail contact under F_{n4} mm^2	208.7
Dimensionless equivalent scale parameter G_{fs1} under F_{n1}	$1.652*10^{-7}$
Dimensionless equivalent scale parameter G_{fs2} under F_{n2}	$1.389*10^{-7}$
Dimensionless equivalent scale parameter G_{fs3} under F_{n3}	$1.255*10^{-7}$
Dimensionless equivalent scale parameter G_{fs4} under F_{n4}	$8.653*10^{-6}$

Average cylinder specimen roughness [mm]	0.000734
Average plane specimen roughness [mm]	0.00113
Average wheel roughness [mm]	0.0025
Average rail roughness [mm]	0.026
Cylinder radius (R_d) [mm]	27.5
Cylinder width (B) [mm]	11.5
Wheel diameter (d) [mm]	920
Hertzian contact semi-axis (b_h) for cylinder specimen (20N) [mm]	0.023
Hertzian contact semi-axis (b_h) for cylinder specimen (40N) [mm]	0.032
Hertzian contact semi-axis (b_h) for cylinder specimen (60N) [mm]	0.04
Hertzian contact semi-axis a [mm]	6.4
Hertzian contact semi-axis b wheel [mm]	5.8
Hardness factor (k_{HE})	0.01
Young's modulus *(E)*	$2.1 \cdot 10^5$ [N/mm^2]
Poisson's ratios *(ν)*	0.3

All deformation regimes were analysed to determine the static friction coefficient and contact parameters considering different values of the dimensionless scale parameter G_{fs} and the fractal parameter D.

3.5.1 Outcomes of the Experimental Analysis

In the elastic regime, the value for a_{cs} in relation to the fractal parameter D and δ_{cs} for cylinder-plane specimens and wheel-rail under their forces can be seen in Table 3.2.

Table 3.3. Fractal parameters and critical characteristics for cylinder-plane and wheel-rail contact at various normal forces.

Specimen/ Normal force	Cylinder-plane/$F_{n1\ (20N)}$	Cylinder-plane/$F_{n2\ (40N)}$	Cylinder-plane/$F_{n3\ (60N)}$	Wheel-rail contact/ $F_{n4\ (100000N)}$
		Parameters		
D	1.637	1.637	1.637	1.661
a_{cs}	$5.023 \cdot 10^{-6}$	$3.552 \cdot 10^{-6}$	$2.9 \cdot 10^{-6}$	$6.094 \cdot 10^{-4}$
δ_{cs}	$5.225 \cdot 10^{-6}$	$4.394 \cdot 10^{-6}$	$3.97 \cdot 10^{-6}$	$1.937 \cdot 10^{-4}$

Table 3.2 shows that, in the case of cylinder-plane contact, the dimensionless critical area (a_{cs1}- a_{cs3}) decreases as the normal force increases, indicating an increased stress concentration and a reduction in the contact area. This highlights the direct influence of the

normal force and the fractal parameter G_{fs} on the characteristics of the contact zone. On the other hand, when subjected to a high normal force, a change in the surfaces' behaviour is observed in the case of wheel-rail contact. The tendency is toward a larger contact area and a more widespread distribution of asperities across the contact surface due to higher fractal parameters D and G_{fs} values. This adaptation reflects how greater forces influence contact characteristics by altering the fractal geometry of the surface.

Also, a similar trend can be identified, where a correlation between the dimensionless critical area a_{cs} and the critical deformation δ_{cs} is in the elastic regime.

The value for elastic contact force P_{se} in relation to the fractal parameter D for cylinder-plane specimens and wheel-rail under their forces can be seen in Table 3.3.

Table 3.4. Spot area (a_s) and elastic contact force (P_{se}) for cylinder-plane and wheel-rail contact at various normal loads.

Specimen/ Normal force	Cylinder-plane/$F_{n1\ (20N)}$	Cylinder-plane/$F_{n2\ (40N)}$	Cylinder-plane/$F_{n3\ (60N)}$	Wheel-rail contact/ $F_{n4\ (100000N)}$
		Parameters		
D	1.637	1.637	1.637	1.661
a_s	$1.757 \cdot 10^{-5}$	$1.757 \cdot 10^{-5}$	$1.757 \cdot 10^{-5}$	$1.757 \cdot 10^{-5}$
P_{se}	$6.497 \cdot 10^{-8}$	$5.818 \cdot 10^{-8}$	$5.454 \cdot 10^{-8}$	$6.972 \cdot 10^{-7}$

As observed in the data from Table 3.3, for cylinder-plane contact, the elastic contact force (P_{se1}) under a smaller normal force (F_{n1}) is noted to be slightly greater than P_{se3} under a larger normal force (F_{n3}), influenced by the decreasing fractal parameter (G_{fs}) as the force increases. A lower normal force leads to a pressure distribution over a larger surface area, resulting in a higher P_{se1}. With an increase in normal force, the contact area is observed to become more concentrated, which leads to a slight reduction in P_{se}. For wheel-rail contact, the increased value of P_{se4} is determined by both the rise in normal force and the higher value of G_{fs}.

In the elastoplastic regime, the value for critical a_{cs1}, a_{cs2} and contact load (P_{sep1}, P_{sep2}) in relation to the fractal parameter D and a_s for cylinder-plane specimens and wheel-rail under their forces can be seen in Table 3.4.

Table 3.5. Critical area (a_{cs1}, a_{cs2}) and contact load (P_{sep1}, P_{sep2}) in elastoplastic regime.

Specimen/ Normal force	Cylinder-plane/$F_{n1\ (20N)}$	Cylinder-plane/$F_{n2\ (40N)}$	Cylinder-plane/$F_{n3\ (60N)}$	Wheel-rail contact/ $F_{n4\ (100000N)}$
		Parameters		
D	1.637	1.637	1.637	1.661
a_{cs1}	$3.13\cdot10^{-9}$	$2.12\cdot10^{-9}$	$1.81\cdot10^{-9}$	$5.63\cdot10^{-6}$
a_{cs2}	$3.01\cdot10^{-7}$	$2.13\cdot10^{-7}$	$1.74\cdot10^{-7}$	0.000459
P_{sep1}	$4.8\cdot10^{-8}$	$4.51\cdot10^{-8}$	$4.34\cdot10^{-8}$	$1.89\cdot10^{-8}$
P_{sep2}	$7.41\cdot10^{-8}$	$7.22\cdot10^{-8}$	$7.11\cdot10^{-8}$	$1.29\cdot10^{-7}$

In the elastoplastic regime, an analysis of the experimental results presented in Table 3.4 shows varying behaviours of the critical areas (acs1 and acs2) and contact loads (P_{sep1} and P_{sep2}) in relation to the fractal dimension D and the dimensionless spot area as. For the cylinder-plane specimens under increasing normal forces (F_{n1}, F_{n2}, F_{n3}), there is a decrease in both a_{cs1}, a_{cs2}, P_{sep1}, and P_{sep2}, indicating a compaction tendency and an increase in material resistance under higher loads. This can be explained by the flattening and deformation of asperities under greater normal forces, reducing effective critical area and a more uniform distribution of the load. In contrast, for the wheel-rail contact subjected to a significantly larger normal force (F_{n4}), there is an increase in the values of a_{cs1} and a_{cs2}, a_s well as P_{sep1} and P_{sep2}. This could be due to a load regime where plastic deformation is so advanced that the asperities are completely flattened, resulting in a smoother surface with a larger contact area and a different load distribution. This effect is exacerbated by the high normal force typical of railway systems, which may induce different material behaviour due to its intrinsic properties and the interactions between wheels and rails.

As D and as vary, a_{cs} and P_{sep} reflect how the surfaces adapt and respond to the applied forces, indicating a close link between material properties, loading conditions, and contact behaviour in the elastoplastic regime, as evidenced by the experimental results for both cylinder-plane and wheel-rail contacts.

In the plastic regime, the contact load P_{sp}, in relation to the fractal parameter D and a_s for cylinder-plane specimens and wheel-rail under their forces, can be seen in Table 3.5.

Table 3.6. Contact load (P_{sp}) in the plastic regime.

Specimen/ Normal force	Cylinder-plane/$F_{n1\ (20N)}$	Cylinder-plane/$F_{n2\ (40N)}$	Cylinder-plane/$F_{n3\ (60N)}$	Wheel-rail contact/ $F_{n4\ (100000N)}$
		Parameters		
D	1.637	1.637	1.637	1.661
P_{sp}	$1.757 \cdot 10^{-7}$	$1.757 \cdot 10^{-7}$	$1.757 \cdot 10^{-7}$	$1.757 \cdot 10^{-7}$

In the plastic regime, as shown in Table 3.5, the contact load P_{sp} remains constant regardless of the variations in the fractal parameter G_f or the spot area as, across all types of samples tested, whether they are cylinder-plane or wheel-rail contacts, under various applied forces. This constancy in the contact load underscores that once surfaces enter the plastic regime, they no longer respond to the subtleties of roughness described by G_f nor to changes in the actual contact area.

Once the asperities are flattened through plastic deformation, they become less significant for contact behaviour, and the roughness no longer contributes to the total load in a measurable way. Thus, the value of P_{sp} remains unchanged with respect to Gf and when considering variations in a_s because the macroscopic effects of material deformation in contact predominate. This means that in the plastic stage, the interactions between asperities and their impact on contact load are mitigated by the extensive deformation, leading to a uniform load distribution. This suggests that under the conditions of advanced plastic deformation, the intrinsic material characteristics and the extent of the contact area become the dominant factors in determining the contact load, while the influence of microscopic details is diminished. Therefore, Psp reflects more on the direct effects of the applied load and overall deformation than the microstructural specifics of the surfaces.

3.5.2. Elastic deformation regime

3.5.2.1. Critical area

In this section, the first presentation covers the variation of the dimensionless critical area (a_{cs}) in relation to the fractal parameter D and the dimensionless critical deformation (δ_{cs}), as illustrated in Figures 3.2(a,b). The determination of a_{cs} is conducted in accordance with Equation 3.7, and δ_{cs} is calculated following Equation 3.11.

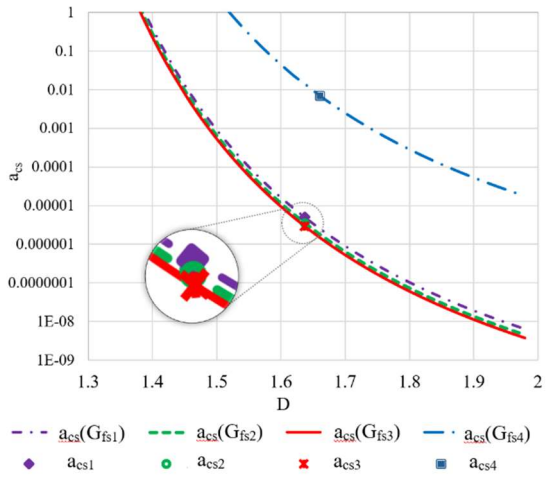

Fig. 3.2. (a) Variation critical area a_{cs} with variable G_{fs} and D fractal parameters

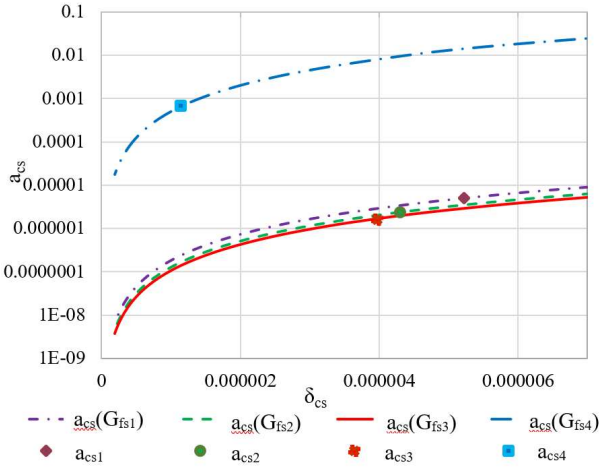

Fig. 3.2. (b) Variation critical area a_{cs} with deformation δcs with variable G_{fs} and D is constant

In Figure 3.2.a, a smaller G_{fs} indicates a higher critical ac, while a reduced D makes asperities less sharp. Their combined effect leads to an increased contact area in the elastic regime when a load is applied. Rounded asperities deform elastically over a broader area before achieving their elastic threshold, enlarging the critical elastic area.

In Figure 3.2.b, where D is held constant, the critical area (a_{cs}) growth coincides with increased critical deformation δ_{cs} and augmented G_{fs} within the elastic regime, underscoring an augmented elastic response.

Subsequently, Figures 3.3 (a,b) depict the variation of the elastic contact force P_{se} concerning the fractal parameter D and the spot area a_s. The elastic contact force P_{se} is determined in accordance with Equation 3.10, and the spot area a_s. is calculated following Equation 3.8.

A smaller G_{fs} suggests a larger critical area, while a reduced D makes the asperities smoother. Their combined effect increases the contact area in the elastic regime under an applied load. Asperities deform over a wider area before reaching their elastic threshold, thus expanding the critical elastic area. When D is constant, the critical area (a_{cs}) increase coincides with an increase in critical deformation δ_{cs} and an increase in G_{fs} in the elastic regime, highlighting an enhanced elastic response.

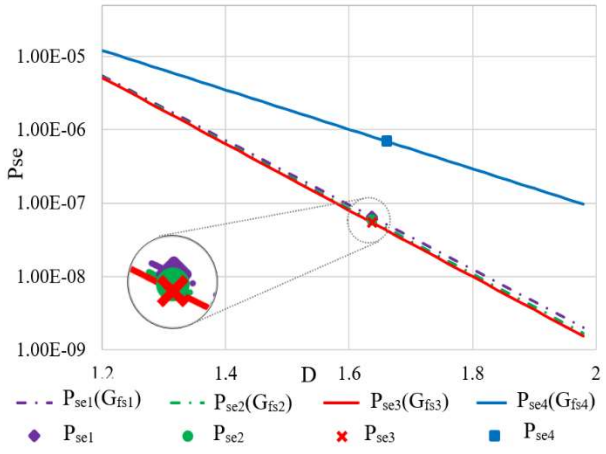

Fig. 3.3. (a) Variation contact load P_{se} with D variable.

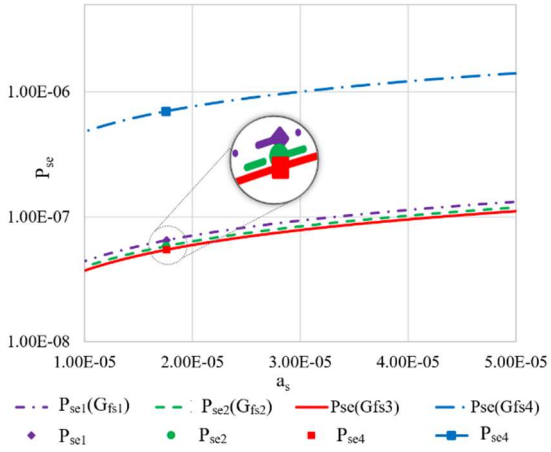

Fig. 3.3. (b) Variation contact load P_{se} with spot area a_s variable.

In Figure 3.3(a), an enhanced dimensionless elastic contact force (P_{se}) is associated with smaller fractal dimensions (D), which denote smoother surfaces, and when paired with larger scale parameters (G_{fs}), an expansion of the contact area within the elastic regime is witnessed, leading to an improved contact load. On the other hand, elevated D values, which suggest pronounced surface irregularities in conjunction with larger G_{fs}, result in a diminished contact force. This reduction in force is attributed to interactions primarily occurring at the most prominent tips of the surface roughness. Consequently, a larger D, coupled with the smallest G_{fs}, is linked to a decrease in the elastic contact force.

Observations of Figure 3.3b confirm that the dimensionless elastic contact force (P_{se}) increases with the enlargement of the contact spot area (a_s). This phenomenon is also evident in the wheel-rail contact. However, in the case of cylinder-plane specimens, a decrease in P_{se} with an increase in the normal force indicates a concentration of pressure in a smaller contact area and a more intense interaction at the microscopic level. This interaction is likely influenced by a restricted distribution of the load and, more specifically, by the influence of the fractal parameter G_{fs}, which decreases as the force increases, underscoring the essential role of fractal parameters in contact behaviour. Also, in the studies on cylinder-plane specimens and wheel-rail contact, an interesting phenomenon has been observed: the size of the Hertzian contact spot area remains unchanged despite variations in the normal force and changes in the fractal parameters D and G_{fs}. This defies the expectations set by Hertz's theory, which predicts that the contact area should vary with the applied force. The consistent size of the contact spot can be attributed to several factors. Firstly, the intrinsic material properties of the subjects under investigation likely play a crucial role in this consistent behaviour. They may exhibit

viscoelastic characteristics or other mechanical qualities that facilitate stress redistribution in a manner that constrains the alteration of the contact spot size.

Furthermore, surface interactions, such as adhesive forces, might keep the contact spot consistent, even when the load conditions fluctuate. On the other hand, changes in the fractal parameters that describe the microscopic scale asperities might not significantly affect the macroscopic contact spot. This could be due to a saturation effect or a plateauing of the elastic deformation of the material capacity, which becomes dominant before any substantial changes in the contact area can occur.

Thus, this detailed analysis of P_{se} behaviour in relation to fractal parameters and applied load not only highlights their impact on the contact characteristics of materials under varied loading conditions but also emphasizes the need to consider the transition towards elastoplastic behaviour for a comprehensive understanding of interactions in the Hertzian contact.

3.5.2.2. Elastoplastic deformation regime

The irreversible changes in material behaviour under load can identify the transition into the elastoplastic regime. Even as the fractal parameters D and Gfs remain constant across all stages of deformation, exceeding the critical deformation value (δcs) signals a shift from purely elastic behaviour to an elastoplastic one. This threshold is defined by the onset of permanent deformations, where the material fails to return to its original shape after the load is removed. The phenomenon is typified by an inflexion point on the stress-strain curve, known as the yield point, marking where the material begins to exhibit a mix of elastic and plastic properties.

Subsequently, Figures 3.4 (a,b) also display the variation of the critical areas in the elastoplastic regime, represented as a_{cs1} and a_{cs2}, and their relationship with the D and G_{fs} fractal parameters, as described in Equation 3.12.

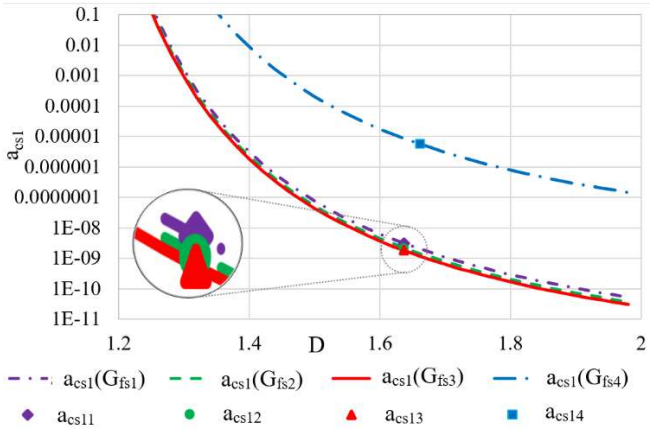

Fig. 3.4. (a) Variation critical area a_{cs1} with D and G_{fs} fractal parameters.

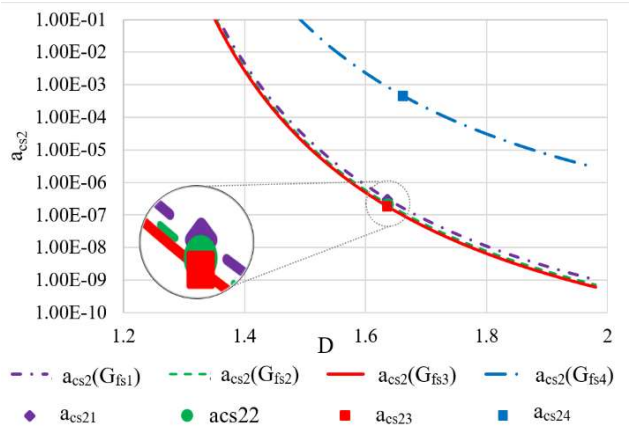

Fig. 3.4. (b) Variation critical area a_{cs2} with D and G_{fs} fractal parameters.

The interaction between fractal parameters and surface roughness significantly affects the transition from elastic to plastic deformation, also known as the critical area, as illustrated in Figure 3.4 (a, b).

Surface roughness, defined by asperity height, shape, and distribution, dictates how two surfaces interact. Less pronounced asperities (indicating smaller roughness) mean that stress gets distributed over a broader area before leading to plastic deformation. Such asperities can sustain more elastic deformation due to reduced stress concentration at their tips. Therefore, with smaller roughness, respectively, a low value for D and G_{fs}, a larger critical area (a_{cs1}, a_{cs2}) is observed before the onset of plastic deformation. The inherent properties of the material further modify this behaviour, with some showing pronounced changes with roughness variations, while others remain relatively consistent.

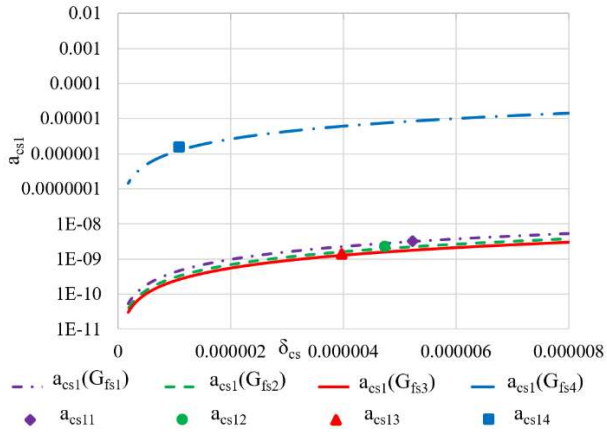

Fig. 3.5. (a) Variation critical area a_{cs1} with deformation δ_{cs}.

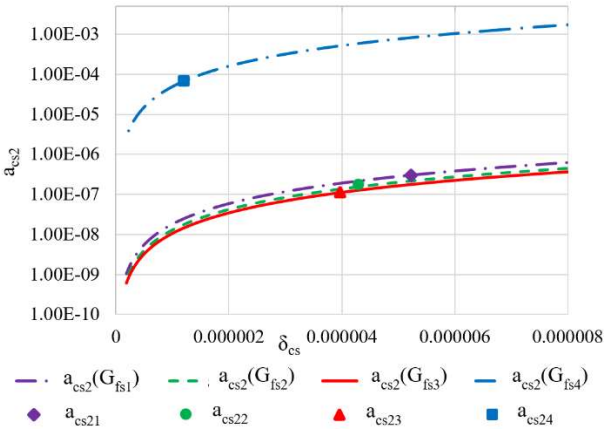

Fig. 3.5. (b) Variation critical area a_{cs2} with deformation δ_{cs}.

The interaction between surface roughness and fractal parameters plays a crucial role in determining the shift from elastic to plastic deformation. This is particularly evident when the

fractal roughness parameter G_{fs} is reduced. This relationship is clearly depicted in Figures 3.5 (a, b), which are following Equations 3.11 and 3.12. The specific attributes of the asperities, defining surface characteristics, significantly affect the mechanics of surface interactions.

Smoother surfaces result in stress dispersion across a larger area, delaying the onset of plastic deformation. This translates to a more extensive critical area (a_{cs1}, a_{cs2}) during this phase. These patterns in Figures 3.5 (a, b) align with trends seen in Figure 3.2b, mapping critical areas against critical deformations.

Following this, the contact load variations in the elastoplastic regime, denoted as P_{sep1} and P_{sep2}, are showcased in relation to the fractal parameter D and spot area as presented in subsequent figures 3.6 (a,b) and Equation 3.13.

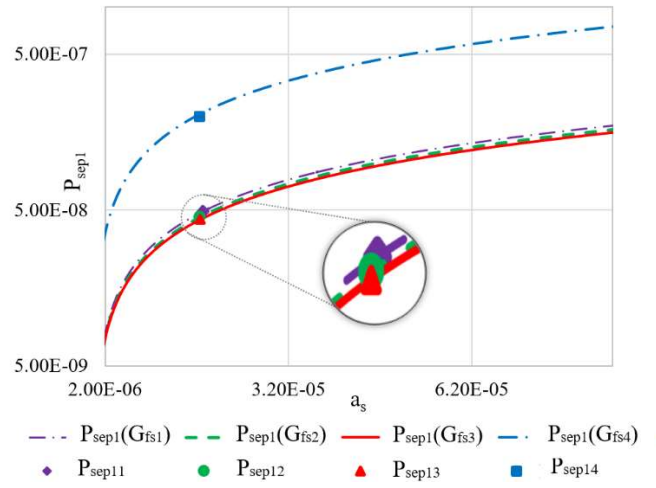

Fig. 3.6. (a) Variation contact load P_{sep1} with variable D and G_{fs} fractal parameters.

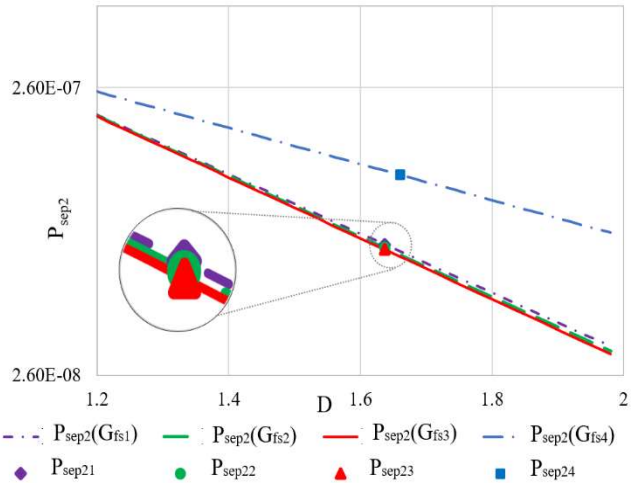

Fig. 3.6. (b) Variation contact load P_{sep2} with variable D and G_{fs} fractal parameters.

A higher fractal parameter D in this range signifies a rougher surface topology. With more irregular surfaces, there are more asperities. However, not all asperities will make adequate contact. The more pronounced roughness (higher D) means the asperities that do come into contact might be those that are taller or more prominent, leading to smaller Psep1, as they carry the bulk of the load and potentially undergo greater local deformations (Figure 3.6. (a)). A larger G_{fs} implies more pronounced asperities. When these asperities are pressed against a surface, more of them interact, leading to a higher P_{sep1}. A decrease in D leads to a slightly smoother surface, and this condition can lead to a broader distribution of load across many asperities, thereby raising the P_{sep1}. The spike in P_{sep1} might be due to this wider distribution and the engagement of many more asperities. The roughness level is very low for the case where D is between 1.1-1.3, and the force distribution across asperities might be such that none deforms significantly. Hence, the roughness features remain largely unchanged.

Regarding the similarity of P_{sep1} with P_{sep2} (Figure 3.6. (b) and elaborated through Equations 3.8 and 3.13), while the foundational principles remain the same, the interaction forces and deformations are more pronounced due to more in-depth elastoplastic behaviour. A decrease in D in this regime results in a rise in P_{sep2} compared to P_{sep1}.

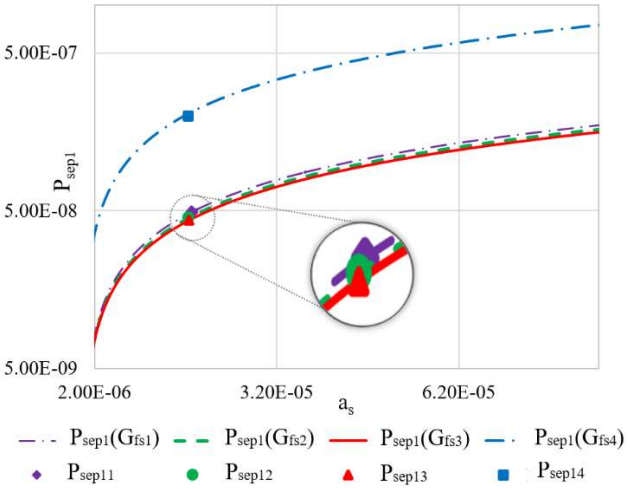

Fig. 3.7. (a) Variation contact load P_{sep1} with variable D and spot area a_s.

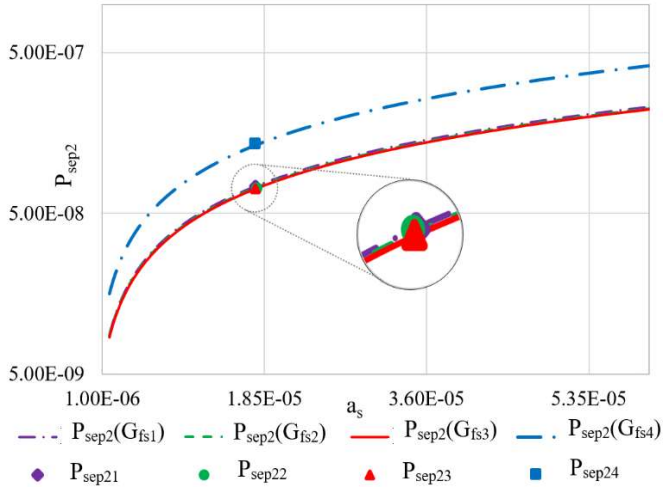

Fig. 3.7. (a) Variation contact load P_{sep2} with variable D and spot area a_s.

Figures 3.7 (a, b) depict the first and second elastoplastic regimes. There is a diminished contact area for a higher D value and G_{fs} constant (a_s). Conversely, this contact load decreases as D decreases, following the same trend as Figure 3.3.(b). This trend illustrates the profound influence of fractal dimension D on contact mechanics within these two elastoplastic regimes.

Specifically, a larger D suggests a more intricate surface microstructure, which may lead to fewer effective contact points and a reduced contact load. As D lessens, the surface becomes smoother on the microscopic scale, resulting in more significant contact areas and subsequently increased contact loads for the given elastoplastic regimes.

3.5.2.3. Plastic deformation regime

Figure 3.8 highlights the relationship between the contact load P_{sp} (Equation 3.14) in the plastic regime and the fractal parameter D and the spot area a_s. In these figures, it is observed that the whole plastic deformation regime remains unaffected by the parameters D and G_{fs}.

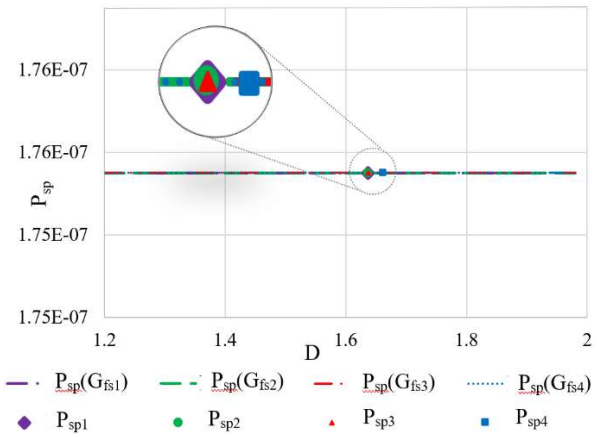

Fig. 3.8. (a) Variation contact load P_{sp} with fractal parameters D.

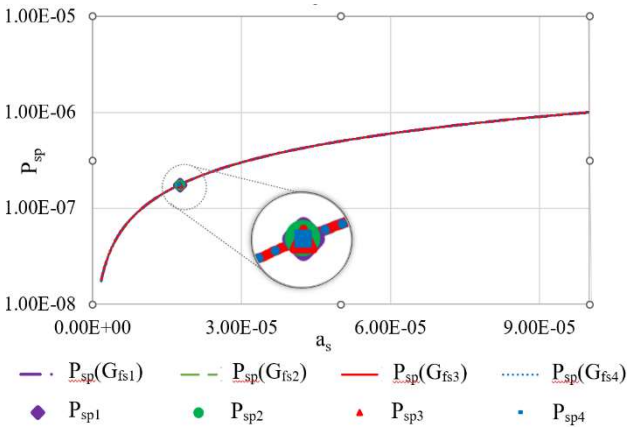

Fig. 3.8. (b) Variation contact load P_{sp} with spot area a_s

When a material reaches its fully plastic state, the initial surface characteristics and parameters such as D and G_{fs} become less relevant. At this stage, asperities undergo significant deformations, and subsequent interactions are more related to the plastic behaviour of the material than to its initial state or its fractal properties. As loading continues and the material deforms, asperities can merge, forming larger contact regions, and their influence becomes less pronounced. In this regime, material properties become paramount, and the significance of parameters D and G_{fs} diminishes a lot, losing their relevance in understanding contact behaviour.

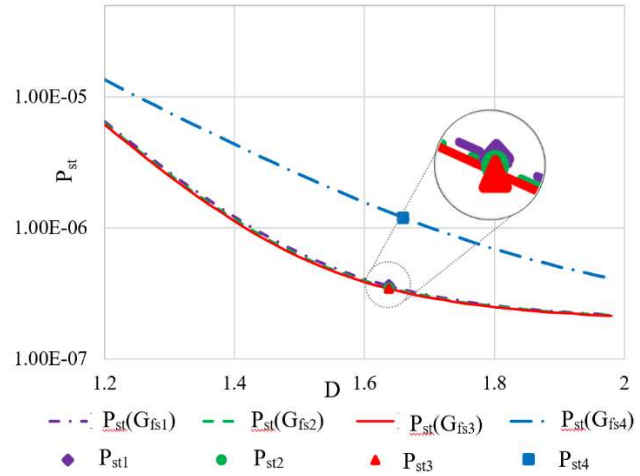

Fig. 3.9. (a) Variation contact load P_{st} with variable D and G_{fs} fractal parameters.

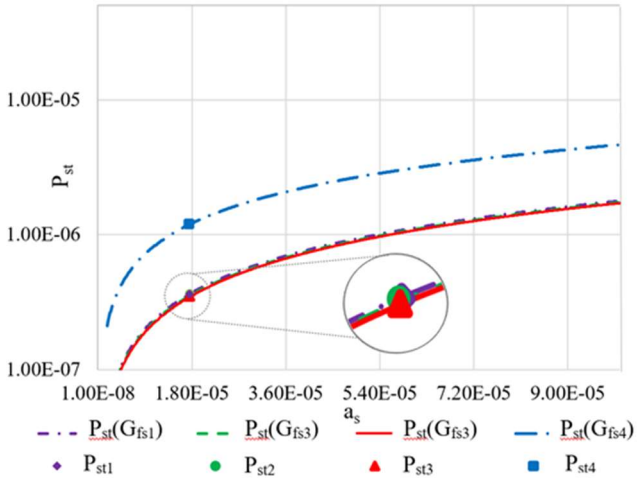

Fig. 3.9. (b) Variation contact load P_{st} with variable as, a_s and G_{fs} fractal parameters.

Figure 3.9 (a, b) depicts the total contact load, P_{st}, (eq. 3.15) and its interplay with the fractal parameters D and G_{fs}. Mirroring the trends observed for P_{se}, P_{se1}, and P_{se2}, a_s, D and G_{fs} vary, P_{st} also demonstrates a similar response.

However, it's noteworthy that while these parameters influence the elastic and elastoplastic regimes, the full plastic regime remains unaffected by variations in D and G_{fs}.

3.5.3. Real contact area

The dimensionless real area (A_{rs}) was determined for all four deformation regimes analysed. As an example, figure 3.10 illustrates the variation of the real area (A_{rs}) concerning the fractal parameter D and the largest spot area a_{ls}, which can range from 0 to 1.

For instance, Figure 3.10, drawing on the formula detailed earlier, showcases the variability of the real contact area (Ars) in relation to the fractal parameter D and the largest spot area (a_{ls}), which ranges from 0 to 1. This relationship is quantified in Equation 3.19, which precedes the graphical representation.

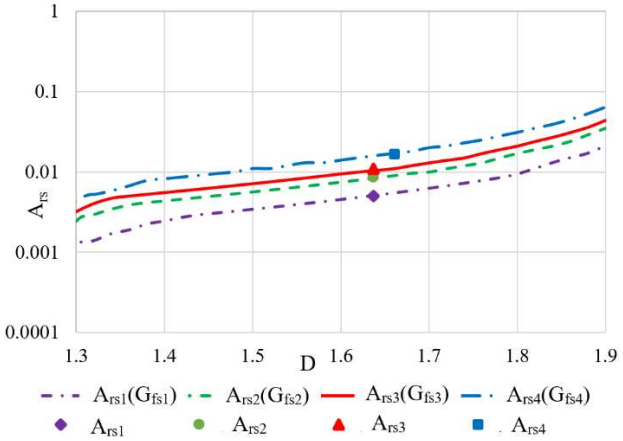

Fig. 3.10 (a) Variation real contact area A_{rs} with variable fractal parameter D, G_{fs} and maximum spot area a_{ls}

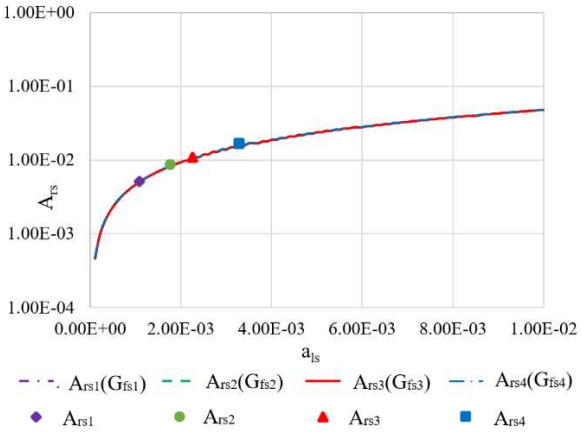

Fig. 3.10 (b) Variation real contact area A_{rs} with variable maximum spot area a_{ls}.

Figure 3.10 (a), corroborated with equation 3.19, shows the interplay between the real contact area (A_{rs}), the fractal parameter D, and the largest spot area a_{ls}.

The figure indicates that as the fractal parameter D increases, there is a corresponding increase in the real contact area. This suggests that the fractal dimension D is intrinsically linked to the expansion of the contact area. Moreover, in the context of Hertzian contact mechanics, this increase in contact area may affect stress distribution and deformation characteristics. Notably, variations in A_{rs} and the type of surface interaction could have implications for acoustic emissions or noise generation, as they relate to asperity contact, stress concentration, and the sliding and stick-slip phenomena. As D and a_{ls} change, alterations in contact mechanics may trigger different vibrational modes, which in turn could affect the nature and level of noise generated during the contact process.

Instead, from figure 3.10 (b), it is observed that G_{fs} does not influence the actual contact area. The increase in the real area with the size of the largest spot suggests that this growth might be dominated by the significant contributions of individual large asperities (a_{ls}). The lack of influence of the scale parameter G_{fs} on the real contact area also indicates that, despite the variation in asperity density (as G_{fs} changes), it does not affect the actual contact between surfaces.

3.5.4. Total normal load

Figure 3.11 shows the fluctuation of the dimensionless total normal load (F_{nst}) in relation to the fractal parameter D and the largest spot area a_{ls} which can span between 0 and 1. This correlation is quantified by Equation 3.24, which provides a mathematical foundation for understanding the observed trends.

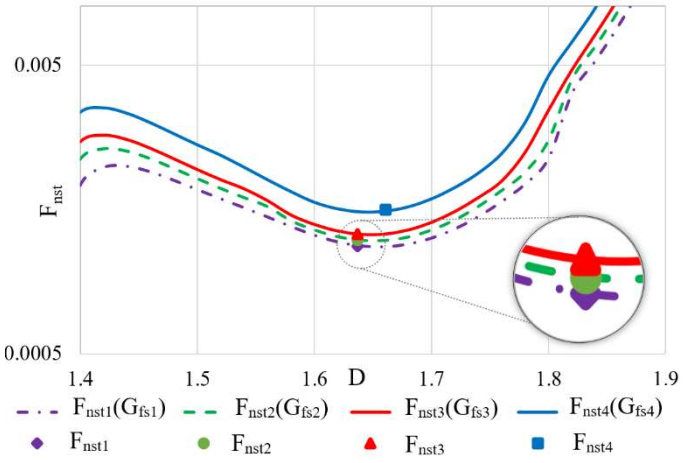

Fig. 3.11. Variation contact load F_{nst} with variable fractal parameter D and maximum spot area a_{ls}.

Figure 3.11. details the relationship between the total normal load, F_{nst}, and the parameters D, G_{fs} and a_{ls}. Thus, it is observed that the total force, F_{nst}, increases with the expansion of the area of the predominant spot. The effect of D on F_{nst} is evident only within the range D from 1.35 to 1.9. F_{nst} appears to be independent outside this range, suggesting that D is not the primary factor governing F_{nst}. This hints at the possibility that surface-level interactions or intrinsic material characteristics may take precedence in these regions, diminishing the role of D.

At higher values of D, there is an increased likelihood that asperities interact at both micro and macro levels, which could significantly contribute to the total contact force, especially when the area of the largest spot is reduced. However, at very low values of D, the

surface might be homogeneous or uniform enough that asperities do not significantly determine the total contact force, regardless of the size of the largest spot. Such behaviour suggests that other mechanisms or properties at the material level or surface interactions might dominate under these conditions.

3.5.5. Static friction coefficient

Figures 3.12 (a, b) depict the dependency of COF on F_{nst} (Eq. 3.26) and the fractal parameter D.

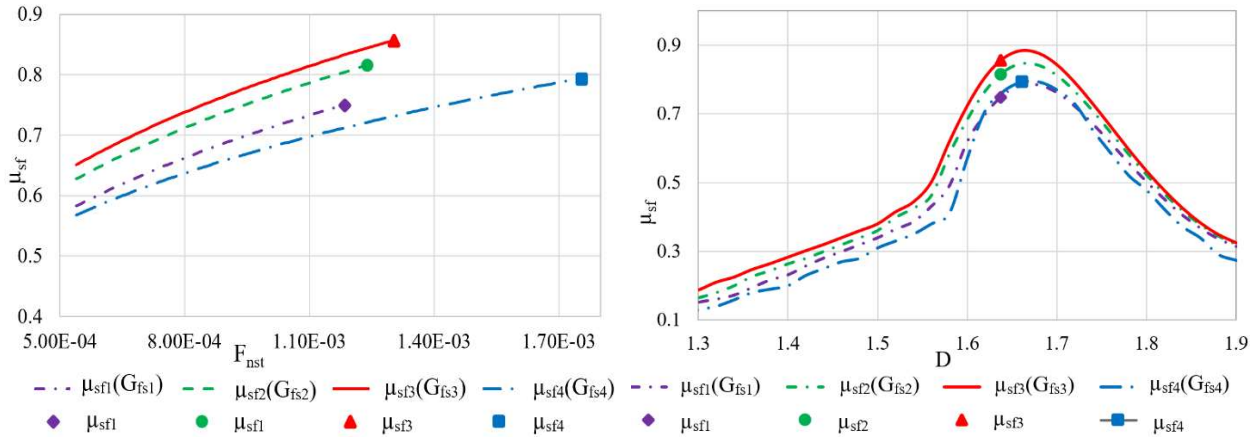

Fig 3.12. (a) Variation contact load F_{nst} with static friction coefficient (μ_{sf}).

Fig 3.12. (b) Variation static friction coefficient (μ_{sf}) with variable fractal parameter D.

In the graph 3.12 (a), for cylinder-plane pairs (μ_{sf1}, μ_{sf2}, *and* μ_{sf3}), the static coefficient of friction (COF) increases with the dimensionless total normal load. This trend aligns with expectations since a greater normal force enhances the interlocking of surface asperities, thereby increasing friction.

Conversely, for the wheel-rail pair (μ_{sf4}), a lower static COF is observed even under significantly higher F_{nst}. This phenomenon may be attributed to the presence of a lubricating film or lubricated conditions in the wheel-rail contact zone, which can reduce friction. Additionally, at very high normal forces, such as those in wheel-rail contact, asperities might be flattened or deformed more extensively, potentially leading to an apparently larger contact area but with less effective micro-level interlocking, resulting in a lower static COF. Nonetheless, the increasing trend suggests that even under these conditions, as the normal force continues to rise, the interactions between asperities and resistance to sliding begin to have a greater impact, leading to a gradual increase in the COF.

From the example shown in Figure 3.12 (b), it is observable that at low G_{fs} values, the static coefficient of friction (COF) reaches its maximum and declines with an increase in Gfs,

highlighting the significant influence of the scale factor on friction characteristics. Conversely, the static COF can be detected by D only within the range of 1.3-1.9. Outside this range, the absence of a discernible static COF could be due to specific surface interactions, deformation characteristics, or insufficient roughness engagement to produce measurable friction.

The COF is at its maximum for D in the range of 1.6-1.7 because this fractal dimension range corresponds to the most optimal balance between surface adherence and the elastic deformation capacity of the asperities. At these values, the asperities are sufficiently engaged to create resistance to sliding but are not so deformed that they allow easier sliding. Essentially, a D of approximately 1.6-1.7 may reflect a density and distribution of asperities that maximize the interaction and interlock between the contacting surfaces, thus leading to an increased COF.

For the wheel-rail pair, the COF value is the lowest shown in the graph, which can be explained by several factors specific to railway systems. Firstly, the wheel-rail interface is often subject to lubrication conditions, either from natural environmental lubrication or the deliberate application of lubricants to reduce wear and facilitate smooth motion.

Secondly, at the level of extremely high forces encountered in wheel-rail contact, asperities may be flattened or plastically deformed, leading to a larger effective contact area but with a minor micro-level asperity engagement, resulting in a lower static COF. Additionally, the wheels and rails in railway systems are subject to wear and smoothing processes during use, which can smooth out the asperities and contribute to a reduced COF.

Moreover, due to the cyclic and repetitive nature of wheels passing over the same rail sections, a 'smooth' running path can form, further reducing the coefficient of friction compared to the laboratory-simulated conditions for cylinder-plane contact.

3.6. Conclusion

Fractal modelling techniques were employed to theoretically evaluate the static friction coefficient within the context of Hertzian wheel-rail contact mechanics, accounting for surface roughness.

The fractal parameters D and G_{fs} directly impact the elastic regime, influencing the critical contact area (a_{cs}), critical deformation (δ_{cs}), and the elastic contact force P_{se}.

The transition from the elastic to the elastoplastic regime (first and second) is aptly captured by the fractal parameters D and G_{fs}, which affect the surface roughness and asperity interactions, impacting the contact loads P_{sep1} and P_{sep2} and exerting a direct influence on the critical areas ($a_{cs1,}$ a_{cs2}), critical deformations ($\delta_{cs1,}$ δ_{cs2}).

When a material achieves its fully plastic state, asperities undergo substantial deformation, diminishing the relevance of initial surface characteristics and fractal parameters like D and G_{fs}. The initial surface roughness and fractal characteristics become secondary as material properties dominate, causing fractal parameters like D and G_{fs} to lose their significance in describing contact behaviour.

In the context of total contact load, P_{st}, variations in fractal parameters D and G_{fs} significantly influence the elastic and elastoplastic regimes but have no discernible impact on the full plastic regime.

In Hertzian wheel-rail contact, the fractal parameter D influences the real contact area (A_{rs}) and the largest spot size (a_{ls}), indirectly affecting acoustic emissions and noise generation.

Despite variations in asperity density with G_{fs} changes, the size of the largest asperities predominantly influences the real contact area, and G_{fs} shows no direct impact on the real contact area.

The total normal load, F_{nst}, interacts with the fractal parameter D, especially in the range 1.4-1.8. With the maximum spot area reduction, parameter D extends its applicability to its maximum capacity. The surface characteristics largely corroborate the behaviour of Fnst, the fractal dimensions, and the forces applied and emphasise the complex balance of these determinants in the governance of contact mechanics.

The static COF is intricately influenced by factors such as maximum spot area a_{ls}, the scale factor G_{fs}, applied force, and the fractal parameter D. Their interplay dictates the frictional behaviour, underscoring the importance of understanding these parameters when evaluating surface interactions. For variation D and G_{fs}, the static COF is evident between 1.4 and 1.9, but outside this range, it may be overshadowed by specific surface interactions, deformation trends, or inadequate asperity contact.

Chapter 4

Stick-Slip Phenomena and Acoustic Emission in the Hertzian Linear Contact

4.1. Introduction

The stick–slip phenomenon is characterised as a jerky motion at low and very low driving speeds in a frictional couple. During sliding, this phenomenon occurs if two types of conditions are met—necessary and sufficient. The necessary conditions are given by a decrease in the friction kinetic coefficient with an increase in the driving speed and the dependence of the friction static coefficient on the sticking time. At the same time, the value of the static friction coefficient between two contact surfaces must be greater than the value of the kinetic friction coefficient. A quantitative relationship provides sufficient conditions among the driving speed (order of magnitude from microns/s to mm/s), the moving body mass, and the finite stiffness system in the sliding direction (*S. S. Antoniou et al., 1976, L. C. Bo, 1982, S. Kato, 1972*).

The theory established by Hertz for the normal non-conforming contact with friction between two bodies with elliptical profiles represents a landmark in linear elasticity (*B. Storåkers, 2005*). Although the theory of Hertz refers only to elastic contact under normal force or normal force with adhesion, the knowledge of the pressure distribution, the deformations at the connection between two bodies, and the mechanical properties of the materials allow for an extension to a compound analysis with tangential and friction forces generated by sliding or rolling (*M. Ciavarella, 2015*). Contact friction between solid bodies under sliding conditions gives rise to various waveforms and oscillations within the contact, resulting in sound radiation, including acoustic emission (*A. Akay, 2002*).

Acoustic emission refers to transitory mechanical waves in the high-frequency range that are produced by elastic stress energy released in a solid material under mechanical stress. The propagation of elastic waves and oscillations due to the appearance of microcracks, deformations, and fibre breakage in solid bodies are manifested by acoustic emission (*R. E. Jr. Green, 1980*) and can be detected by AE-devoted transducers placed on or near the monitored interface (*S. A. Dobrynin, 2010*).

Initially, in the tribology field, AE has been proposed to monitor the operating condition of bearings (*F. Elasha, 2017*), cutting tools (*A. V. Filippov, 2017*), surface finishing processes (*D. Strombergsson, 2017*), sanding (*A. Boaron, 2018*), and rotary machines (*H. Sadegh, 2016*). The AE could assess the behaviour of machining tools during operation (*H. A. Kishawy, 2018, J. Badger, 2018*) The AE measurement method is appropriate for discovering initial structural changes in materials. For example, for complex systems, such as the piston–ring–cylinder system of diesel engines, the sources of acoustic emissions are signalled when the engine speed,

load, and lubrication conditions change (*R. M. Douglas, 2006*). The active monitoring and diagnosis of various machine components, such as bearings, gears, pumps, and motors, are assessed by AE evaluation over time (*K. Asamene, 2012, P. Tian, Y. Tian, 2015*). In addition, the generation of AE at different pressures and sliding speeds has been evaluated by basic methods for rough/finish turning (*A. E. Diniz, 1992, T. S. Reddy, 2010*), detection of the breakdown of a machine tool device (*E. Emel, 1988, E. N. Diei, 1987*), or in the case of disc brake friction couple components (*N. A. Stoica, 2017*).

Regarding the acoustic emission related to the stick–slip phenomena, experimental research has shown the occurrence of AE during the sliding and rubbing of flat surfaces of various materials, such as rock (*T. Matcharashvili, 2011*), granite (*B. D. Thompson, 2005*), and composite materials (*J. Začal, 2017*). Studies on the stick–slip phenomenon in O-ring sealing samples (*L. Chuanjun, 2012*) and the contact between a mild steel sample and hardened steel clamps (*C. Ferrer, 2010*) have shown the importance of AE utility in tribology.

The origin of acoustic emission is the internal modifications in the materials due to an external stimulus. These modifications are usually composed of discrete events so that the emission of elastic waves is in the form of bursts or pulses of distinctive characteristics. Therefore, the analysis of signals captured in the AE test is usually performed considering this discrete nature, using a rather complex range of parameters related to the wave pulses, such as the number of counts, the rise and disappearance time, or frequency content-related variables (*E. Martinez, 2013, A. Hase, 2013, J. Meriaux, 2010, T. Shiotani, 2008, E. M. González, 2013*). This analytical strategy, combined with the frequency content, typically in the ultrasound range (>20 kHz), leads to the need for specific equipment, both hardware and software, to carry out these very specific tests. However, some less demanding parameters, such as the power of the square signal integrated over the signal period (AE_{rms}), have been successfully used to quantify pseudo-continuous emissions (*J. Sun, 2005, H. S. Benabdallah, 2008*), even in wear and friction phenomena (*R. J. Boness, 1995, L. Zuo, 2018, J. Hanchi, 1991*).

The present work aimed to use parameters of the AE signal with low hardware and software demand, i.e., those that can be calculated from a signal captured by a multipurpose data acquisition system for mechanical tests, to detect the occurrence of the stick–slip phenomenon at the Hertzian linear contact in dry friction conditions.

In addition, the analysis of the correlation between the stick–slip amplitude and the amplitude of the acoustic emission provides a new quantitative identification of tribological states in different conditions of contact pressures and very low driving speeds. The energy

generated by AE and the energy consumed by friction for stick and slip phases were determined and analysed based on the Pearson correlation coefficient, while the correlation of these energies as a function of the driving and sliding speeds were obtained from the logarithmic fitting. With this, the AE accompanies the friction process and becomes, for Hertzian linear contact, a non-destructive tool for detecting and monitoring the stick–slip phenomenon.

At very low-speed regimes, it has been established that the characteristics of unlubricated friction between the cylinder and plane are largely independent of the material properties, a concept supported by studies from C. Caroli and P. Noziers (1995) and E. Rabinowicz (1958). This sets the stage for a deeper investigation into the nuances of friction, particularly under conditions where lubrication does not play a significant role.

The study broadens its research scope by incorporating the validation of the experimentally determined static friction coefficient by comparing it with the value obtained from fractal analysis, both measurements being conducted under stabilized regime conditions. This approach aims to reinforce understanding of the friction phenomenon and verify the accuracy of the methods used in calculating the static friction coefficient. By directly linking these research aspects, the aim is to detect the stick-slip phenomenon through acoustic emission parameters and to conduct a deeper analysis of the relationship between friction behaviour and low driving speeds, a central point in the study of tribology principles.

4.2. Experimental Model—Geometry and Material of Specimens

The material of flat and cylinder specimens is used for the rails and wheels in railway systems, as described in Chapter 3.3. The sizes of the cylinder and flat samples are shown in Fig.4.1.

The fixing drawbar of the cylindrical specimen was incorporated into the tribometer loading device. Applying a known tangential force on its free end caused the bending of the drawbar–cylinder system, which could be measured, and thus, the sample stiffness was obtained (straight slope—30.427 N/mm). This stiffness influences the amplitude of the stick–slip phenomenon; hence, the greater the stiffness, the more the stick–slip phenomenon will decrease until it disappears. Although the effect of the frictional force on deformation is essential, frictional force does not depend on stiffness.

The cylindrical sample moved vertically until it arrived at the flat specimen under predetermined conditions. In this position, it was loaded at a normal force (F_n = 20, 40, 60 N). The flat test piece moved linearly on a horizontal plane with a driving speed, thus achieving the

frictional force. This device simulated linear contact with tangential and normal forces at very low sliding speeds, specific to contact with forced rolling. The device allowed for the experimental detection of one of the effects of rolling motion micro slips, namely the dynamics of sliding friction at low speeds and contact pressures with elliptical Hertz-type distribution. This distribution led to a flat surface of the elastically deformed bodies, whilst the friction force between the specimens depended on the evolution of the friction coefficients with the driving speed (v) and sliding speed (v_{slip}).

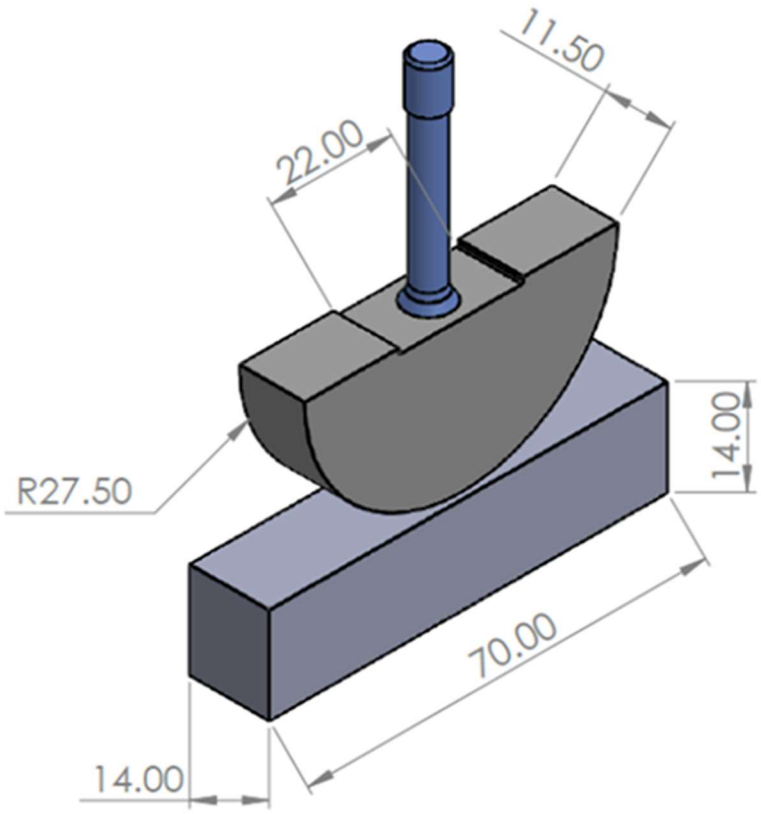

Fig.4.1. Dimensions for cylindrical and plane specimens used for tests.

The experimental setup presented in this paper was carried out in CERT UMT-2 Tribometer, which is used to test the stick–slip phenomenon of different materials. Fig.2 shows the test system with the upper and lower specimens connected to the tribometer. The tribometer was adapted to the specific slip conditions for Hertzian linear contact to perform these experimental tests. Thus, the clamping systems of the lower flat sample and the cylindrical sample with the bending stiffness calibrated to detect the SS phenomenon were designed and made for these experimental tests. The tribometer was equipped with a two-dimensional force sensor DFH-20 that was used to measure the control of a normal loading force and friction force between the upper and lower test pieces. The damping system, located between the force sensor

and the upper sample support, was used to maintain a constant load force during the tests. In order to maintain the normal force as constantly as possible at the contact of the samples, the tribometer was equipped with a device with a spring and shock absorber that allowed for the continuous adjustment of the normal force depending on the “response” of the material of the flat sample. The upper specimen was plugged into the monitoring system, while the lower specimen was connected to the L20HE linear motion unit.

The adhesion at the molecular level and the elastic–plastic deformations at the roughness level are both responsible for friction, which in turn is responsible for tangential force (*H. Eid, 2011, N. Mulakaluri, 2011, B. N. J. Persson, 2000)*. A CETR AE-5 AE sensor with a frequency range between 0.2 MHz and 5 MHz, integrated with the UMT-2 tribometer, was intended to measure the acoustic emission signals during the friction test. It was mounted on the side of the cylinder specimen. The AE signal, along with those related to force and position, was acquired by the CETR UMT control unit at a 200 kHz sampling rate. The AE signal was amplified with a gain of 60 dB, and its r_{rms} value was calculated every 0.5 s.

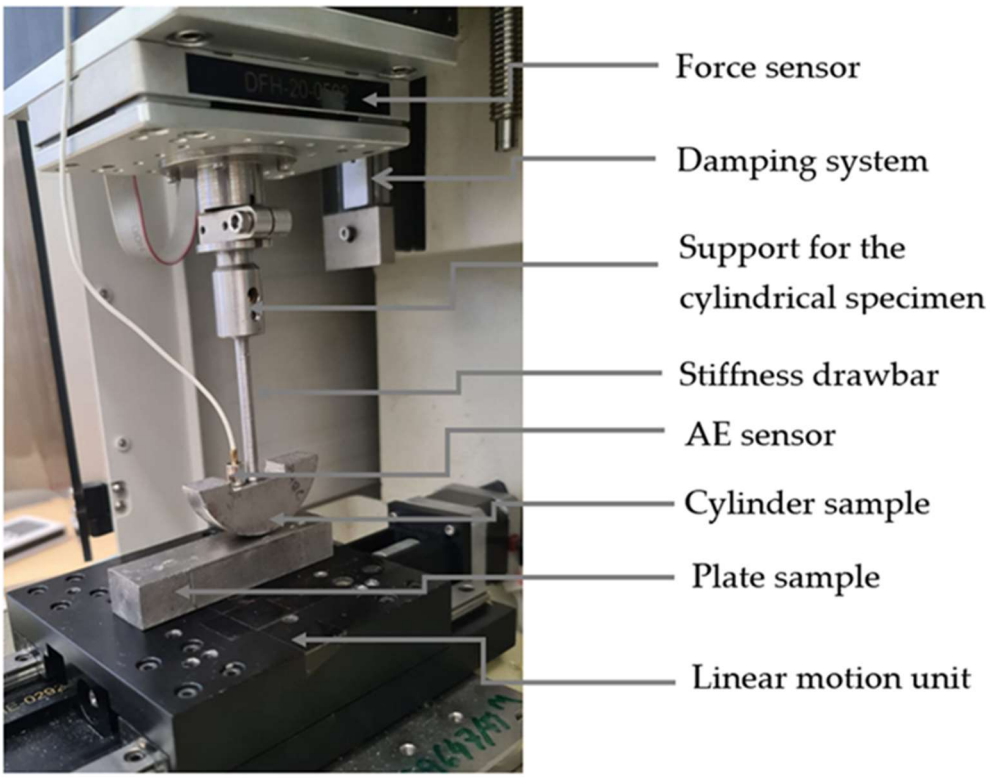

Fig.4.2. Tribometer to study the phenomenon of stick–slip.

The primary purpose of the experimental tests presented was to determine the evolution of the static and kinetic friction coefficients of the stick–slip phenomenon accompanied by the appearance of the acoustic emission at the Hertzian linear contact. The beginning of friction is a fundamental and essential issue in understanding the principle of tribology, an effect observed for different sliding speeds, three contact forces, and three contact pressures.

4.3. Methodology

One goal of this study was to demonstrate that the basic parameters of the AE are suitable and sufficient to detect the SS phenomenon and, thus, the adapted configuration of the Tribometer UMT-2 prepared for this type of experiment led to a simplified but sufficient analysis of the AE signals, avoiding the requirements of standard AE equipment. Moreover, the fundamental objective of the experimental tests carried out was to analyse the correlations of the AE and COF parameters, depending on the low and very low driving speeds, because the initiation of the relative motion between two bodies under friction is a fundamental and essential problem in understanding the friction principle in tribology.

The tribometer was equipped with tensometric transducers for normal and tangential stresses and AE and driving speed transducers. Due to the calibration of the bending stiffness on the vertical drawbar that was mounted on the cylindrical specimen (the bending deformation occurred depending on the force applied perpendicularly to the drawbar), the tangential force was determined as a frictional force. The driving speed was determined by adjusting the time and distance. The synchronization of the friction force measurement with the AE measurement was automatic. Based on the friction force, the normal force and AE were measured directly by the transducers and could be determined indirectly by calculating the average of each COF (static, kinetic, amplitude), sliding speed, energy consumed by friction, and several AE parameters (counts, amplitude, energy).

Before starting the tests, at the lowest normal load and driving speed, five assays were performed in order to "adapt" the surfaces to each other, and then the tests were run from the highest to the lowest driving speed with progressively increasing normal force. In order to analyse the phenomenon of stick–slip, 12 tests were performed. For these, four driving speeds (0.2, 0.1, 0.05, and 0.01 mm/s), four time periods (50, 100, 200, and 1000 s), and three normal load (20, 40, and 60 N) were set (*L. M. Babici, 2019*), resulting in three Hertzian contact pressures (48.20, 68.16, and 83.48 MPa), determined by calculation. Each test result was obtained from an average of three identical attempts performed under the same conditions (the

normal loads and driving speed supplied), and the coefficient of statistical variation was determined as the ratio between the mean square deviation and the arithmetic mean. The highest value of the statistical coefficient of variation for all tests (three forces and four speeds) was 0.08. The stick–slip periods used in the investigation were chosen from the stabilised zone of the movement, taken into account after two or three jumps from the initiation of the movement.

The stick and slip periods were analysed, and for each jump sequence between static and kinetic friction, the static friction coefficients μ_s, the kinetic friction coefficients μ_k, and the amplitude of the stick–slip phenomenon μ_v were determined, where $\mu_v = (\mu_s - \mu_k)/2$. The maximum static friction coefficient is the peak of the phenomenon, and the kinetic one is the minimum. These coefficients are approximately constant at the same load and speed (the COF is considered a deterministic phenomenon).

For each normal force and speed, the peaks of the static friction coefficients were counted (the static friction coefficient number is equal to the kinetic friction coefficient number), resulting in a frequency of stick–slip jumps relative to the period of time.

In this work, the count of AE refers to all AE peaks above the threshold value (set to 0.02 V). Only the signals that exceed the voltage threshold are identified as AE signals. Each AE count was obtained over time for each stick and slip phase sequence in a test, and finally, the average peak results were obtained for each test.

The AE amplitude, directly connected to the AE energy, denotes the highest measured voltage in a waveform. The energy induced in the system by friction (W_{COFst} and W_{COFsl}) during the stick–slip period is the integral defined by the friction force ($F_f = F_n$ COF) and the length of the friction path ($L_f = v \cdot t$). In the stick phase, there is no movement between the specimens, but the static friction force deforms elastically, and the system accumulates energy.

The energy generated by the acoustic emission (W_{AEst} and W_{AEsl}) during the stick–slip period is defined as the integral (area) of the square voltage (V_{AE}) emitted over time.

The instantaneous speed in the slip phase is defined as the derivative of the distance the cylindrical specimen covers during the slip time. This distance was determined by the lower test piece moving at a fixed translation speed (driving). The average slip speed was obtained from reporting the distance covered by the upper specimen in the slip phase (determined by the jump between the static friction force characteristic of the tip and the minimum kinetic friction force and the known system rigidity) during the slip phase. This time was determined from the recording of the phenomenon.

Error bars are graphical representations of data variability that are used on graphs to show the error or uncertainty in a given measurement; however, error bars frequently reflect one standard error, a standard deviation of uncertainty, or a certain confidence interval (e.g., a 95% interval). The Pearson correlation coefficient was used to determine the correlations between the COF and AE amplitudes, as well as the energies between them, whose values higher than 0.75 indicate a high correlation between these parameters. The results of the *p* test show the percentages of the confidence levels of the results obtained (*D. Nettleton, 2014, S. Boslaugh, 2008, W. Zhan, 2010*).

The analytical approach taken in this study delves into the slip oscillations observed in the stick-slip phenomenon, considering the kinetic friction coefficient as a function of driving speed and the static friction coefficient as a function of stick time. Referencing pivotal research such as that by F. Heslot (1994), T. Baumberger (1996), C. Caroli and P. Noziers (1995), and Baumberger et al. (1995), the studies highlight a clear logarithmic relationship between the static friction coefficient and the stick time (t_{stick}), of the form $\mu_s(t) = a_s + b_s \ln\left(\frac{t}{t_0}\right)$ where t_0 represents an arbitrary normalization constant. This indicates that μ_s is contingent on the interaction history and the prior conditions experienced by the surfaces, suggesting that the static friction coefficient is not just an instantaneous property but also a reflection of the material's "memory" or the cumulative history of contact and deformation.

The saturated static friction coefficient (μ_s) was determined at an extremely low speed of 10^{-4} mm/s to understand friction behaviour at very low speeds. In a saturated regime, contact characteristics such as the contact area and stress distribution remain relatively constant, not exhibiting significant fluctuations due to loading or unloading, and the system has reached a state of equilibrium where elastic, plastic, and dissipation effects are balanced, resulting in predictable and repeatable behaviour. This speed, considered to be very close to zero, lies in the transition zone between static and kinetic friction. In this specific transition region, slippage and material deformation may occur before the object moves continuously, representing an incipient slip. To determine the static COF at this speed, data previously obtained at four different speeds (from 0.01 to 0.2 mm/s) and three loads were used. By analyzing the dependence of the static friction coefficient on the stick time and the static and kinetic friction coefficients as a function of the driving speed, logarithmic approximations were applied to the resulting data, which allowed the determination of the memory length (L_{mc}) (T. Baumberger, 1995) for the three applied contact forces and, consequently, the static coefficients at the

targeted speed of 10^{-4} mm/s. Stick time (t_{stick}), in the context of the stick-slip phenomenon, refers to the duration that two contact surfaces remain in the stick state before starting the slip phase. In this phase, the surfaces are in stable contact, without relative sliding, even though they are subjected to an external tangential force. Measurements were conducted to determine the stick time in the context of the stick-slip phenomenon based on the experimental values obtained. The stick time for each SS sequence was determined, capturing the specific duration in which the contact surfaces remained in the "stick" state before entering the "slip" phase.
Through the analysis of experimental data, an average of the stick times was calculated corresponding to each speed and type of loading. These calculated averages comprehensively assess adhesion durations, offering a more generalized and unified description of the phenomenon across different operating and loading conditions. Within the realm of tribology and contact mechanics, L_{mc} denotes the distance across which past surface interactions still affect present behaviour. It can be considered as the 'history' of the contact or the surface 'memory' regarding its past tribological events. Furthermore, the creep time was determined from the experimental data, which, related to the memory length, determined the critical speed. Creep time, in the context of the stick-slip phenomenon for Hertzian contact (cylinder-plane or wheel-rail contact), is the duration that two surfaces remain in stable contact (stick phase) before beginning to slide against each other (slip phase). During this period, the friction coefficient remains relatively constant, and the system seems to "remember" the initial state of contact and adhesion. In the context of the stick-slip phenomenon, the critical speed is the speed at which the transition from the stick phase to the slip phase occurs. It is calculated as the memory distance (memory length) ratio to the creep time and is a measure of how quickly a system transitions from the adhesion state to the sliding state. Various factors, including the applied force, the properties of the materials in contact, and lubrication or humidity conditions can influence the critical speed. In some cases, the critical speed can be an indicator of the stability of the system under varying loading and operating conditions. The experimentally obtained static friction coefficients in a stabilized regime at a speed of 10^{-4} mm/s were compared and validated with those determined by the fractal method, as detailed in Chapter 3.

4.4. Results and Discussions

The friction coefficient evolution accompanied by AE is presented as an example of the results obtained for the driving speed of 0.01 mm/s at normal forces of 20–60 N. (Fig.3a–c) and the friction coefficient evolution for the force of 60 N at the four driving speeds

(Fig.3d). In all cases, the presence of the stick–slip phenomenon was confirmed by COF variation. In general terms, the stick–slip jumps coincided with the sudden increases in AE, although for a 20 N load, this coincidence was not always present.

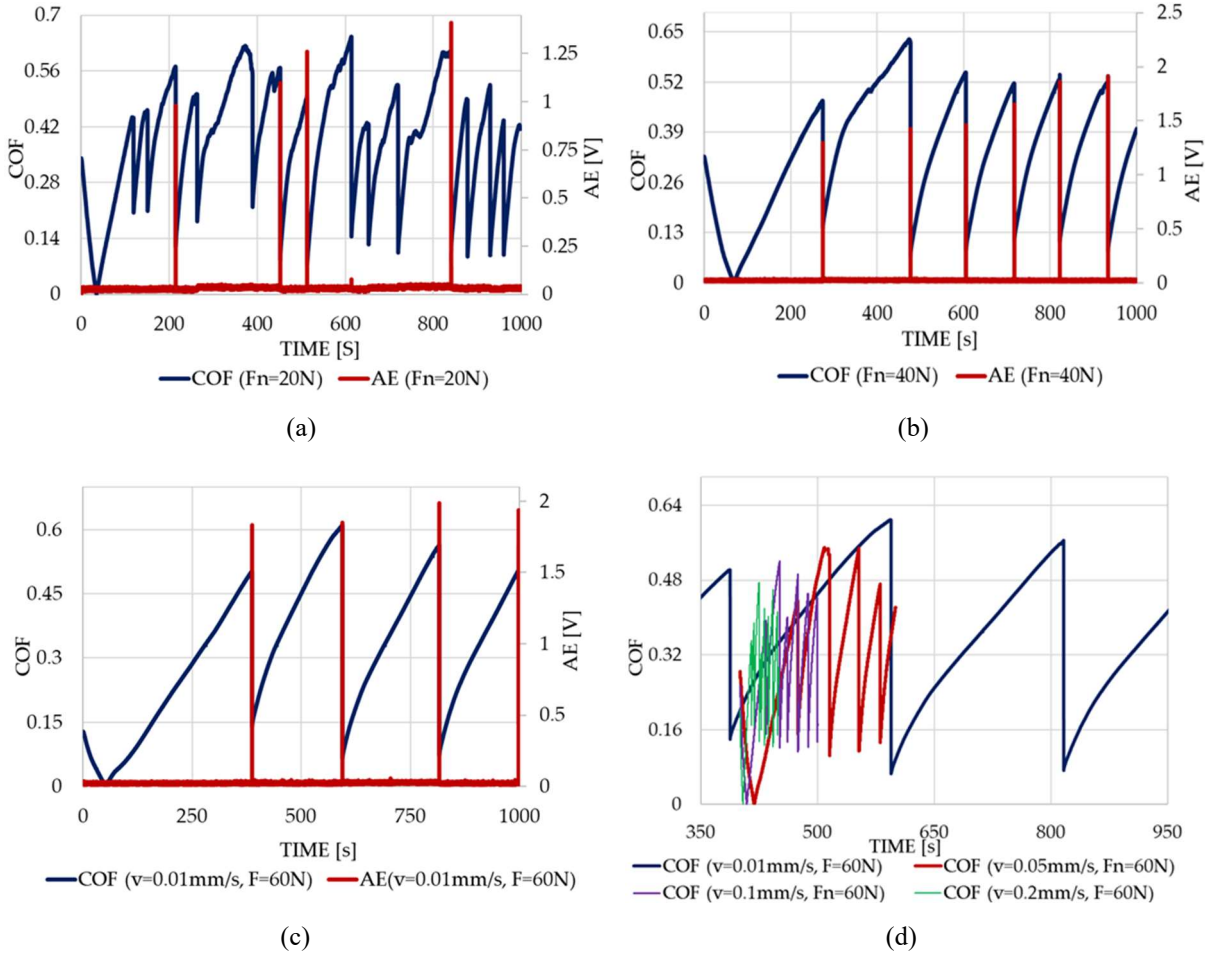

Fig.4.3. COF and AE amplitude with a driving speed of 0.01 mm/s
for the normal force of 20 N (a), 40 N (b), and 60 N (c).
Comparison of COF results over time at 60 N force and all driving speeds (d).

As a general trend, a high normal load and slow driving speed tended to create a stick–slip phenomenon of low frequency and high amplitude, as shown in Table 1, where each value represents an average of all stick–slip events at a specific normal force and driving speed (the same holds for all figures). The driving speed, sliding speed, and normal load are the major factors that play a significant role in the variation of friction coefficients (*J. F. Archard, 1980, B. Bhushan, 1999, M. A. Chowdhury, 2011*). The driving speed and normal load are directly measured from tests, and the sliding speed is easily calculated from the time and displacement of each phase. The sliding speed is related to the stick–slip frequency and amplitude; therefore,

a higher normal load and slower driving speed tended to increase the sliding speed due to the stick–slip phenomena of low frequency and high amplitude (Fig.4.4).

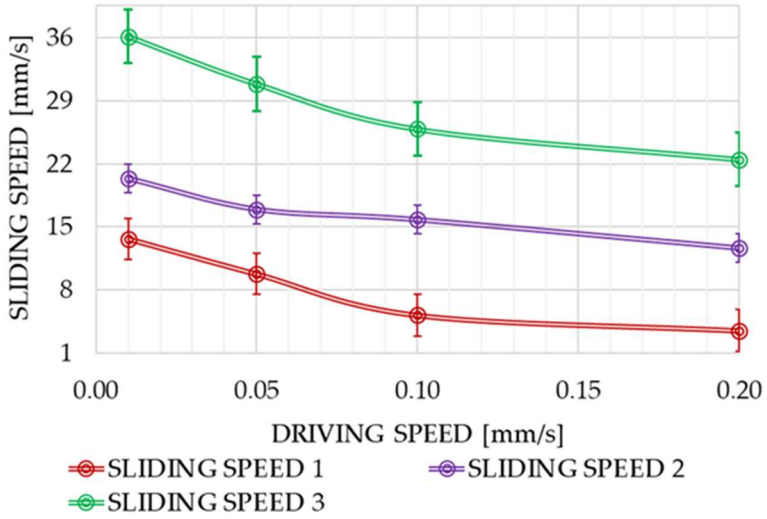

Fig.4.4 Variation in sliding speed with driving speeds (mm/s), including error bar.

Table 4.1. Values of the friction coefficients.

Driving Speed (mm/s)	F_n= 20 N			F_n = 40 N			F_n = 60 N		
	μ_{s1}*	μ_{k1}**	μ_{v1}***	μ_{s2}*	μ_{k2}**	μ_{v2}***	μ_{s3}*	μ_{k3}**	μ_{v3}***
0.2	0.317	0.224	0.047	0.386	0.182	0.102	0.415	0.162	0.127
0.1	0.378	0.239	0.07	0.418	0.186	0.116	0.435	0.168	0.134
0.05	0.430	0.246	0.092	0.47	0.189	0.141	0.485	0.175	0.155
0.01	0.525	0.282	0.121	0.557	0.262	0.148	0.582	0.250	0.166

* Static friction coefficients. ** Kinetic friction coefficients. *** Amplitude of the stick–slip phenomenon.

Fig.4.5 shows the static and kinetic friction coefficients and the stick–slip amplitude for different driving speeds. As expected, the static and kinetic friction coefficients decreased as the driving speed increased to a specific stiffness. Both friction coefficients increased with the soldering time due to the phenomenon of "saturation" of the real contact area, so the higher the driving speed, the shorter the soldering time and the lower the static and kinetic coefficients (*S. Ozaki, 2020, K. Lontin, 2021*). The increase in driving speed also reduced the contact surface

and accordingly, the friction coefficient tended to decrease, giving, as a result, a stick–slip movement of lower amplitude (measured by the difference between the static and kinetic COFs), as can be seen in Fig.4.5c, and higher frequency, as shown in Fig.4.5d.

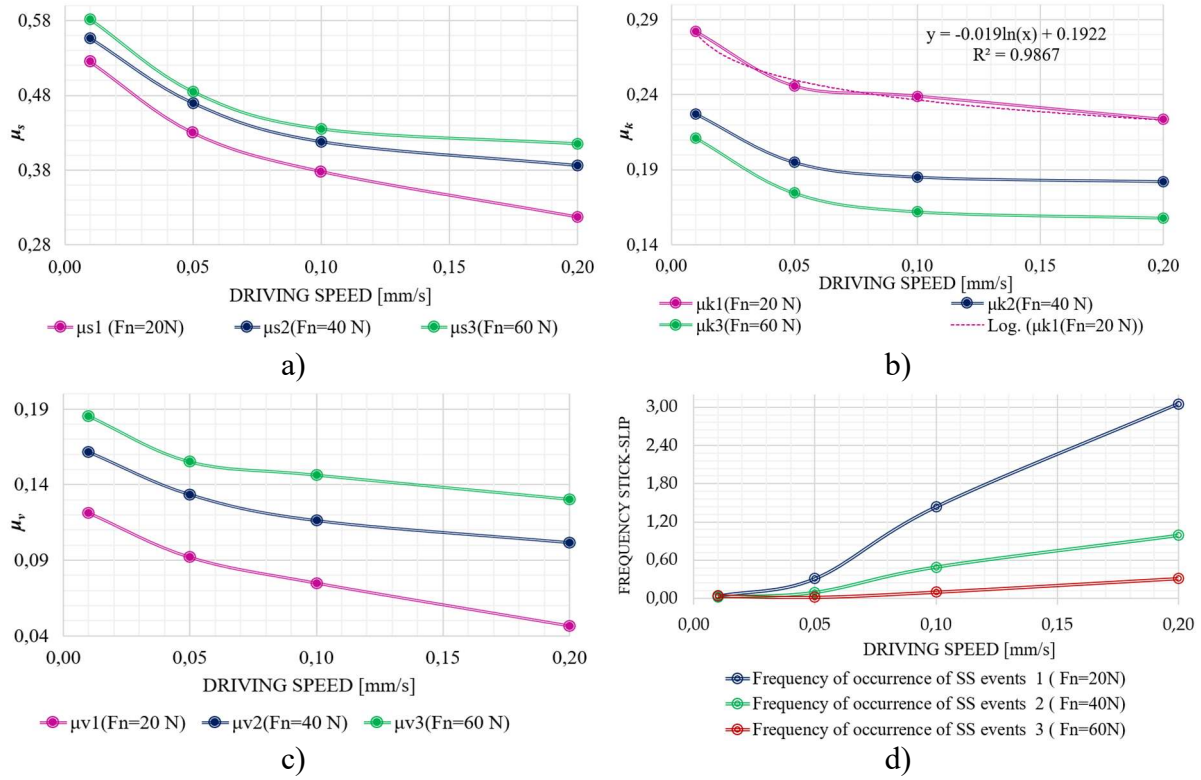

Fig.4.5. The influence of the driving speed and normal force on the friction coefficients:
a) static friction coefficient, b) kinetic friction coefficient, including the fitted curve of the kinetic friction coefficient with a force of 20 N, c) the amplitude of the stick–slip phenomenon,
d) with the frequency of the number of the stick–slip jumps.

Further increases in the driving speed would lead to the possible cancellation of the stick–slip phenomenon. The effect of the normal load is the increase in the static coefficient of the friction force because the contact pressure and real contact area also increase. In addition, according to the known molecular–mechanical (*D. Gourdon, 2003, D. Pavelescu, 1987*) friction theory for conventional dry contact, the kinetic friction coefficient decreases with a decreasing normal force. This divergence in the static and kinetic friction behaviour regarding the normal load leads to a stick–slip movement of a lower frequency and higher amplitude.

In addition, Fig.4.5b shows the dependence between the kinetic friction coefficients on the driving speed, which decreases with increases in the driving speed of the surface, approximated by the logarithmic curves of the form y = a + (b ln (x)) as has been previously found by Helstot and Caroli (*F. Heslot, 1994, C. Caroli, 1995)*.

The Pearson correlation coefficients were calculated between the amplitude of the SS (μ_v) as an independent variable and the normal force (F_n) and driving speed (v) as dependent variables. The obtained results can be found in Table 4.2.

Table 4.2. Correlation between SS amplitude and normal force, respectively, and driving speed.

Coefficients	μ_v/F_n v=0.2 mm/s	μ_v/F_n v=0.1 mm/s	μ_v/F_n v=0.05 mm/s	μ_v/F_n v=0.01 mm/s
Pearson correlation	0.969*	0.986**	0.976**	0.995**
Coefficients	μ_v/v F_n = 20 N	μ_v/v F_n = 40 N	μ_v/v F_n = 60 N	
Pearson correlation	−0.986**	−0.962*	−0.976**	

* Correlation is significant at the p =0.05 level (95% level of confidence).

**Correlation is significant at the p =0.01 level (98% level of confidence).

Regarding the acoustic emission, as a general trend, there was the continuous activity of low AE in the stick phase; however, there was a burst emission of high amplitude in the sliding phase, and both were dependent on the normal load.

It is easy to see that the AE peaks appeared only at the jumps from the stick to the slip (the transition from static friction to kinetic friction), although they took place with a delay of a few milliseconds compared to the COF. This delay of the AE could be explained by the finite propagation speed of the AE elastic waves compared to the moment of the initiation of the slip phase (Fig.6).

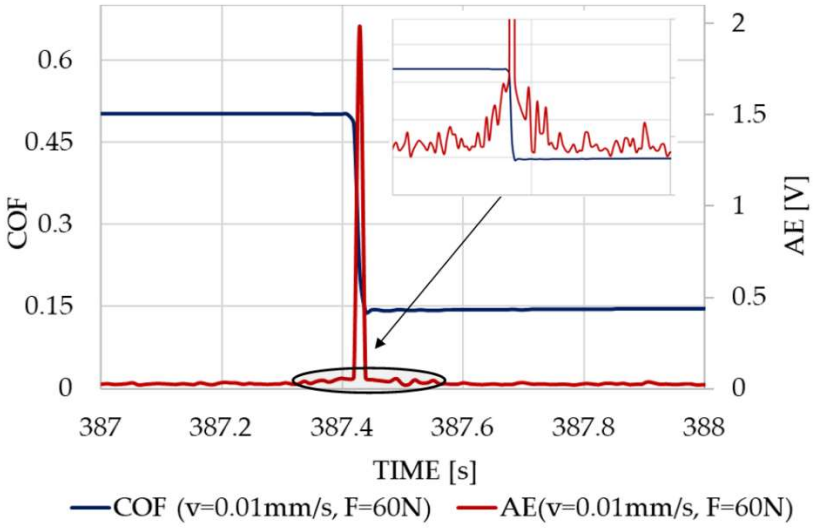

Fig.4.6. The variation in the friction coefficient and acoustic emission (peak extracted).

In the following, some characteristics of the AE, such as the AE amplitude, AE burst/continuous counts, and AE energy, are analysed in comparison to the characteristics of the stick–slip movement with the aim of investigating if they can be helpful for a comprehensive view of the identification of the stick–slip phenomenon by AE. The counts of AE in the stick and slip phases are presented in Fig.7.

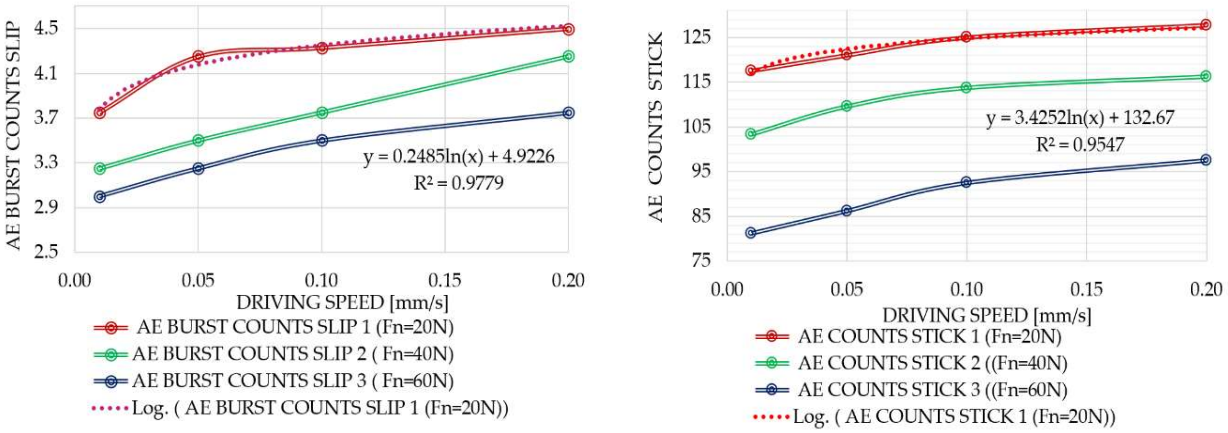

(a) (b)

Fig.4.7. AE counts in the slip (a) and stick (b) phases,
including the fitted curves of the counts of AE with a force of 20 N.

In both the stick and slip phases, the counts of AE increased with the driving speed and decreases in the normal load. In fact, the higher the frequency of the stick–slip movement, the higher the AE counts. The reason for this result is due to the higher number of stick–slip movements for a single test and because the AE takes place basically at the beginning of the slip movement, as shown in Fig.8. For each slip phase sequence in a test, each AE count was calculated over the slip time, and finally, mediated for each test. Likewise, for the stick phase, the AE counts were determined for each sequence over the stick time, and finally, an average was determined for each test. Therefore, a low frequency, higher amplitude slip-stick movement gives a relatively low count of AE with the burst aspect, mainly occurring at the beginning of the slip movement. However, the fact that some of the bursts are missing due to the low sampling frequency used in this work must be taken into account in consideration of the results related to the counts.

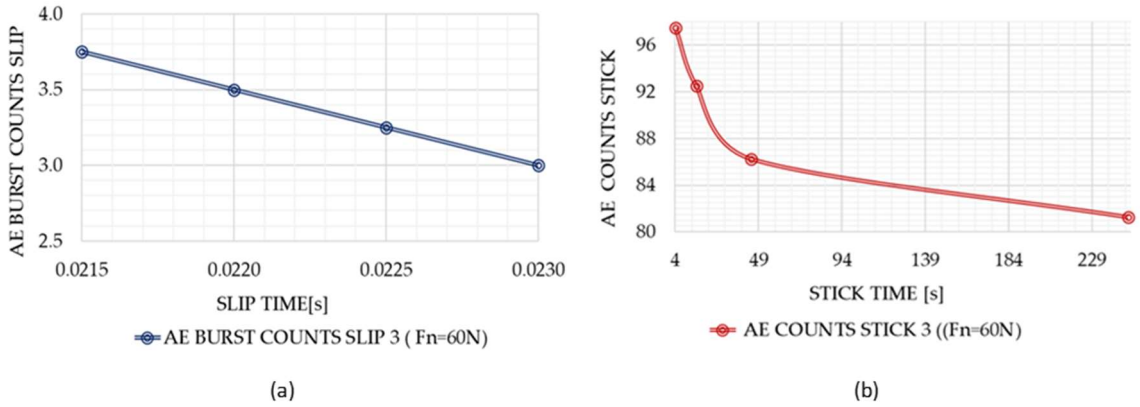

Fig.4.8. Distribution of the AE burst counts along the slip time (a), and AE counts along the stick time (b).

The amplitudes of the AE signal were plotted against driving speed for different loads (Fig.4.9). In general terms, the AE amplitudes for both the stick and slip phenomena seem to be rather related to the kind of stick–slip movement: the increase in the normal force and the decrease in driving speed led to an increase in the stick–slip movement amplitude, with a consequent rise in the amplitude of the AE bursts. In addition, the amplitude in the stick phase was significantly lower than the amplitude in the sliding phase (Fig.4.9a, b), as was expected, since the AE caused during the stick phase was only prompted by the contact surface deformation, while for the slip phase, other phenomena, such as a part of the plastic deformation occurred. In the process of transmitting normal forces between the two bodies and in the presence of relative motion, the "third body" was formed with properties specific to the material couple. Thus, the structure of the material changed, the existing microcracks joined, and new cracks appeared, especially during the appearance of plastic deformations (Fig.9). It was also observed that the AE amplitude follows a logarithmic curve, similar to the friction coefficients, depending on the movement speed.

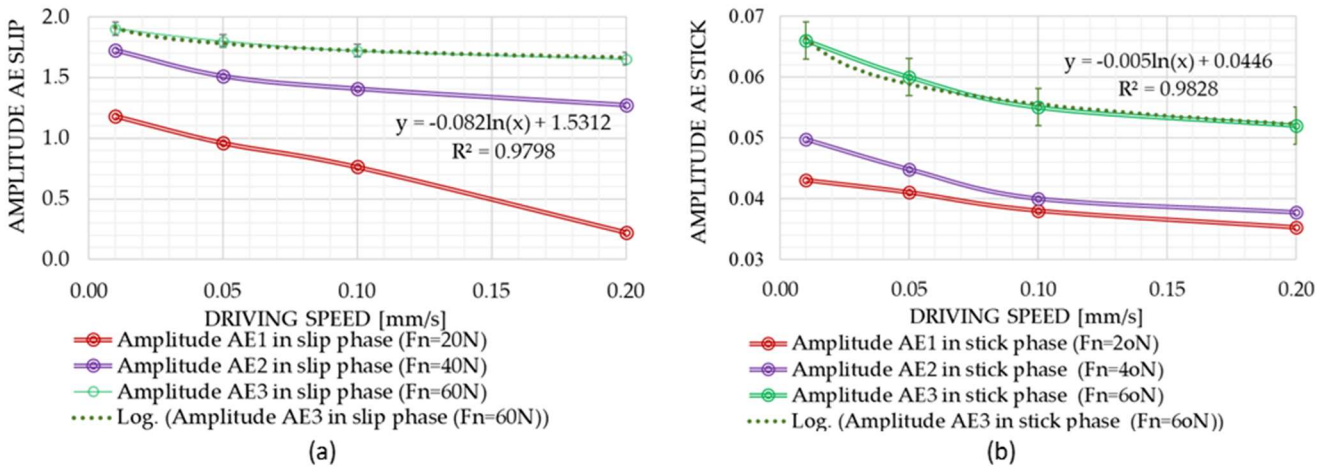

Fig.4.9. Variation in AE amplitude with driving speed in slip phase (a) and stick phase (b).

The Pearson correlation coefficients were calculated between the amplitude of the acoustic emission, A_{AEsl} and A_{AEst} from the slip and stick phases, respectively, as an independent variable and the amplitude of the stick–slip phenomenon (μ_v) as a dependent variable. The obtained results can be found in Table 3.

Table 4.3. Correlations between the AE and stick–slip amplitudes.

Coefficients	A_{AEsl}/μ_v	A_{AEst}/μ_v
	F_n=20 N	
Pearson correlation	0.980**	0.997**
	F_n=40 N	
Pearson correlation	0.930*	0.96*
	F_n=60 N	
Pearson correlation	0.961**	0.970**

* Correlation is significant at the p =0.05 level (95% level of confidence).

**Correlation is significant at the p =0.01 level (98% level of confidence).

The Pearson coefficients fall within the 95% confidence interval ($p< 0.05$), and it can be seen that there was a very high correlation between the AE amplitude and the amplitude of the stick–slip phenomena. Considering the high value of the correlation coefficients, we can conclude that the appearance of the stick–slip phenomenon can be identified by determining the amplitude of the acoustic emission.

Knowing that the amplitude of AE is correlated to the amplitude of the stick–slip movement, and the number of counts seems to be rather independent of the amplitude of the movement, it seems that the energy consumed by friction (W_{COF}) and the AE (W_{AE}) energy could also be related. The energy consumed by friction (W_{COF}) and the AE (W_{AE}) energy were calculated for the three forces, 20, 40, and 60 N, and for each phase of soldering and sliding (Fig.4.10). In general terms, the higher the amplitude of the stick–slip movement, the higher the energy consumed by friction (W_{COF}) due to increases in the friction force and sliding distance, and the higher energy generated by AE, due to the intensity of the deformation mechanisms in the contact zone.

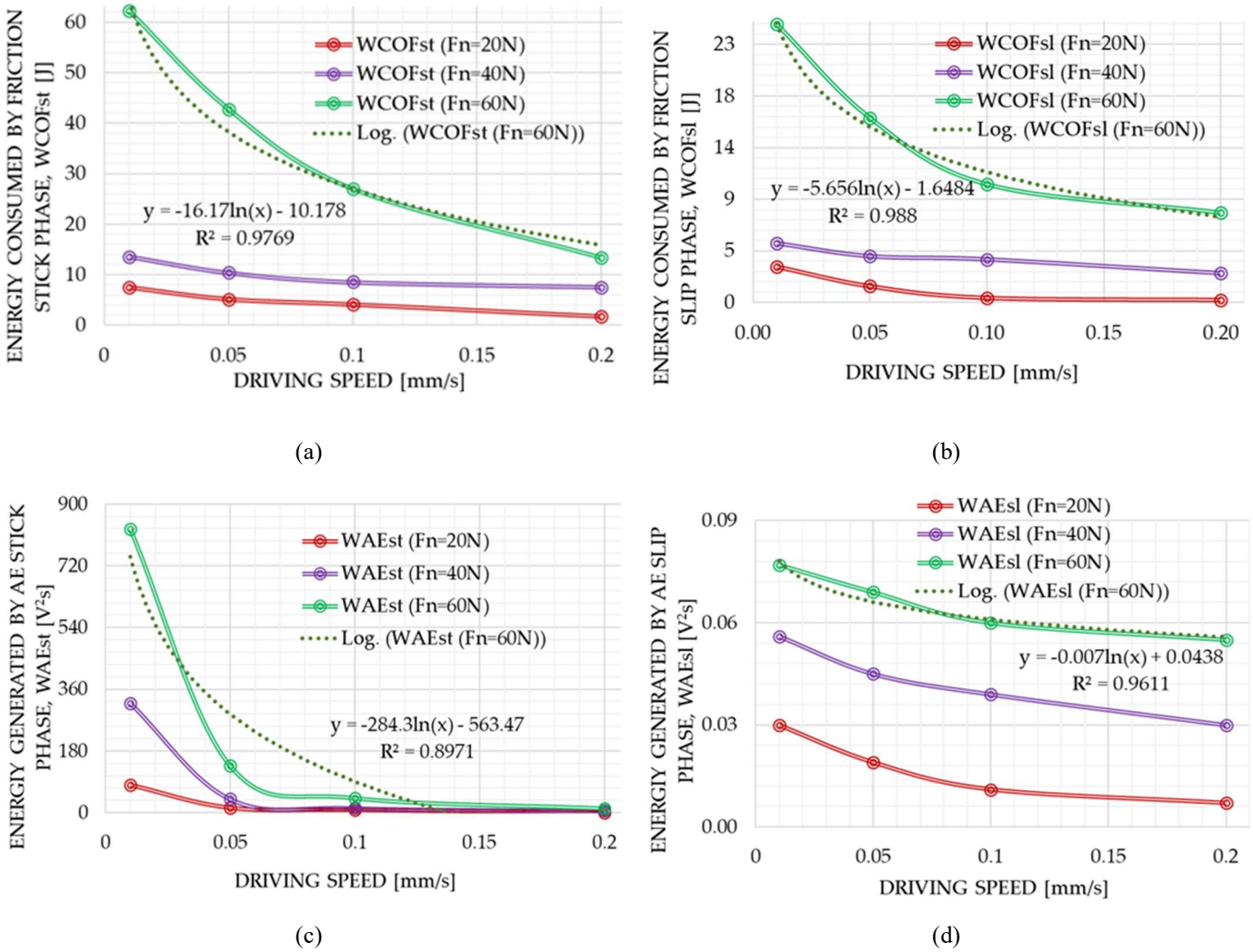

Fig.4.10. Variation in energies with different driving speeds (mm/s): (a) energy consumed by friction in slip phase, WCOFsl (J), (b) energy consumed by friction in stick phase, WCOFst(J), (c) energy generated by AE in slip phase, WAEsl (V2s), (d) energy generated by AE in stick phase, WAEst(V2s).

Therefore, the energies seem to be related to each other and also to the amplitude of the stick–slip movement. The Pearson correlation coefficients were calculated between the energy generated by the acoustic emission, W_{AEsl}(slip), W_{AEst} (stick) and the energy consumed by friction, W_{COFsl} (slip)W_{COFst} (stick), between the SS amplitude (μ_v) and these energies as well as between the AE_{sl} and SS amplitudes and the sliding speed (v_{slip}) (Table 4). Therefore, the energies appear to be related between themselves and also associated with the amplitude of the stick–slip motion. There was always a good correlation between both energies, with slightly reduced results in the stick phase when the 20 N force was applied. There was not always a burst of AE for the slide phase at this low normal force, so the correlation was not as good as

for a greater normal load. In addition, at low normal forces, the deformations at the contact level were small; therefore, reduced tangential force effects caused a reduced AE signal.

Table 4.4. Correlations between the AE and COF energies, stick–slip amplitudes and sliding speed in the stick and slip phases.

Coefficients	W_{AEsl}/W_{COFsl}	W_{AEst}/W_{COFst}	A_{AEsl}/v_{slip}	μ_v/v_{slip}	μ_v/W_{COFsl}	μ_v/W_{COFst}	μ_v/W_{AEsl}	μ_v/W_{AEst}
F_n=20N								
Pearson correlation	0.990**	0.900*	0.91*	0.960**	0.91*	0.964**	0.939**	0.770*
F_n=40N								
Pearson correlation	0.991**	0.934**	0.963**	0.937**	0.921*	0.91*	0.945**	0.72*
F_n=60N								
Pearson correlation	0.989**	0.932**	0.999**	0.970**	0.935*	0.966**	0.976**	0.755*

* Correlation is significant at the p =0.05 level (95% level of confidence).

** Correlation is significant at the p =0.01 level (98% level of confidence).

Considering the high value of the correlation coefficients, it seems that the magnitude of the stick–slip phenomenon can be estimated by calculating the energies generated by the acoustic emission, both in the stick phase and the slip phase. The Pearson correlations between the stick–slip amplitude and the COF and AE energies in the stick and slip phases show a close correlation between them (Table 4.4). The amplitude of stick–slip movement correlates well with the AE energy for the slip phase and not so well (as expected) with the AE energy for the stick phase, but the energy seems not to be as good an indicator of the stick–slip movement amplitude as it is the amplitude of AE. In the stick phase, it is possible that the local elastic deformations were the majority compared to the plastic ones, and as such, the AE energy was reduced. The system (drawbar and cylindrical specimen) was deformed exclusively elastically. The real contact area also contained roughnesses that deformed plastically. There was also a strong positive correlation between the AE and SS amplitudes with the sliding speed for all applied forces (Table 4.4).

In order to ascertain the origin of the AE, the W_{AE} and W_{COF} in the slip phase were plotted against the sliding speed in Fig.4.11. The sliding speed is a direct indicator of the amplitude of the stick–slip movement, and, as expected, the friction energy tended to increase with the sliding

speed, and it was dependent on the normal force. In addition, the AE energy tended to grow with the sliding speed as well, but it shows some dependence on the normal force, suggesting that other complex phenomena took place at the contact point zone, such as a reduction in tangential stresses and an increase in the contact area.

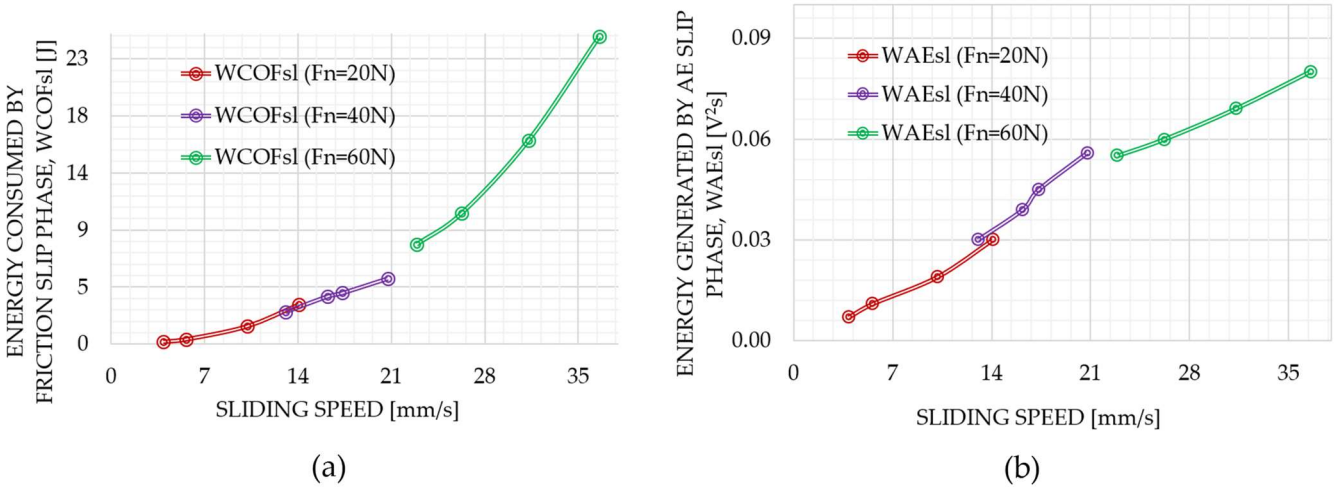

Fig.4.11. Variation in COF (a) and AE (b) energies with sliding speed.

At very low-speed regimes, the characteristics of unlubricated friction between the cylinder and plane are essentially independent of the material properties [C. Caroli, P. Noziers, 1995; E. Rabinowicz, 1958]. The analysis of slip oscillations in the stick-slip phenomenon considered the kinetic friction coefficient as a function of driving speed and the static friction coefficient as a function of stick time. The results of studies, including notable references such as *(F. Heslot, 1994; T. Baumberger, 1996; C. Caroli, and P. Noziers, 1995; and Baumberger et al., 1995)*, highlight a clear logarithmic relationship between the static friction coefficient and the stick time (t_{stick}) of the form $\mu_s(t) = a_s + b_s \ln\left(\frac{t}{t_0}\right)$ with t_0 being an arbitrary normalization constant; thus μ_s depends on the history of the interaction and the conditions to which the surfaces were previously subjected. This suggests that the static friction coefficient μs is not just an instantaneous property but is influenced by the "memory" of the material or the history of contact and deformation. The static dependence of COF on stick time (t_{stick}) can be seen in Fig. 4.12.

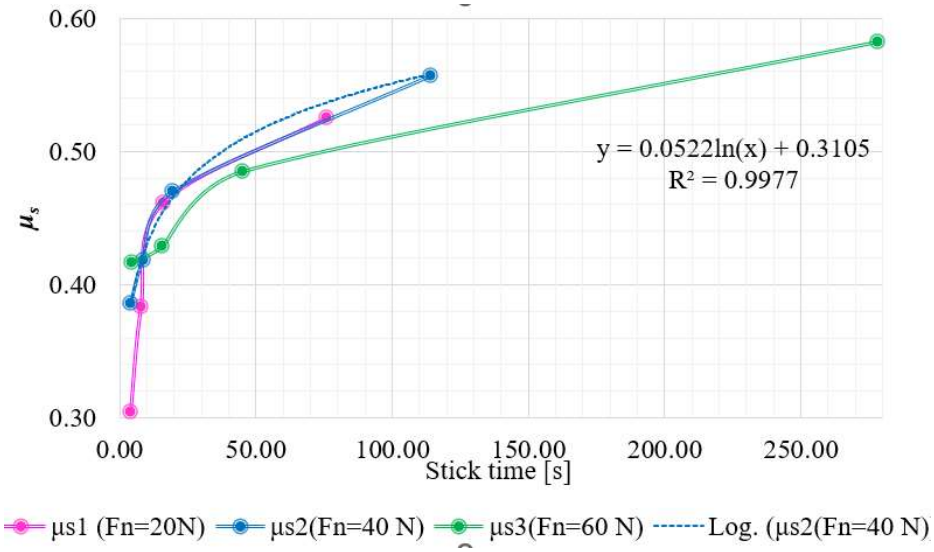

Fig.4.12. The stick time and normal force influence the static friction coefficients.

As observed in Fig. 4.12, μs gradually increases with the duration of the stationary contact before the initiation of movement. This response reflects a slow relaxation of the materials under a static load, with increased contact points and enhanced interaction between the microscopic asperities and roughness of the contacting surfaces. Thus, the stick-slip phenomenon, in the case of cylinder-plane contact, is profoundly influenced by the particularities of the microscopic-level interaction. Following Hertz's theory, the concentrated pressure in small contact areas favours elastic deformation and an increase in adhesion force and static friction coefficient. This is amplified by processes such as diffusion or adsorption at the surface level and possible chemical reactions, thus increasing the force required to initiate sliding. As previously shown (Fig. 4.5), the dynamic friction coefficient (μ_k), when measured in a regime of constant sliding, is dependent on the driving speed v. At low and very low speeds, it decreases logarithmically as v increases. At higher sliding speeds, μd increases, rapidly reaching a new dissipation regime. However, in the regime of reduced driving speed, μd is controlled by a mechanism similar to slow flow. This mechanism refers to how the friction between two surfaces changes to the speed at which they move against each other. Furthermore, [Rabinowics, 1965] established that frictional dynamics transition, as the driving speed increases, from a "slow flow" regime to one controlled by the overall inertia of sliding [A.L. Ruina, 1983; J.R. Rice, 1983]. In this context, a characteristic length Lmc can be defined, such that:

$$\mu_k\left(\frac{v}{v_0}\right) = a_k - b_k \ln\left(\frac{v}{v_0}\right) \;;\; \mu_k\left(\frac{v}{v_0}\right) = \mu_s\left(\frac{t}{t_0}\right) = \mu_s\left(\frac{L_{mc}}{v}\right). \tag{4.1}$$

Where, v_0 is an arbitrary normalising constant.

In studying friction and sliding behaviour in Hertzian contact, L_{mc} serves as an essential parameter, reflecting the "memory" or "age" of microscopic interactions. Moreover, L_{mc} is directly associated with the duration of time during which the contacting surfaces remain in a state of adhesion, known as "stick time," and can be interpreted as the average displacement necessary to renew or "reset" the population of micro-contacts, thereby marking a transition between sets of contacts at the microscopic level (J.H. Dieterich, 1994). Hertzian interactions involve complex behaviour at the microscopic level, where applied normal and tangential forces influence plastic flow and micro-contact strength. Thus, L_{mc} emerges as a crucial indicator, facilitating a deeper understanding and more accurate modelling of the dynamics of friction and sliding in Hertzian contact systems. The characteristic L_{mc} is relevant when analyzing the hysteresis phenomenon in stick-slip, as it highlights how previous interactions can influence current friction behaviour. When two surfaces come into contact and experience the stick-slip phenomenon, there is a continuous play of adhesion and sliding, and the hysteric response manifests as a memory of these interactions: even after the surfaces have slipped (slip phase), they retain a memory of the force or pressure at which slipping began. This memory is essential for understanding why and how slipping occurs at a specific force or pressure in subsequent interactions. Hence, memory length and hysteretic response are two interconnected concepts in the study of tribology and contact mechanics. Both highlight the importance of the history and previous experiences of the contacting surfaces in determining their current and future behaviour. Lmc has been used in calculations to represent the minimum sensitivity with which the system can detect and respond to variations in the dynamics of the friction process, by deducing the relationship between the static and kinetic coefficients as follows:

$$L_{mc} = v \cdot t_0 \exp\left(\frac{a_k - a_s - b_k \ln\left(\frac{v}{v_0}\right)}{b_s}\right) \tag{4.2}.$$

The coefficients a_s, b_s for μ_s and a_k, b_k for μ_k were extracted based on the logarithmic fitting curves obtained from the experimental data. These coefficients are tools for calculating

the memory length $L_{mc,}$ becoming essential in analyzing and characterizing the friction and sliding responses in Hertzian contact. (Table 4.5).

Table 4.5. Logarithmic fitting coefficients and memory length (L_{mc}).

	a_s	b_s	a_k	b_k	L_{mc}[mm]
F_n=20 N	0.2276	0.0699	0.1922	-0.019	0.261
F_n =40 N	0.3105	0.0522	0.1525	-0.016	0.821
F_n =60 N	0.3357	0.0420	0.2158	-0.019	1.075

The static friction coefficients obtained experimentally at a speed of 10^-4 mm/s were compared and validated with those determined by the fractal method, as detailed in Chapter 3, with the results found in Table 4.6.

Table 4.6. Comparison of static friction coefficients from experimental method against the fractal method.

Driving Speed (mm/s)	***F*$_n$= 20 N**			***F*$_n$ = 40 N**			***F*$_n$ = 60 N**		
	μ_{s1}*	μ_{sf1}**	Relative error [%]	μ_{s2}*	μ_{sf2}**	Relative error[%]	μ_{s3}*	μ_{sf3}*	Relative error [%]
0.0001	0.751	0.749	0.267	0.813	0.816	0.369	0.851	0.856	0.587

* Static friction coefficients. ** Static friction coefficients from fractals.

The data analysis presented in the table shows a notable concordance between the values of static friction coefficients obtained through experimental methods and those determined by fractal analysis. This alignment of results suggests that both methods are reliable for measuring the static friction coefficient under stable regime conditions close to zero velocity. The minimal relative differences between the data sets highlight minimal error, confirming the applicability and accuracy of both measurement procedures. In the context of tribology, this implies dependable predictability and consistency in the behaviour of static friction at very low speeds, which is crucial for understanding and modelling stick-slip phenomena in Hertzian contacts.

In the cylinder-plane contact under an applied force, the pressure distribution and the size of the contact area evolve until a stable equilibrium is reached. This adjustment period, known as "creep time," reflects the interval during which the cylinder's surface conforms to the contour of the flat surface. The duration of this process is determined by the properties of the materials, their stiffness, the rate of movement, and the applied load. Experimental results have

demonstrated that the creep time remains constant under varied loading and speed conditions, indicating predictability in the material behaviour at the initial contact stage without sliding. This observation is relevant in the analysis of Hertzian contact, where the creep time marks the duration necessary for stabilizing the contact between the cylinder and the plane, as can be seen, for example, for a force of 60 N and a driving speed of 0.01 mm/s in Fig. 4.14.

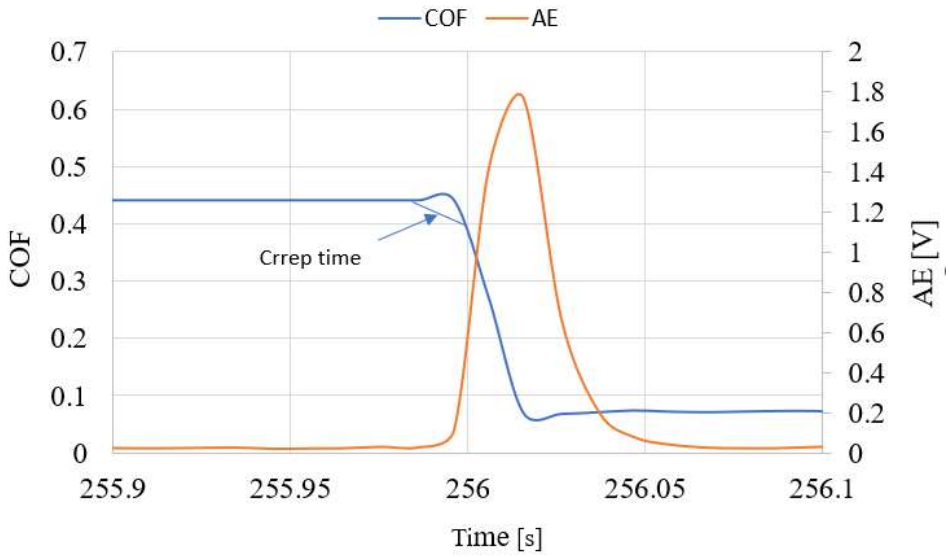

Fig. 4.14. Highlighting Creep Time

This consistent manner of the creep time can be analysed in relation to the critical speed, which serves as an indicator of the system's sensitivity to the transition from the stick phase to the slip phase, as can be observed in Table 4.7. A lower critical speed value may suggest a smoother and more gradual transition from stick to slip, while a higher value may indicate a more abrupt transition.

Table 4.7. Values of Creep Time and Critical Speed.

	Crrep time (s)	**Critical Speed (mm/s)**
Fn= 20 N	0.02	13.05
Fn = 40 N	0.02	41.05
Fn = 60 N	0.0205	50.14

Thus, from Table No. 4.7, a significant correlation can be observed between the applied force, the critical speed, and the stick time. As the applied force increases, the critical speed, an indicator of the threshold for transition from the "stick" to "slip" phase, also increases

proportionally. This suggests the system's increased reactivity and predisposition to initiate the "slip" phase under the influence of a larger tangential force. By maintaining an approximately constant creep time, evident variations in the critical speed are observed based on changes in the memory length, which other parameters, such as friction coefficients and the applied force, can influence. This allows for a detailed exploration of how various parameters influence the stick-slip dynamics and can contribute to a deeper understanding of the mechanisms governing these actions in Hertzian contact. A lower critical speed value, as observed for a normal load of 20 N, may indicate a smoother and more gradual transition from stick to slip, while a higher value, such as for a normal load of 60 N, may indicate a more sudden transition.

This set of observations highlights a direct connection and a dynamic balance between the critical speed and stick time concerning the applied force. Understanding this correlation is essential, facilitating a thorough analysis and coherent interpretation of the fundamental mechanisms governing stick-slip behaviour. This can form the basis for optimizing and adjusting operational and mechanical parameters in applications, allowing for more efficient management of the phenomenon and improving the performance and reliability of systems in Hertzian contact.

4.5. Conclusions

The acoustic emission signals generated during the relative motion between the cylinder–plane specimens were captured by a multipurpose acquisition system and processed using basic parameters based on the r_{rms} signal in order to determine if the stick–slip appearance and their sensitivity to the onset of movement can be detected and predicted by the acquisition and analysis of the AE using hardware and software with low demand. The tests were conducted under various situations involving normal loads, driving, and sliding velocities. Although the tests were not exhaustive, they verified the feasibility of using non-complex AE parameters as a non-destructive method of detecting the stick–slip phenomenon.

In all tests performed, the presence of the stick–slip phenomenon was confirmed by the COF variation and the coincidence with the bursts of AE for all contact pressures and driving and sliding speeds. The variables that significantly affected the changes in friction coefficients were the driving speed, sliding speed, and normal load. Higher normal loads and slower displacement speeds increased the slip velocity because of the low-frequency, high-amplitude stick–slip phenomena that occurred mostly at the start of the slide movement.

AE is related to this type of motion. In terms of acoustic emission, the stick phase had low AE activity, while the sliding phase exhibited bursts of high amplitude activity that were reliant on the normal load. Jumps from static to kinetic friction (COF) were followed at short time intervals (milliseconds) by acoustic emission (AE) jumps.

The presence of the stick–slip phenomenon can be detected by measuring the amplitude and energies of the acoustic emission revealed by a high positive Pearson correlation between them. The energy consumed by friction (W_{COF}) increased with the amplitude of the stick–slip motion, and the energy generated by AE increased also.

The amplitude and energies generated by the acoustic emission are relevant and confirm the direct dependence on the stick–slip phenomena for the non-lubricated Hertzian linear contact, while the count of AE bursts is not applicable to identifying the magnitude of the stick–slip movement, probably due to the same amount of real bursts missing caused by the relatively low sampling frequency used in this work.

Hence, the acoustic emission detected by analysing the parameters that can be used from a signal captured from a multifunctional platform becomes an essential indicator for detecting and monitoring the stick–slip phenomenon.

Experimental results show that an extended stick time increases the static friction coefficient, highlighting the impact of material memory and microscopic interactions on friction within the stick-slip phenomenon. The critical speed, determined by the creep time and memory length, plays a crucial role in identifying the transition from adhesion to sliding in Hertzian contact. This provides insights into how the history of contact and external factors influence friction in a tribological system. The agreement between the experimentally determined static friction coefficient and that obtained through fractal analysis confirms the accuracy of the latter method as a precise validation tool in the study of friction behavior. This correlation validates the use of fractal analysis as a reliable methodology for estimating the static friction coefficient under stable regime conditions.

Chapter 5

Conclusions and further work

In this chapter, the summary of the main findings of the thesis is presented. Moreover, various recommendations for future research on the topic are proposed.

5.1. Thesis conclusions

To begin with, techniques of fractal modelling were employed to depict the roughness characteristics of the rails at the Faurei Test Centre in Romania. Both the structure function and the Weierstrass-Mandelbrot function were used to capture the intricate nature of the rail roughness effectively. The analysis assessed 41 conventional statistical parameters and compared them with the rail acoustic roughness obtained from measurements and the simulated fractal parameters.

Four sections of rail roughness testing, each of 7.5 meters, were systematically evaluated and segmented from 1 m to 7.5 meters. A comparison was made between the statistical parameters of the experimental measurements and the parameters simulated using the W-M function, revealing that a representative number of these parameters fell within a relative error of 10%. However, it was observed that the fit of the number of simulated parameters to the measured parameters decreased as the measurement length decreased.

Specifically, when amplitude, spatial, and hybrid parameters were considered for a measured roughness of 7.5 m, their correspondence to the simulated roughness at the same length was found to be 100%. But as the measured length decreased, the matching of the number of parameters was noted to decrease gradually to 66.6% for a distance of 2.5 m and then to 50% for a length of 1 m.

For a measured roughness of 30 m, the roughness parameters from the experimental measurements were found to match the simulated parameters by 83.33% for the same length. As the measurement length increased, both the measured and simulated roughness profiles were observed to have almost symmetrical Gaussian distributions.

Parameters such as ADF, ACF, PSD, and BAC exhibited close roughness equivalence when simulated with the W-M function. The convergence of experimental measurements and simulated profiles underscored the effectiveness of the fractal approach in decrypting the complex behaviour of rail roughness.

Continuing, fractal modelling techniques were employed to assess the static friction coefficient within the context of Hertzian wheel-rail contact mechanics, with surface roughness taken into consideration. The fractal parameters D and G_{fs} were directly found to influence the elastic regime, affecting the critical contact area, the critical deformation, and the elastic contact force.

The transition between the elastic and elastoplastic regimes was characterized by the fractal parameters D and G_{fs}, which were found to influence the surface roughness and the

interactions between asperities. When the material reached its fully plastic state, substantial deformations in the asperities were observed, diminishing the importance of the initial surface characteristics and fractal parameters.

Regarding the total contact force, significant impacts on the elastic and elastoplastic regimes by variations in fractal parameters D and G_{fs} were identified, but no effect on the fully plastic regime was observed. In the context of Hertzian wheel-rail contact, the fractal parameter D was noted to influence the real contact area and the maximum spot size, indirectly affecting acoustic emissions and noise generation.

The total normal load was found to interact with the fractal parameter D, especially within the range of 1.4-1.8. The static friction coefficient was influenced by factors such as the maximum spot area, the scale factor G_{fs}, the applied force, and the fractal parameter D. Variations in D. G_{fs} were observed to influence the static friction coefficient between 1.4 and 1.9. Still, outside this range, it was noted that it might be overshadowed by specific surface interactions or insufficient asperity contact.

These observations underscore the importance of understanding and considering these parameters when surface interactions are assessed.

In the concluding phase of the research, the stick-slip phenomenon for Hertzian contact was closely examined.

Acoustic emission signals generated during the relative motion of cylinder–plane specimens were captured by a multipurpose acquisition system and were processed using basic parameters based on the RMS signal. The objective was to determine if the onset and sensitivity of the stick–slip phenomenon could be detected and predicted through the acquisition and analysis of AE using equipment and software with low requirements. Tests were conducted under various conditions, including normal loads and sliding speeds. Although the tests were not exhaustive, they confirmed the feasibility of using non-complex AE parameters as a non-destructive method for detecting the stick–slip phenomenon.

In all tests conducted, the presence of the stick–slip phenomenon was confirmed by the variation in the coefficient of friction and its coincidence with AE bursts. Significant influences on the coefficient of friction were found to be the driving speed, sliding speed, and normal load. Greater normal loads and slower driving speeds were found to increase the sliding velocity.

Regarding acoustic emissions, a reduced AE activity was observed during the stick phase, while high amplitude bursts of activity were presented during the sliding phase. The presence

of the stick–slip phenomenon was detected by measuring the amplitude and energies of the acoustic emission, which were evidenced by a strong positive correlation between them.

Amplitudes and energies generated by the acoustic emission were found to be significant and confirmed a direct dependence on the stick–slip phenomenon for non-lubricated Hertzian linear contact. Thus, the acoustic emission detected through parameter analysis was identified as an essential indicator for detecting and monitoring the stick–slip phenomenon.

From another perspective, the analysis of the experiments highlighted that a static friction coefficient (COF) was derived from the stick-slip phenomenon. This was perceived as a reflection of the specific behaviour of the material pair under certain conditions. Furthermore, a COF corresponding to the saturated regime was deduced using statistical methods. When compared with the COF obtained through fractal modelling, the coherence and relevance of using fractal theory in assessing and predicting the friction behaviour of materials in contact were demonstrated. The conclusion is that acoustic emission, coupled with fractal modelling, provides a robust and effective framework for studying and understanding the stick–slip phenomenon and its associated friction properties.

5.2. Contributions

- Analysis of the running surface quality of the railway track, focusing on the specific fractal dimensions of the roughness of the rails and the driving wheels, employing fractal geometry, and deducing the unique fractal parameters D and Gf, which are independent of the measurement scale;
- The utility of the Weierstrass-Mandelbrot function for simulating roughness height is argued by comparing it with 41 classical roughness measurement parameters, emphasizing the relevance of fractal dimensions of surfaces for Hertzian Contact;
- Establishing the minimum length for measuring rail roughness, ensuring that the results are conclusive and aligned with international standards on acoustic roughness (EN 15610: 2019), reflecting the fractal dimensions of roughness;
- The experimental determination of the static friction coefficient for Hertzian contact, followed by its validation through the application of a theoretical model employing fractal approaches.
- Detecting Acoustic Emissions (AE) as a crucial indicator and an effective non-destructive method for identifying and monitoring the stick-slip (SS) phenomenon in non-lubricated linear Hertzian contacts. Utilizing AE allows for direct and

instantaneous observation of transitions between stick and slip phases, thus providing deep insights into the dynamics of friction and surface interactions.

- Defining the memory length as a determining factor for the static friction coefficient in relation to stick time and determining the critical speed of transition between the stick and slip phases;

5.3. Recommendations and future work

Diagnosing rail degradation and the stick-slip phenomenon using AE transducers.

Diagnosing rail degradation and capturing the stick-slip phenomenon using AE transducers. Utilizing AE transducers allows for accurate detection and real-time monitoring of rail degradation and captures the intricacies of the stick-slip phenomenon. This deeper insight facilitates more efficient interventions and enhanced infrastructure maintenance management.

Linking various wear patterns of rails and wheels with changes in fractal dimensions.

By conducting a detailed examination and modelling using the fractal method of different wear patterns, we can gain a clearer insight into how these wear patterns influence fractal dimensions and, consequently, the dynamic behaviour of rails and wheels. Understanding this relationship can pave the way for devising more efficient strategies for preventing and repairing rail and wheel degradation.

Suggestions for implementing fractal dimensions in the standardized characterization of acoustic roughness.

Incorporating fractal dimensions as a standard in the analysis of acoustic roughness could provide a more coherent metric for assessing the performance of rails and wheels. This might also facilitate data communication and comparison across different studies and applications.

Highlighting the influence of fractal parameters of the equivalent roughness of rails and wheels on vertical rolling vibrations.

By assessing the stiffness of Hertzian surfaces with fractal roughness, we can gain crucial insights into how changes in fractal parameters impact vertical vibrations. This knowledge is essential, as the interplay of fractal roughness parameters, contact dynamics, load distribution, and material properties jointly influence these vibrations. Understanding these interactions could lead to developing solutions for vibration reduction and prolonging the lifespan of rails and wheels.

Establishing a method to evaluate unique fractal parameters using surface probing devices with varying resolutions.

This method could offer a more detailed and nuanced surface examination, accurately revealing roughness variations and structure. Additionally, it might enhance the accuracy and reliability of measurements and provide a framework for verifying acoustic roughness results. In the context of railway maintenance, this approach could be pivotal for drafting a strategic maintenance plan. With the ability to precisely anticipate roughness variations and fractal parameters, the optimal timing for rail rectification could be determined, ensuring efficient operation and prolonging the life span of the railway infrastructure.

Appendix A

Publications

Journals

Accepted manuscripts

- Babici L. M., Tudor A., J. Romeu, Stick-slip phenomena and acoustic emission in the Hertzian linear contact, Multidisciplinary Digital Publishing Institute, Applied sciences (Basel), 22/09/2022, 12, 19, article 9527, 1 - 16, 2076-3417
- Babici L. M., Tudor A., J. Romeu, M. Stoica, Fractal evaluation aspects in characterizing the roughness of a driving wheel from a locomotive, Institute of Physics (IOP), IOP Conference Series: Materials Science and Engineering, 01/01/2020, 724, 1, 1757-8981
- Babici L. M., Tudor A., J. Romeu, M. Stoica, Fractal rigidity of the wheel-rail contact, Institute of Physics (IOP), IOP conference series: materials science and engineering, 25/12/2020, 997, 012002:1 - 012002:12, 1757-899X
- Babici L. M., Tudor A., Some aspects regarding the roughness of the railway surface and rolling noise at locomotives, Institute of Physics (IOP), IOP conference series: materials science and engineering, 26/06/2019, 514, 012010:1 - 012010:14, 1757-899X
- Babici L. M., Experimental measurements of composite materials from the bearing structure of railway vehicles, Institute of Physics (IOP), IOP Conference Series: Materials Science and Engineering, 11/2016, 161, article 012064, 1757-8981

Manuscript under review

- Babici L. M., J. Romeu and Tudor A., Fractal - based modelling of rail roughness, Acoustical and Mechanical Engineering Laboratory (LEAM), Politècnica de Catalunya (UPC)

International Conferences

- Babici L. M., Tudor A., and J. Romeu, Fractal based modelling of rail roughness, WCAM 2023 The 9th Annual Congress World of Advanced Materials, May 2023, Japan
- Babici L. M., Tudor A., J. Romeu, Acoustic emission at the wheel-rail contact with micro-slip and stick-slip, International Congress and Exposition on Noise Control Engineering, Glasgow, United Kingdom (2022)

- Babici L. M., Acoustic emission in stick-slip phenomena of wheel-rail contact for variable velocity, IWRN13 Conference (13th International Workshop on Railway Noise), Leuven, Belgium (2019)
- Babici L. M., Tudor A., J. Romeu, M. Stoica, Fractal evaluation aspects in characterizing the roughness of a driving wheel from a locomotive, International Conference on Tribology ROTRIB, Gluj-Napoca, Romania (2020)
- Babici L. M., Tudor A., PRASIC'18, Some aspects regarding the roughness of the railway surface and rolling noise at locomotives, 10^{th} Product Design, Robotics, Advanced Mechanical& Mechatronic Systems and Innovation Conference, 2018, Brasov, Romania, in IOP Conference Series: Materials Science and Engineering, vol. 517, 2019

Symposiums

- Babici L. M., I. Sebeșan, Tudor A., Parametrul fractal in caracterul microgeometriei șinei (The fractal parameter in the character of rail microgeometry), Railway Rolling Material Symposium, November 2018
- I. Sebeşan, Babici L. M., Zgomotul aerodinamic în transportul feroviar (The aerodynamic noise in railway transport), Railway Rolling Material Symposium, November 2017

References

[1] Akay A., Acoustics of friction. J. Acoust. Soc. Am. 2002, 111 (4), 1525 - 1548.

[2] Almqvist A., Sahlin F., Larsson R., Glavatskih S., On the dry elastoplastic contact of nominally flat surfaces, 2006, Tribology International 40, 2007, 574 - 579.

[3] Amontons G., De la résistance causée dans les machines, Mem. l'Acad. Roy. A, 1699; 257 - 82.

[4] Antoniou S. S., Cameron A., Gentle C. R., The friction-speed relation from stick-slip data. Wear, 1976, 36, 235 - 254.

[5] Archard J. F., Wear, Theory and Mechanisms. In Wear Control Handbook, Peterson, M. B. Winer, W.O., Eds., ASME: New York, NY, USA, 1980, pp. 35 - 80.

[6] Asamene K., Sundaresan M., Analysis of experimentally generated friction-related acoustic emission signals. Wear, 2012, 296, 607 - 618.

[7] Babici L. M., Tudor A., Some aspects regarding the roughness of the railway surface and rolling noise at locomotives, IOP Conf. Series: Materials Science and Engineering, 514 2019 012010.

[8] Babici L. M., Tudor A., Stoica N. A., Stoica M., Acoustic emission in stick-slip phenomena of wheel-rail contact for variable velocity. In Proceedings of the 13th International Workshop on Railway Noise, Ghent, Belgium, 16 - 20 September 2019.

[9] Badger J., Murphy S., O'Donnell G., Acoustic emission in dressing of grinding wheels: AE intensity, dressing energy, and quantification of dressing sharpness and increase in diamond wear-flat size. Int. J. Mach. Tools Manuf. 2018, 125, 11 - 19. https://doi.org/10.1016/j.ijmachtools.2017.11.007.

[10] Baumberger et al., Nonlinear analysis of stick-slip bifurcation in the cree-controlled regime of dry friction, Physical Review E, 51(5), 1995, pp. 4005-4010.

[11] Benabdallah H. S., Aguilar D. A., Acoustic Emission and its Relationship with Friction and wear for Sliding Contact. Tribol. Trans., 2008, 51, 738 - 747.

[12] Benardos P. G. and Vosniakos G. C., Predicting surface roughness in machining: a review, Int. J. Mach. Tool Manuf. 43 2003 833 - 844.

[13] Berry M. V. and Lewis Z. V., On the Weierstrass - Mandelbrot fractal function, Proc. R. Soc. Lond. A, 370, 1980, 459 - 484.

[14] Bhushan B., Majumdar A., Elastic-plastic contact model for bifractal surfaces, Wear, 153, 1992, 53 - 64.

[15] Bhushan B., Poon C. Y., Comparison of surface roughness measurements by stylus profiler, afm and non-contact optical profiler. Wear, 1995; 190:76 – 8.

[16] Bhushan B., Principle and Applications of Tribology John Wiley & Sons Inc: New York, NY, USA, 1999, pp. 344 - 430.

[17] Blau P. J., The significance and use of the friction coefficient. Tribol. Int., 2001, 34, 585 - 591.

[18] Bo L. C., Pavelescu D., The friction-speed relation and its influence on the critical velocity of stick-slip motion. Wear, 1982, 82, 277 - 289.

[19] Boaron A., Weingaertner W. L., Dynamic in-process characterisation method based on acoustic emission for topographic assessment of conventional grinding wheels. Wear, 2018, 29, 406 - 218.

[20] Boness R. J., Hawthorne H. M., Acoustic emission from the unlubricated sliding wear of steel and silicon nitride. Tribol. Trans., 1995, 38, 293 - 298.

[21] Boslaugh S., Watters P. A., Statistics in a Nutshell: A Desktop Quick Reference; O'Reilly Media: Sebastopol, CA, USA, 2008, Chapter 7, ISBN-13 978-0596510497.

[22] Bush W., Gibson R. D., Keogh G. P.. Strongly anisotropic rough surfaces. ASME J Lubr Technol, 1979, 101:15

[23] Bush W., Gibson R. D., Thomas T. R., The elastic contact of rough surface. Wear, 1975, 35, 87 - 111.

[24] Caroli C., Nozieres P., Persson B. N. J., Tossatti E., Dry friction as a hysteretic elastic response. In Physics of Sliding Friction, Springer: Dordrecht, The Netherlands, 1995, pp. 27 - 49.

[25] Carr J. R., Benzer W. B., On the practice of estimating fractal dimension, Math. Geol., 23, 1991, 945 - 958.

[26] Chang W. R., Etsion I., Bogy B. D., An elastic-plastic model for the contact of rough surfaces. ASME J. Tribol., 1987, 109, 257 - 263.

[27] Chang W. R., Etsion I., Bogy D. B., Static friction coefficient model for metallic rough surfaces. ASME J. Tribol., 1988, 110, 57 - 63.

[28] Chowdhury M. A., Khalil M. K., Nuruzzaman D. M., Rahaman M. L., The Effect of Sliding Speed and Normal Load on Friction and Wear. Int. J. Mech. Mechatron. Eng., 2011, 11, 53 - 57.

[29] Chuanjun L., Shuangfu S., Yuming W., Weifeng H., Ying L., Study on Stick-Slip Friction of Reciprocating O-Ring Seals Using Acoustic Emission Techniques. Tribol. Trans., 2012, 55, 43 - 51.

[30] Ciavarella M., Transition from stick to slip in Hertzian contact with "Griffith" friction: The Cattaneo–Mindlin problem revisited. J. Mech. Phys. Solids, 2015, 84, 313 - 324.

[31] Cooper A. J. et al., The effect of anisotropic and isotropic roughness on the convective stability of the rotating disk boundary layer, Phys. Fluids 27, 2015, 014107.

[32] Coulomb C. A., Théorie des machines simples, en ayant égard au frottement de leurs parties, et la roideur des cordages. Mem Math Phys Paris 1785; x:161 - 342

[33] Crandall S. H. and Zhu W. Q., Random vibration: A survey of recent developments, J. Appl. Mech. Trans., 50 (4B), 1983, 953 - 962.

[34] Da Vinci L., Notebooks and manuscripts prepared in the late 1400s, as described in [3].

[35] Danian C., On adhesive friction coefficient with fractal geometry Part J. Acta Mechanica Sinica, 2003, 35 (3): 296 - 301.

[36] Demkin N. B., Izmailov V. V., Surface Topography and Properties of Frictional Contacts. Tribology International, 1991, 24(1): 21 - 24.

[37] Diehl R. J., Holm P., Roughness measurement-have the necessities changed?, Journal of Sound and Vibrations, 293, (2006), 777 - 783.

[38] Diei E. N., Dornfeld D., A model of tool fracture generated acoustic emission during machining. Trans. ASME J. Eng. Ind., 1987, 109, 227 - 233.

[39] Dieterich J. H., and Kilgore, B. D. Direct observation of frictional contacts: new insights for state-dependent properties, Pageoph., (1994), 143, 283-302.

[40] Diniz A. E., Dornfeld D. A., Correlating tool life, tool wear and surface roughness by monitoring acoustic emission in finish turning, Wear, 1992, 152, 395 - 407.

[41] Dobrynin S. A., Kolubaev E. A., Smolin A. Y., Dmitriev A. I., Psakhie S. G., Time-frequency analysis of acoustic signals in the audio-frequency range generated during Hadfield's steel friction. Tech. Phys. Lett., 2010, 36, 606 - 609.

[42] Dong W. P., Sullivan P. J. and Stout K. J., Comprehensive study of parameters for characterizing three-dimensional surface topography, Wear, 178, 1994, 29 - 43.

[43] Douglas R. M., Steel J. A., Reuben R. L., A study of the tribological behaviour of piston ring/cylinder liner interaction in diesel engines using acoustic emission. Tribol. Int. 2006, 39, 1634 - 1642.

[44] Dowson D., History of tribology. 2nd ed. London: Professional Engineering Publishers, 1998.

[45] Eid H., Adams G. G., McGruer N. E., Fortini A., Buldyrev S., Srolovitz D., A Combined Molecular Dynamics and Finite Element Analysis of Contact and Adhesion of a Rough Sphere and a Flat Surface. Tribol. Trans., 2011, 54, 920 - 928. https://doi.org/10.1080/10402004.2011.615638.

[46] Elasha F., Greaves M., Mba D., Fang D., A comparative study of the effectiveness of vibration and acoustic emission in diagnosing a defective bearing in a planetary gearbox. Appl. Acoust. 2017, 95, 115 - 181.

[47] Elseved cap 2 Wheel rail interface

[48] Emel E., Kannatey - Asibu E. Jr., Tool Failure Monitoring in Turning by Pattern Recognition Analysis of AE Signals. ASME J. Eng. Ind. 1988, 110, 137 - 145.

[49] Ferrer C., Salas F. Ã., Pascual M., Orozco J., Discrete acoustic emission waves during stick-slip friction between steel samples. Tribol. Int. 2010, 43, 1 - 6.

[50] Filippov A. V., Rubtsov V. E., Tarasov S. Y. Y., Acoustic emission study of surface deterioration in trip contacting. Appl. Acoust., 2017, 12, 117 - 106.

[51] Gadelmawla E. S. et al., Roughness parameters, J. Mater. Process. Technol, 123, 2002, 133 - 145.

[52] Gagnepain J. J., and Roques-Carmes C., Fractal Approach to Two - Dimensional and Three - Dimensional Surface Roughness, Wear, 109 1986 119 - 126.

[53] Ganti S., Bhushan B., Generalized fractal analysis and its surfaces applications to engineering surfaces, Wear, 180, 1995, 17 - 34.

[54] González E. M., Detection of Failure Mechanisms of Tool Steels by Means of Acoustic Emission Technique. Ph.D. Thesis, Escola Universitària d'Enginyeria Tècnica Industrial de Barcelona, Mechanical Engineering Department, Universitat Politècnica de Catalunya (UPC), 2013.

[55] Gourdon D., Israelachvili J. N., Transitions between smooth and complex stick-slip sliding of surfaces. Am. Phys. Soc., 2003, 68, 1 - 10.

[56] Green I., Exact Spectral Moments and Differentiability of the Weierstrass-Mandelbrot Fractal Function, J. Tribol., 142(4), 2020, 041501.

[57] Green R. E. Jr., Basic Wave Analysis of Acoustic Emission. In Mechanics of Non-destructive Testing, Springer: Boston, MA, USA, 1980, pp. 55 - 76.

[58] Greenwood J. A. and Williamson J. B. P., Contact of nominally flat surfaces, Proc. R. Sot. London, Ser. A, 295, 1966, 308 - 319.

[59] Greenwood J. A., Williamson J. B. P., Contact of nominally flat surfaces. Proc. R. Soc. Lond., 1966, 295, 300 - 319.

[60] Gujrati A. et al., Combining TEM, AFM, and profilometry for quantitative topography characterization across all scales, ACS Appl. Mater. Interf., 10, 2018, 29169.

[61] Hamdi A., Merghache S. M. and Aliouane T., Effect of cutting variables on bearing area curve parameters (BAC-P) during hard turning process, Arch. Mech, 67(1), 2020, 73 - 95.

[62] Hanaor D., Gan Y. and Einav I., Static friction at fractal interfaces. Tribology International, 2016, 93, 229 - 238.

[63] Hanchi J., Klamecki B. E., Acoustic emission monitoring of the wear process. Wear, 1991, 145, 1 - 27.

[64] Hase A., Mishina H., Wada M., Microscopic study on the relationship between AE signal and wear amount. Wear 2013, 308, 142 - 147.

[65] He L. and Zhu J., The fractal character of processed metal surfaces, Wear, 208, 1997, 17 - 24.

[66] He P. et al., Analysis of the best roughness surface based on the bearing area curve theory, Proc IMechE Part J: J Engineering Tribology ,2021, 1 - 14.

[67] Heslot F., Baumberger T., Perrin B., Creep, stick-slip, and dry-friction dynamics: Experiments and a heuristic model. Am. Phys. Soc., 1994, 49, 4973 - 4950.

[68] Jacobs T. D. B., Junge T. and Pastewka L., Quantitative characterization of surface topography using spectral analysis, Surf. Topogr. Metrol. Prop., 5, 2017, 013001.

[69] Johnson K. L., Contact mechanics [M]. Cambridge: Cambridge University Press, 1987.

[70] Jordan D. L., Hollins R. C. and Jakeman E., Measurement and characterization of multi-scale surface, Wear, 109, 1986, 127 - 134.

[71] Jun Z. J., Shi H. Y., Wei C., Fractal Prediction Model of Friction Coefficient in Dry Friction Pair, Advanced Materials Research, Vols 301 - 303, 2011, pp 315 - 320 Trans Tech Publications, Switzerland

[72] Kamash K. M. A. and Robson J. D., Application of isotropy in road surface modelling. J. Sound Vib, 57(1) 89 - 100, 1978.

[73] Kato S., Sato N., Matsubyashi T., Some Considerations on Characteristics of Static Friction of Machine Tool Slideway. J. Lubr. Technol., 1972, 72, 234 - 247.

[74] Kishawy H. A., Hegab H., Umer U., Mohany A., Application of acoustic emissions in machining processes: Analysis and critical review. Int. J. Adv. Manuf. Technol., 2018, 98, 1391 - 1407.

[75] Kiyak M., Çakir O., Examination of machining parameters on surface roughness in EDM of tool steel, J. Mater. Process. Technol., 191, 2007, 141 - 144.

[76] Kogut L., Etsion I., A semi-analytical solution for the sliding inception of a spherical contact. ASME J. Tribol., 2003, 125, 499 - 506.

[77] Kogut L., Etsion I., A static friction model for elastic-plastic contacting rough surfaces. ASME J. Tribol., 2004, 126, 34 - 40.

[78] Kogut L., Etsion I., Elastic–plastic contact analysis of a sphere and a rigid flat. ASME J. Appl. Mech., 2002, 69, 657 - 662.

[79] Kourroussis G., Connolly D. P. and Verlinden O., Railway induced ground vibrations - A review of vehicle effects, Int. J. Rail Transp., 2(2), 2014, 69 - 110.

[80] Lan G., Sun W., Zhang X., et al. A three-dimensional fractal model of the normal contact characteristics of two contacting rough surfaces. AIP Advances, 2021, 11(5): 055023.

[81] Lan G., Zhang X., Ding H., et al. Modified model of static friction coefficient of joint interfaces based on fractal theory. Transactions of the Chinese Society for Agricultural Machinery, 2012, 43(1): 213 - 218.

[82] Li H. et al., Estimation Method of Ideal Fractal Parameters for Multi-Scale Measurement of Polished Surface Topography, Fractal Fract, 7 (17), 2023, 1 - 15.

[83] Li L., Wang J., Shi X., et al. Contact stiffness model of joint surface considering continuous smooth characteristics and asperity interaction. Tribology Letters, 2021, 69(2): 1 - 12.

[84] Li X., Wang Z., Wang X., et al. Research on static friction coefficient of joint surfaces considering elastic-plastic deformation based on fractal model [J]. International Journal of Industrial and Systems Engineering, 2019, 32(1), 32 - 55.

[85] Lontin K., Khan M., Interdependence of friction, wear, and noise. Friction, 2021, 9, 1319 - 1345. https://doi.org/10.1007/s40544-021-0500-x.

[86] Majumdar A. and Bhushan B., Role of fractal geometry in roughness characterization and contact mechanics of surfaces, J. Tribol., 112, 1990, 205 - 216.

[87] Majumdar A., Bhushan B., Fractal model of elastic–plastic contact between rough surfaces. ASME J. Tribol., 1991, 113, 1 - 11.

[88] Majumdar A., Bhushan B., Fractal model of elastoplastic contact between rough surfaces, J. Tribol. 113, 1991, 1 - 11.

[89] Majumdar A., Bhushan B., Role of fractal geometry in roughness characterisation and contact mechanics of surfaces J, Journal of Tribology, 1990, 112(2): 205 - 216.

[90] Majumdar A., Tien C. L., Fractal characterization and simulation of rough surfaces, Wear, 136, 1990, 313–327.

[91] Majumdar A., Tien C. L., Fractal Network Model for Contact Conductance, J. Heat Transfer., 113 (3), 1991, 516 - 525.

[92] Malinverno A., A simple method to estimate the fractal dimension of a self-affine series, Geophys. Res. Lett.,17, 1990, 1953 - 1956.

[93] Mandelbrot B. B. and Van Ness J. W., Fractional Brownian motions fractional noises and applications, Siam review, 10, 1968, 422-437, H11, 254 - 284.

[94] Mandelbrot B. B., How long is the coast of Britain, Science 156, 1967, 636 - 638.

[95] Mandelbrot B. B., Self-affine fractals and fractal dimension, Phys. Scr. 32, 1985, 257 - 260.

[96] Mandelbrot B. B., The Fractal Geometry of Nature, eds. Echo Point Books & Media, (Brattleboro, Vermont, 2021.

[97] Martinez E., Picas I., Romeu J., Casellas D., Filtering of Acoustic Emission Signals for the Accurate Identification of Fracture Mechanisms in Bending Tests. Mater. Trans. 2013, 54, 1087 - 1094.

[98] Matcharashvili T., Chelidze T., Zhukova N., Mepharidze E., Investigation of acoustic emission accompanying stick-slip movement of rock samples at different spring stiffnesses–block system. Tribol. Int., 2011, 44, 811 - 819.

[99] Mendelson A., Plasticity: Theory and Application, Macmillan, New York, 1968.

[100] Meriaux J., Boinet M., Fouvry S., Lenain J. C., Identification of fretting fatigue crack propagation mechanisms using acoustic emission. Tribol. Int., 2010, 43, 2166 - 2174.

[101] Miao X. M., Huang X. D., A complete contact model of a fractal rough surface [J]. Wear, 2014, 309(1), 146 - 151.

[102] Morag Y., Etsion I., Resolving the contradiction of asperities plastic to elastic mode transition in current contact models of fractal rough surfaces [J]., Wear, 2007, 262(5), 624 - 629.

[103] Mulakaluri N., Persson B. N. J., Adhesion between elastic solids with randomly rough surfaces: Comparison of analytical theory with molecular-dynamics simulations. EPL 2011, 96, 66003. https://doi.org/10.1209/0295-5075/96/66003.

[104] Nayak P. R., Random process model of rough surfaces, J. Lube. Technol., 93 1971, 398 - 407.

[105] Nayak P. R., Random process model of rough surfaces. ASME J Lubr Technol, 1971, 93, 398 - 407.

[106] Nayak P. R., Some aspects of surface roughness, Wear, 26, 1973, 165 - 174.

[107] Nettleton D., Commercial Data Mining-Processing, Analysis and Modelling for Predictive Analytics Projects, Morgan Kaufmann: Boston, MA, USA, 2014.

[108] Onion R. A., Archard J. F., The contact of surfaces having a random structure. J Phys D, 1973.

[109] Otero Yugat J., Contribución al estudio de las vibraciones producidas por el contacto rueda-carril y su transmisión al entorno, M. S. thesis, Universitat Politècnica De Catalunya, 2009.

[110] Ozaki S., Matsuura T., Maegawa S., Rate, state and pressure-dependent friction model based on the elastoplastic theory. Friction, 2020, 8, 768 - 783.

[111] Pan W., Li X., Wang X., Contact mechanics of elastic-plastic fractal surfaces and static friction analysis of asperity scale. Engineering Computations, 2020, 38(1): 131 - 150

[112] Pavelescu D., Tudor A., On the roughness fractal character, the tribological parameters and the error factors, 5 (2), 2004, 1 - 6.

[113] Pavelescu D., Tudor A., The sliding friction coefficient-its evolution and usefulness. Wear, 1987, 120, 321 - 336.

[114] Peitgen H. O. and Saupe D., The Science of Fractal Images, eds. Springer-Verlag, (New York, 1988, pp. 82 - 91.

[115] Peng Y. F., Guo Y. B., An elastic-plastic adhesion model for contacting fractal rough surface and perfectly wetted plane with meniscus[J]. Chinese Journal of Mechanical Engineering, 2009, 22(1), 9 - 14.

[116] Persson B. N. J., Sliding Friction. In Physical Principles and Applications, Springer-Verlag: New York, NY, USA, 2000.

[117] Persson B. N. J., Tossati E., Physics of sliding friction, 1995, Series E, Applied Science, 311.

[118] Popov V. L., Contact Mechanics and Friction, Physical Principles and Applications, Springer, 2009.

[119] Reddy T. S., Reddy C. E., Realtime monitoring of surface roughness by acoustic emissions in CNC turning. J. Eng. Sci. Technol., 2010, 3, 111 - 115.

[120] Rice J. R., & Ruina, A. L. Stability of Steady Frictional Slipping. Journal of Applied Mechanics, 50(2), 343,(1983). doi:10.1115/1.3167042

[121] Ruina A. Slip instability and state variable friction laws. Journal of Geophysical Research: Solid Earth, 88(B12), (1983), 10359–10370. doi:10.1029/jb088ib12p10359

[122] Russ J. C., Fractal Surfaces, Plenum Press, New York, 1994.

[123] Sadegh H., Mehdi A. N. N., Mehdi A., Classification of acoustic emission signals generated from journal bearing at different lubrication conditions based on wavelet analysis in combination with artificial neural network and genetic algorithm. Tribol. Int., 2016, 95, 426 - 434.

[124] Sanner A. et al., Scale-dependent roughness parameters for topography analysis, Appl. Surf. Sci. Adv., 7, 2022, 100190 1 - 10.

[125] Sayles R. S., Thomas T. R., The spatial representation of surface roughness by means of the structure function: A practical alternative to correlation. Wear, 42, 1977, 263 - 276.

[126] Sheng X., Luo J., Wen S., Static Friction Coefficient Model Based on Fractal Contact [J]. China Mechanical Engineering, 1998, (7), 16 - 18.

[127] Shiotani T., Parameter Analysis, Acoustic Emission Testing, Springer Nature: Berlin / Heidelberg, Germany, 2008, pp. 41 - 51.

[128] Singh A. N., The theory and construction of non-differentiable functions, in Squaring the Circle and Other Monographs, Chelsea Publishing, 1953.

[129] Sovey S., Osman K. and Mohd-Matore M. E., Exploratory and confirmatory factor analysis for disposition levels of computational thinking instrument among secondary school students, European Journal of Educational Research, 11(2), 2022, 639 - 652.

[130] Stachowiak G. W., Batchelor A. W. and Stachowiak G. B. in Experimental Methods in Tribology, (Tribology Series 44) ed. D. Dowson, Academic Press – Elsevier, 2004, Chap. 6, pp. 115 - 125, Chap. 10, pp. 475 - 488.

[131] Stoica N. A., Petrescu A. M., Tudor A., Pedrescu A., Tribological properties of the disc brake friction couple materials in the range of small and very small speeds. InIOP Conference Series: Materials Science and Engineering, Proceedings of the13th International Conference on Tribology (ROTRIB'16), Galati, Romania, 22 - 24 September 2016, IOP Publishing: Galati, Romania, 2017, Volume 174. https://doi.org/10.1088/1757-899X/174/1/012019.

[132] Storåkers B., Elaguine D., Hertz contact at finite friction and arbitrary profiles. J. Mech. Phys. Solids, 2005, 53, 1422 - 1447.

[133] Strombergsson D., Marklund P., Edin E., Zeman F., Acoustic emission monitoring of mechanic-chemical surface finishing process. Tribol. Int., 2017, 36, 112 - 129.

[134] Sun J., Wood R. J. K., Wang L., Care I., Powrie H. E. G., Wear monitoring of bearing steel using electrostatic and acoustic emission techniques. Wear, 2005, 259, 1482 - 1489.

[135] T. Baumberger, Dry friction dynamics at low velocities, In Physical Principles and Applications, Springer-Verlag: New York, NY, USA, 1996, pp 1-26.

[136] Thomas T. R., in Rough surface, eds. Thomas T. R. M. Sc., Ph.D., C.Eng., F. Inst. P., M. I. Mech. E., M. I. Prod. E., (Longman Inc., New York, 1982, pp. 2 - 9, 72 - 90, 91 - 111.

[137] Thomas T. R., Thomas A. P., Fractals and engineering surface roughness, Surf. Topogr., 1, 1988, 1 - 10.

[138] Thompson B. D., Young R. P., Lockner D. A., Observations of premonitory acoustic emission and slip nucleation during a stick-slip experiment in smooth faulted Westerly granite. Geophys. Res. Lett. 2005, 32, 1 - 4. https://doi.org/10.1029/2005GL022750.

[139] Thompson D. J., Hemsworth B. and Vincent N., Experimental validation of the TWINS prediction program for rolling noise, part I: description of the model and method, J. Sound Vib., 193, 1996, 123 - 135.

[140] Thompson D. J., in Noise and Vibration from High-Speed Trains, eds. V. V. Krylov and T. T. Limited (Loughborough University, 2001) Theory of generation of wheel / rail rolling noise, Thomas Telford, London, 2001, pp. 3 - 23.

[141] Thompson D. J., Railway Noise and Vibration: Mechanisms, Modelling and Means of Control. Elsevier Ltd, 2009,

[142] Thompson D. J., The influence of the contact zone on the excitation of wheel/rail noise, Journal of Sound and Vibrations, 267 (2003) 523 - 536.

[143] Tian H., Liu F., Zhao C., et al. Prediction of surface static tribological properties of metallic materials - experimental support. Journal of Vibration and Shock, 2014, 33(1): 209 - 220.

[144] Tian H., Zhao C., Fang Z., et al. Mathematical model of nonlinear friction based on anisotropic fractal geometric theory. Journal of Vibration and Shock, 2013 - 2, 32 (23): 135 - 144.

[145] Tian H., Zhao C., Fang Z., et al. Predication investigation on static tribological performance of metallic material surfaces—theoretical model. Journal of Vibration and Shock, 2013 - 1, 32 (12): 40 - 44, 66.

[146] Tian H., Zhu D., Qin H., Fractal model of static friction coefficient of joint interface and its simulation. Chinese Journal of Applied Mechanics, 2011, 28(2): 158 - 162.

[147] Tian P., Tian Y., Shan L., Meng Y., Zhang X., A correlation analysis method for analysing tribological states using acoustic emission, frictional coefficient, and contact resistance signals. Friction, 2015, 3, 36 - 46.

[148] Timoshenko S., Goodier J. N., Theory of elasticity. New York: McGraw-Hill Book Comp., Inc., 1951.

[149] Verheijen E., A survey on roughness measurements, Journal of Sound and Vibrations, 293 (2006), 784 - 794.

[150] Villamarin R. A., A model for railway induced ground vibrations in the frame of preliminary assessment studies, M. S. thesis, Universitat Politècnica De Catalunya, 2011.

[151] Wang S., Komvopoulos K., A fractal theory of the temperature distribution at elastic contacts of fast sliding surfaces. ASME J. Tribol., 1995, 117, 203 - 214.

[152] Wen R. J., Sinding-Larsen R., Uncertainty in fractal dimension estimated from power spectra and variograms, Math. Geol., 29, 1997, 727 - 753.

[153] Whitehouse D. J., Archard J. F., The properties of random surface of significance in their contact. Proc Roy Soc (London) Ser A, 1970, 316, 97 - 121.

[154] Whitehouse D. J., Phillips M. J.. Discrete properties of random surfaces. Philos Trans R Soc (London) Ser A, 1978, 290: 267 - 98.

[155] Whitehouse D. J., Phillips M. J.. Two-dimensional discrete properties of random surfaces. Philos Trans R Soc (London) Ser A, 1982, 305: 441 - 68.

[156] Xiao L. et al., A study on the effect of surface topography on rough friction in roller contact, Wear, 254, 2003, 1162 - 1169.

[157] Yang J., Komvopoulos K., A mechanics approach to static friction of elastic–plastic fractal surfaces. ASME J. Tribol., 2005, 127, 315.

[158] Youand J. M., Chen T. N., A static friction model for the contact of fractal surfaces, Proc. IMechE Vol. 224 Part J: J. Engineering Tribology, 2010, pg. 513 - 518, DOI: 10.1243/13506501JET760

[159] Yuan Y., Gan L., Liu K., & Yang X., 2016. Elastoplastic contact mechanics model of rough surface based on fractal theory. Chinese Journal of Mechanical Engineering, 30(1), 207 - 215.

[160] Yusof N. F. M., & Ripin Z. M., A technique to measure surface asperities plastic deformation and wear in rolling contact. Wear, 2016, 1 - 9.

[161] Začal J., Dostál P., Šustr M., Dobrocký D., Acoustic emission during tensile testing of composite materials. Acta Univ. Agric. et Silvic. Mendel. Brun., 2017, 65, 1309 - 1315. doi.org/10.11118/actaun201765041309.

[162] Zeng Q. et al., Correlating and evaluating the functionality-related properties with surface texture parameters and specific characteristics of machined components, Int. J. Mech. Sci., 149, 2018, 62 - 72.

[163] Zhan W., Fink R., Fang A., Application of Statistics in Engineering Technology Programs. Am. J. Eng. Educ., 2010, 1, 65 - 78.

[164] Zhang C. et al., Static friction coefficient model of joint surface based on the modified fractal model and experimental investigation, The International Journal of Advanced Manufacturing Technology, 2022, 124 (11-12), 1 - 15

[165] Zhang W. et. al., Wheel / rail adhesion and analysis by using scale roller rig, Wear, 253, (2002), 82 - 88.

[166] Zhang X., Xu Y. and Jackson R. L., An analysis of generated fractal and measured rough surfaces in regards to their multi-scale structure and fractal dimension, Tribol. Int., 105, 2017, 94 - 101.

[167] Zhang Y., Zhang X., Jiang L., et al. Fractal Model of Static Frictional Coefficient on Joint Surface Considering Elastic-plastic Deformation. Journal of Taiyuan University of Science and Technology of China, 2014, 25(4): 294 - 301.

[168] Zhao B., Xu H. & Lu X., 2019. Sliding Interaction for Coated Asperity with Power-Law Hardening Elastic-Plastic Coatings. Materials, 12(15), 2388.

[169] Zhao Y. W., Maietta D. M., L. Chang, An asperity micro-contact model incorporating the transition from elastic deformation to fully plastic flow. ASME J. Tribol., 2000, 122, 86 - 93.

[170] Zhou G. Y. et al., Fractal geometry model for wear prediction, Wear, 170, 1993, 1 - 14

[171] Zhou G. Y., Leu M. C., Blackmore D., Fractal geometry model for wear prediction. Wear, 1993, 170, 1 - 14.

[172] Zhou G., Statistical, random and fractal characterizations of surface topography with engineering application, A Dissertation Submitted to the Faculty of New Jersey Institute of Technology in Partial Fulfilment of the Requirements for the Degree of Doctor of Philosophy Department of Mechanical and Industrial Engineering, 1993.

[173] Zhu H. et al., Experimental study on the characterization of worn surface topography with characteristic roughness parameter, Wear, 255, 2003, 309 - 314.

[174] Zuo L., Zuo D., Zhu Y., Wang H., Acoustic emission analysis for tool wear state during friction stir joining of SiCp/Al composite. Int. J. Adv. Manuf. Technol., 2018, 99, 1361 - 1368.

* EN ISO 21920 - 2: 2023 Geometrical product specifications (GPS) - Surface texture: Profile - Part 2: Terms, definitions and surface texture parameters.

** EN 15610: 2018 Railway applications. Acoustics. Rail and wheel roughness measurement related to noise generation.

*** ISO 3095: 2013 Acoustics - Railway applications - Measurement of noise emitted by rail bound vehicles.

Abstract

In this study, the Weierstrass fractal function was used to model the surface roughness of railway tracks and, subsequently, the static coefficient of friction (COF) for Hertzian rail-wheel contact and cylinder-plane interactions. This methodology is based on the assumption that the fractal nature of surface roughness can be effectively captured using fractal parameters, which significantly influence the contact mechanics and frictional behaviour observed in railway systems.

Initially, the study focused on a detailed modelling of the railway track surface roughness. To validate the efficacy of this model, a rigorous and meticulous comparison between the theoretical results obtained and the experimental data was conducted. These data were collected through extensive roughness measurements carried out at the Faurei Railway Testing Centre in Romania. For robust validation, 41 roughness parameters derived from the fractal model were compared with those measured experimentally. This comprehensive approach allowed not only for the validation of the fractal model but also for its refinement by identifying which parameters are most critical in representing the real roughness of the tracks, as well as the minimum measuring length for determining acoustic roughness.

The experimental determination of the static COF was conducted through laboratory tests involving two cylinder-plane specimens, made from the same material as the railway wheel and track. This configuration was chosen to closely replicate the contact conditions found in actual wheel-rail interactions, thus ensuring that the experimental data collected were representative and reliable.

To precisely determine the static COF, the stick-slip (SS) process was meticulously characterized by monitoring acoustic emissions (AE), allowing for convenient identification of each phase. The acoustic emissions provided a non-invasive means not only to detect transitions between stick and slip phases but also to understand the underlying mechanisms driving these transitions.

This dual approach of theoretical modelling and experimental validation forms the core of this methodology and offers a comprehensive understanding of the frictional phenomena occurring within railway systems, which essential for designing and maintaining safer and more efficient railway operations. The insights gained from this study are expected to significantly contribute to the development of new standards and practices in railway engineering, particularly in areas of wear reduction, noise control, and overall system reliability.

The results of this research pave the way for a more nuanced understanding of the fractal nature of contact surfaces and their implications on tribological performance.